LOCAL STRUCTURE AND THE PHOTOELASTIC RESPONSE IN ZINC-MODIFIED OXIDE GLASS

by

Jeremy Thorbahn

Submitted in partial fulfilment of the requirements
for the degree of Master of Science

at

Dalhousie University
Halifax, Nova Scotia
August 2013

Table of Contents

List of Tables

List of Figures

Abstract

Understanding the relationship between the structure of materials and their properties allows for the development of new applications and technologies. Here the relationship between local structure and optical properties in several binary oxide glass systems containing zinc oxide was examined, in particular the relationship between structure, applied stress and induced birefringence in a glass. The empirical model introduced by Zwanziger and co-workers posits a negative correlation between the ratio of the bond length to coordination number in a glass and the induced birefringence; zinc oxide in this model is predicted to be exactly at the threshold between positive and negative birefringence and is thus of particular interest to investigate. XAFS and Raman spectroscopy were used to determine local structure while the Sénarmont compensator method, Abbe refractometry and spectroscopic ellipsometry were used to measure optical properties.

List of Abbreviations and Symbols Used

T_g Glass transition temperature

NBO   Non-bridging oxygen

n   Index of refraction

Δn   Birefringence

C Stress-optic coefficient

σ Applied mechanical stress

δ Optical path length difference

l Sample thickness

π_{ij} Photoelastic tensor

B_i Relative dielectric impermeability

x_i Molar fraction

y_i Principal axes of the indicatrix

ξ Polarizability ratio

α Polarizability

d Bond length

N_c Coordination number

Å   Angstroms

XAFS   X-ray Absorption Fine Structure

NMR   Nuclear Magnetic Resonance

$\mu(E)$ XAFS absorption coefficient

H Hamiltonian

$\langle i|$ Initial state

$|f\rangle$ Final state

$C.C.$ Complex conjugate

χ Fractional change in EXAFS absorption coefficient

EXAFS   Extended X-ray Absorption Fine Structure

A   Quantized radiation field

p   Momentum

m	Mass
c	Speed of light
k	Wavenumber
ϵ	Polarization vector
e	Electronic charge
ω	Angular frequency
r	Radial coordinate of photoelectron wave function
$\delta(r)$	Dirac delta function
$f(k)$	EXAFS amplitude factor
R	Scattering path length
σ_j^2	Variance in absorber-scatterer distance
$\lambda(k)$	Mean free path
$\delta_j(k)$	Scattering phase shift
I_1, I_2 and I_3	Intensity from beamline detectors
S_0^2	Passive electron reduction factor
ΔE_0	EXAFS edge shift
ΔR	Scattering path length difference
ρ	Density
W	Weight
λ	Wavelength
eV	Electron-volts
NIR	Near-infrared
N_3	Fraction of 3-fold coordinated structural units

Acknowledgements

I would first like to acknowledge the support of my supervisor, Dr. Josef Zwanziger, for allowing me to work on a project that has been consistently interesting and challenging. Under Joe's guidance I have learned a great deal and also have had the opportunity to work independently and explore my own ideas. I would like to thank my colleagues in the lab, Justine Galbraith, Courtney Calahoo and Dr. Amir Mohajerani, who taught me many of the sample preparation and measurement techniques that I used in this work. Dr. Ning Chen at the Canadian Light Source provided an incredible amount of assistance in carrying out our XAFS experiments. On a more personal note, I would like to thank my parents for their continued support in all that I do, and my partner, Ashley-Rose, who has always been very understanding throughout my graduate program. I would lastly like to thank Dr. Ted Monchesky and Dr. Peng Zhang for acting on my supervisory and defence committees.

Chapter 1

Introduction

Studying the properties of materials enables the development of new technology [1, 2]. This work focuses on the properties of glass, which is a unique material with many technological applications. In particular, the relationship between the atomic arrangement and optical properties of glass is examined and potential applications for new types of glass are discussed.

While glass has been used for many centuries [3], modern technological developments have given glass some very important new uses. Fiber optic communication systems have revolutionized the way information is transmitted, and solar cells will have an increasingly important role in meeting our energy needs. These highly specialized applications require very specific types of glass with unique combinations of mechanical, chemical and optical properties. To meet these technological requirements, glass scientists must continuously investigate composition-structure-property relationships in glass to better understand how to obtain the desired characteristics.

In many applications, glass can be placed under stress, either unintentionally or by design. Stress can be mechanical, thermal or chemical and can exist within glass or be externally applied. Stress can alter glass even at the atomic level, changing its properties, and the effects of stress may detrimentally affect the performance of a glass. Macroscopically, glass could crack or even shatter under stress. However, even when glass appears unchanged to the naked eye, stress could still be affecting the transmission of light or other properties. The refractive index, which describes the speed of light in a material relative to free space, depends on how atoms are arranged and interactions between them. If the stress on glass is pushing its atoms and their electrons together or pulling them apart, the refractive index may change. If the refractive index is not the

same in every direction, for instance due to applied stress, then the glass is said to be birefringent. Birefringence can lead to unwanted effects such as image distortion.

The ability of glass to become birefringent under applied stress is known as *photoelasticity* and can be an undesirable property in many applications. In general, photoelasticity could cause problems in any application where a glass may experience mechanical stress and where preservation of image quality through the glass is important. A few such applications include high-precision optical instruments such as microscopes or telescopes [4], optical fibers and display technologies such as Liquid Crystal on Silicon (LCoS) [5]. In these cases, stress could arise due to the method of holding glass in place, bending of a fiber or due to thermal expansion if the glass is near a source of heat. Different types of glass exhibit varying degrees of photoelasticity, so it can be an important property to consider when choosing the best glass for a given application.
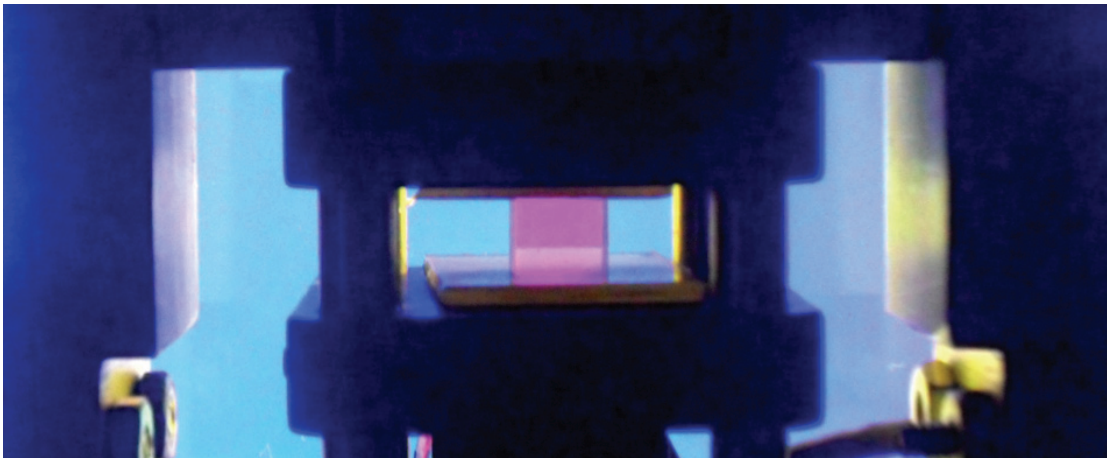
Fig 1.1: Stress-induced birefringence in oxide glass viewed through crossed polarizers

In some types of glass, photoelasticity can be very small or absent altogether. A glass with no photoelastic response is referred to as a zero stress-optic glass since the constant of proportionality between applied stress and induced birefringence, called the stress-optic coefficient, is zero. Zero stress-optic glass is commercially interesting since it is a crucial component in the aforementioned applications where photoelasticity is detrimental. The ideal zero stress-optic glass would be transparent, colourless, non-

dispersive, environmentally friendly and inexpensive to produce. Thus far, however, no ideal glass has been discovered, so research in this area continues.

A common means of obtaining a zero-stress optic response is through the addition of heavy metal oxides such as PbO to a glass composition. One commercially available zero-stress optic glass manufactured by Schott, called SF57, is a lead silicate glass. The optical properties of such glasses are appealing, but the use of heavy metals can be damaging to the environment and dangerous to humans. In 2006, the European Union restricted the use of lead, mercury and cadmium in many commercial products [6] and similar legislation is being considered elsewhere [7]. Therefore, it is important to find alternative types of zero stress-optic glass that are lead-free. Many researchers have worked on this problem and several lead-free zero stress-optic glasses have been proposed [5, 8, 9].

The stress-optic coefficient can be positive, negative, or zero, depending on whether the index of refraction in the stressed direction increases, decreases or remains unchanged. All of the compounds that form glass on their own have positive stress-optic coefficients, but adding other compounds to a glass composition can reduce the coefficient. The effort to design new zero stress-optic glasses involves identifying combinations of compounds that significantly reduce the stress-optic coefficient, while also giving rise to the other desirable properties such as transparency and durability. Barium tellurite, tin phosphate and zinc tin phosphate glass have all been shown to be capable of a zero stress-optic response [5, 8, 9]. Attempts to understand the origin of stress-induced birefringence and to model its relationship with glass structure are ongoing and have been useful in predicting zero stress-optic glass compositions.

In order to predict exactly how a certain glass composition would respond under stress, a complete theoretical understanding of the physical mechanism behind photoelasticity would be necessary. No such theory exists yet, nevertheless attempts have been made to explain the phenomena that cause photoelasticity and empirical relationships have been developed to make predictions about the photoelastic properties of a given glass composition. Mueller and Weyl each have published theoretical accounts of how atoms respond to stress in a manner that gives rise to birefringence [10, 11]. Their descriptions are largely based on deformations of the atomic lattice and polarization of

the electron cloud. Zwanziger *et al.* have developed a purely empirical model (henceforth referred to as "the empirical model of photoelasticity" or simply "the empirical model") that uses information about the structure of glass to predict whether it will have a positive or negative stress-optic response [5].

The empirical model is successful in predicting the stress-optic response for many types of glass. For others, however, it is not yet clear how the model should be applied. The model depends only on bond lengths and coordination numbers in glass, and for some glass additives these factors lead to a prediction on the threshold between positive and negative birefringence. Zinc oxide is one such example where the model has not yet been thoroughly tested. The goal of this thesis is to explore the relationship between structure and photoelasticity in glasses containing zinc oxide. The empirical model suggests that the addition of zinc oxide may yield a zero stress-optic response in otherwise photoelastic glasses. By examining whether or not these glasses fit the predicted photoelastic response, a better understanding of the model's applicability will be established, which may lead to new lead-free zero stress-optic glass.

In the second chapter, the concepts upon which the rest of the work depends are described in detail. The nature of glass is accounted for and compared with other materials. Important theories from glass science are given to help establish a framework for studying glass structure. Photoelasticity is explained and a quantitative description of the stress-optic coefficient is derived. In section 2.2.2, current and historical theories of photoelasticity are presented and compared. The development of the empirical model discussed throughout this thesis is documented so that it is clear what work is left to be done. Section 2.2.3 describes the previous work that has been carried out to better understand the empirical model and photoelasticity in glass containing ZnO.

Chapter 3 describes all of the experimental methods used in this investigation and the reasoning behind each choice of technique. An overview of sample preparation techniques is also given for each type of glass studied. Extended X-ray Absorption Fine Structure spectroscopy (EXAFS), the primary means of studying glass structure used in this work, is described in considerable detail since the use of EXAFS is new to this line of research. The theoretical basis of EXAFS is given in addition to practical considerations for carrying out EXAFS experiments at a synchrotron beamline. A brief

introduction to EXAFS data processing and analysis follows, with a more complete guide available in Appendix A. Raman spectroscopy was also used to study glass structure, so a brief description of the instrument and experiment is included. The Sénarmont compensator method for measuring the stress-optic coefficient is explained, as is the apparatus used. Chapter 3 concludes with descriptions of the Archimedes method used to measure density and the refractive index measurements done using Abbe refractometry and spectroscopic ellipsometry.

In Chapter 4, all experimental results are presented for each of the three zinc-containing glasses studied. Density measurements are presented, from which values of molar volume are obtained. Density is used as a simple check for whether or not a glass composition matches the composition that was intended to be prepared. Experimental EXAFS spectra and the corresponding fits resulting from data analysis are shown in momentum and position space. Coordination numbers and bond lengths extracted from the EXAFS data are tabulated. Raman spectra, when used, follow the EXAFS results. Stress-optic coefficients were measured using two methods and the results of each are given, followed by refractive index measurements.

Chapter 5 contains the discussion and interpretation of the preceding results. Conclusions are made about the probable structure present in the various glass samples measured. The structure and photoelastic measurements allow for an evaluation of how well the empirical model performs for each type of glass, and the potential for zinc oxide to contribute to a zero stress-optic response is discussed.

The final chapter summarizes the work done in context of the greater effort to design new lead-free zero stress-optic glasses. The accomplishments and shortcomings of the project are outlined and opportunities for future work are highlighted. The primary conclusions drawn from experimental results are restated and their implications discussed, followed by closing remarks.

Considerable work has been done to understand the correlation between local structure and photoelasticity in oxide glasses. This thesis takes inspiration from many other works completed by scientists who have worked in this area over many years. It certainly would not have been possible without access to the expertise of my colleagues

and mentors. I hope that my work proves to be a useful contribution to the field and that others may learn from it, as I have from the work of those who came before.

Chapter 2

Background

2.1 The Structure of Glass

As this thesis discusses the relationship between structure and photoelasticity in glass, it is important to first develop a general description of the structure of glass. Glass is a material that is ubiquitous in our society and common in homes, vehicles and workplaces, but the nature of this extremely common material is not always well understood. One could easily describe what glass is *like*, based on its macroscopic properties – it is often transparent and may shatter when dropped, for example. However, to explain what glass actually is, is more challenging. To understand the nature of glass, and what makes this material different from other types of solids, one must investigate its structure at the atomic level, as glass scientists have been doing for many decades.

Glass is an amorphous solid, meaning that it has the rigidity of a solid, but the structural disorder of a liquid or gas. Typically, solids possess some type of long-range ordering – some repeating pattern of atoms, molecules or larger structural units constructed thereof. Liquids and gases are amorphous, meaning they have no long-range order, since their constituent atoms or molecules are able to move freely and orient themselves in any direction. Certain types of materials are capable of maintaining their disordered state during a liquid to solid phase transition, if they are cooled sufficiently rapidly. While some metals, waxes and thin films can be found in an amorphous state, glasses are the most commonly encountered type of amorphous solid.

The process by which glass becomes a solid is what makes it unique. When a liquid is cooled, it will typically solidify into an ordered state at its melting temperature, undergoing a sudden decrease in volume. A glass will instead experience a gradual decrease in volume and corresponding increase in viscosity below the melting

temperature. The intermediate phase between the liquid melt and solid glass is referred to as a *supercooled liquid*. The temperature at which the specific viscosity of the supercooled liquid reaches 10^{13} Pa·s is called the *glass transition temperature* or T_g. The gradual change from liquid to solid is referred to as the *glass transition,* and is what makes glass unique compared to other amorphous solids. Some glasses are very stable and will remain amorphous indefinitely below T_g. Others are less stable and quickly crystallize.

Several theories have attempted to describe the structure of glass since the inception of glass science. The crystallite hypothesis proposed by Lebedev [12] suggested that glass is made up of many very small crystals. While this theory was initially supported by others [13] and seemed to be backed by experimental evidence [14], the crystallite hypothesis lost favour as experiments were unable to detect any crystallite segments in glass [15]. Zachariasen published a competing theory, known as the random network theory, in 1932 [16]. The random network theory has become much more well-accepted and is the dominant viewpoint held by glass scientists today.

The random network theory states that, unlike a crystalline material consisting of a regular pattern of some repeating structural unit, the analogous glass is made up of a network of the same type of structural units, but they are randomly distributed and oriented. While the bonding energetics of the crystalline and glass forms are similar, all periodicity and symmetry of the crystal network is absent in a glass. Warren *et al*., who supported the random network theory, acknowledged that some small crystallite segments may exist in glass, but believed them to be of negligible size [17]. The phenomenon of the glass transition can be explained by the random network theory, since the many different bonding configurations of the random network require a wider range of energies to be broken or formed, causing a gradual rather than sudden phase transition. Fig. 2.1 illustrates the difference between an ordered crystalline material and a random glass network.
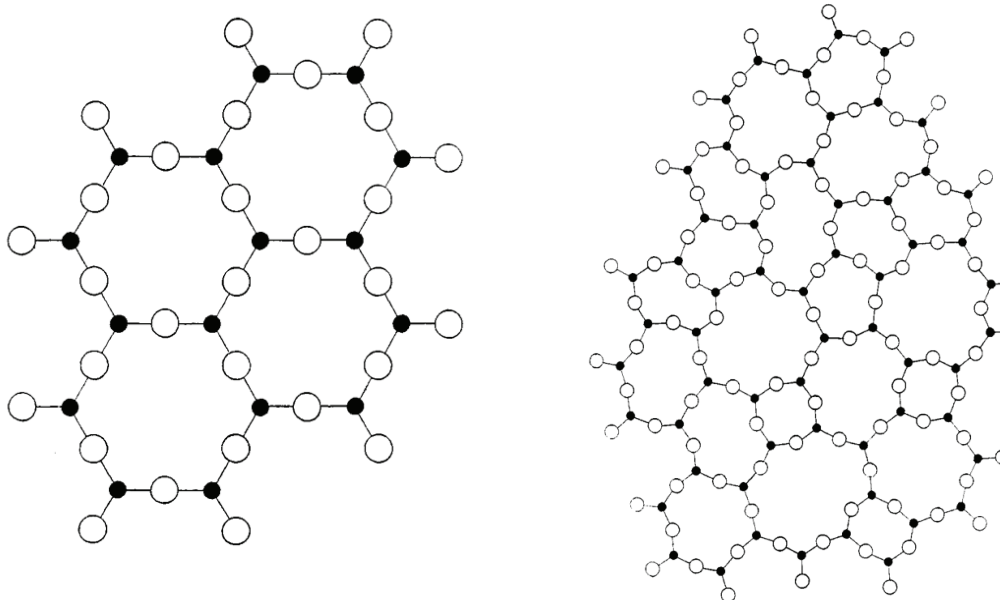
Fig. 2.1: An illustration of a crystalline (left) and glass (right) network of the same compound [17]

In order for it to be energetically favourable to form a glass, the random network must not have a potential energy vastly different from that of a periodic structure. This requirement gives limitations on which types of compounds are able to form glasses. Zachariasen gives 4 rules that an oxide must obey for the formation of a glass:

1. An oxygen atom is linked to no more than 2 cations.
2. The cation coordination number must be small.
3. Polyhedra share corners rather than faces or edges.
4. At least 3 corners of each polyhedron must be shared.

There are only a relatively small number of oxide compounds that fit all of these conditions. Compounds that are able to form a glass on their own are referred to as *glass network formers*. Some common glass network formers are SiO_2, B_2O_3, P_2O_5, GeO_2 and TeO_2. Other compounds are able to participate in the glass network but cannot form a glass on their own. These are called *glass network modifiers*, and tend to break up the glass network and introduce non-bridging oxygen (NBO) atoms. Modifiers are often added to all types of glass to achieve desirable properties. Some compounds can act as both formers and modifiers and are therefore referred to as *intermediate oxides*. In this work, the glass network formers P_2O_5, B_2O_3 and TeO_2 are considered, each with the

addition of the intermediate oxide ZnO, which has been shown to affect many physical and optical properties of the glasses to which it is added [18-20].

Phosphate glasses are made directly from P_2O_5 or from a phosphate compound such as $NH_4H_2PO_4$. The phosphate glass network is made up of corner-sharing PO_4 tetrahedra. Phosphate glasses have a number of potentially useful properties, including high thermal expansion coefficients, low melting temperatures and high UV transmission [21]. Phosphate glasses have a number of biomedical applications [22] and can also be used in high-power lasers [23] and high-gain optical amplifiers [24].

Borate glass is typically made by melting powdered B_2O_3 or using boric acid (H_3BO_3). Pure borate glass consists of a three-dimensional network of corner-sharing BO_3 triangles that may become BO_4 tetrahedra if a modifier is added. Borate glass has applications in linear and nonlinear optics [25]. Borate glasses containing SiO_2, called borosilicate glass, are very commonly used for laboratory glassware and heat resistant cookware.

Tellurite glass is made by melting powdered TeO_2. The tellurite glass network consists of TeO_4 trigonal pyramids that can become TeO_3 trigonal bipyramids if the network is modified. Tellurite glasses have several interesting optical properties such as a high refractive index and large third-order nonlinear susceptibility [26], and are therefore used primarily for optical applications such as fiber optic communication systems, nonlinear optical devices and lasers [18]. Tellurite glasses have significant advantages over phosphate and borate glasses as they have a much lower melting temperature and are non-hygroscopic.

2.2   Photoelasticity

Annealed, homogenous glass is typically optically isotropic, meaning that its index of refraction is the same in all directions [27]. If a uniaxial mechanical stress is applied to glass, the isotropy can be broken: the index of refraction in the extraordinary (stressed) direction may become different than those in the other (ordinary) directions. A material

with an index of refraction that depends on the direction of propagation or polarization state of light is said to exhibit birefringence. Birefringence can introduce undesired effects in optical applications where image distortion must be minimized. Stress-induced birefringence is called *photoelasticity*, or *the photoelastic effect*. Photoelasticity is a large and problematic effect in some types of glass, while in others it is very small or absent altogether. Several theories have attempted to explain or predict photoelasticity [5, 10, 11], although no complete physical explanation has been developed yet.

2.2.1   The Stress-Optic Coefficient

In a birefringent sample, the difference between the extraordinary and ordinary refractive indices is

$$\Delta n = n_e - n_o. \tag{2.1}$$

When the birefringence, Δn, is induced by an applied stress σ, the two quantities are proportional:

$$\Delta n = C\sigma. \tag{2.2}$$

The constant of proportionality, C, between applied stress and induced birefringence is called the *stress-optic coefficient* and has units called brewsters. In SI units, 1 brewster = 1 TPa^{-1}. Birefringence is difficult to measure directly, but the optical path length difference due to birefringence can be obtained experimentally using an optical apparatus known as a compensator. A compensator, such as the Sénarmont or Babinet-Soleil compensator, actually measures a phase retardation introduced by a birefringent sample, which can then be converted into an optical path length difference (The optical path length is the geometric path length multiplied by the index of refraction). The optical path length travelled by a light ray in the extraordinary direction will be different than that of the ordinary direction, and the path length difference δ is related to σ and the sample thickness l as

$$\delta = Cl\sigma. \tag{2.3}$$

Therefore, by measuring δ using a compensator, one can determine the stress-optic coefficient of a glass sample. Birefringence, and therefore stress-optic coefficients, can be either positive or negative. Conventionally, a sample with a higher refractive index in the extraordinary direction is said to have positive birefringence (and a positive stress-optic coefficient), while a sample with a lower refractive index in the extraordinary direction is said to have negative birefringence (and a negative stress-optic coefficient) [27].

The stress-optic coefficient C as described above represents a special case derived from the general photoelastic tensor elements π_{ij}. In the case of a uniaxial material, the relative magnitude and directions of the three refractive indices can be described by an ellipsoid called the indicatrix with the Cartesian principal axes y_i, where i = 1, 2, 3 and i = 3 is the extraordinary axis:

$$\frac{y_1^2}{n_1^2} + \frac{y_2^2}{n_2^2} + \frac{y_3^2}{n_3^2} = 1. \tag{2.4}$$

The relative dielectric impermeability B_i, a tensor representing the inverse of dielectric permittivity, is defined as

$$B_i = \frac{1}{n_i^2}, \tag{2.5}$$

so equation (2.5) can be rewritten as

$$B_1 y_1^2 + B_2 y_2^2 + B_3 y_3^2 = 1, \tag{2.6}$$

or for an arbitrary orientation of axes,

$$B_{ij} y_i y_j = 1, \tag{2.7}$$

where it is understood that repeated indices are to be summed over. An applied mechanical stress σ_{ij} will change the coefficients B_{ij} by

$$\Delta B_{ij} = \pi_{ijkl} \sigma_{kl}, \tag{2.8}$$

12

where π_{ijkl} represents the full 81-element photoelastic or piezo-optic tensor. Each element of the tensor is called a stress-optic coefficient and has units of Pa^{-1}. The notation can be modified by summing to 6 rather than 3 and only using 2 indices, writing π_{ij}. When considering an isotropic glass, many of the elements are interdependent:

$$\pi_{11} = \pi_{22} = \pi_{33},$$

$$\pi_{12} = \pi_{21} = \pi_{13} = \pi_{31} = \pi_{23} = \pi_{32}, \tag{2.9}$$

$$\pi_{44} = \pi_{55} = \pi_{66} = [\pi_{11} - \pi_{12}].$$

Only two elements are independent, and equation (2.8) can be reduced to

$$\Delta B_i = \pi_{ij}\sigma_j \tag{2.10}$$

which can be readily solved in the case of a uniaxial stress σ_3. The solutions for Δn_1 and Δn_3 are

$$\Delta n_1 = -\frac{n^3}{2}\pi_{13}\sigma_3 \tag{2.11}$$

and

$$\Delta n_3 = -\frac{n^3}{2}\pi_{33}\sigma_3. \tag{2.12}$$

Where n is the refractive index of the unstressed glass. For light propagating in the y_2 direction,

$$\Delta n_3 - \Delta n_1 = -\frac{n^3}{2}[\pi_{33} - \pi_{13}]\sigma_3. \tag{2.13}$$

By comparison with equation (2.2), the relationship between the stress-optic coefficient C and the photoelastic tensor elements π_{ij} becomes clear:

$$C = -\frac{n^3}{2}[\pi_{33} - \pi_{13}]. \tag{2.14}$$

2.2.2   Theories of Photoelasticity

One of the earliest attempts to develop a theory to explain photoelasticity was published by Mueller in 1938 [10]. Mueller described how strain affects crystals and amorphous materials and theorized that deformations of the atomic lattice and of atoms themselves contribute to the photoelastic effect. The effects of strain were separated into two types: the *lattice effect*, describing changes in the arrangement of atoms as the lattice is strained, and the *atomic effect*, describing polarization of the electron clouds of atoms themselves.
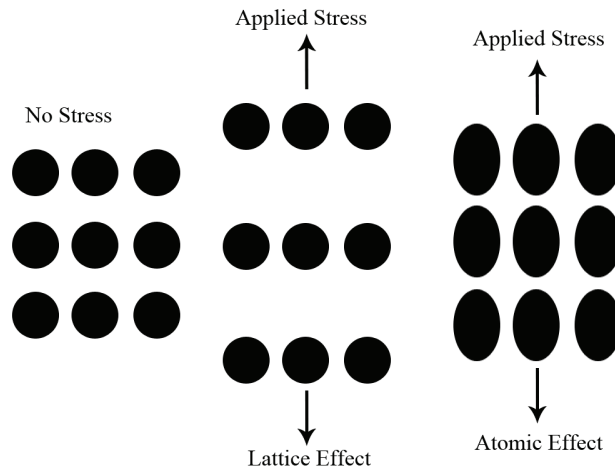
Fig. 2.2: 2-Dimensional illustration of the lattice and atomic effects under uniaxial mechanical stress

Mueller stated that the lattice effect reduces the stress-optic coefficient, while the atomic effect increases it by creating optical anisotropy in the atoms. In a cation-oxygen chain, oxygen atoms bridging two cations are highly polarized under tensile stress. Non-bridging oxygen (NBO) atoms, being connected to a single cation, are polarized to a much lesser degree. The greater atomic effect in bridging oxygen atoms, according to Mueller's theory, means that they contribute to a large positive stress-optic coefficient, while NBO reduce the coefficient. Since more NBO are present when a glass modifier bonds ionically, a conclusion of Mueller's theory is that the addition of compounds that form ionic bonds in a glass could minimize the photoelastic effect.

Another model, proposed by Weyl [11], attempts to account for photoelasticity in terms of electrostatic interactions and the polarizability of ions in a glass. Unlike Mueller, Weyl believed that as the distance between atoms increases due to tensile stress, electrostatic interactions weaken in the stressed direction and therefore the electron cloud is elongated in the direction perpendicular to the stress. The increased electron density in the perpendicular direction may polarize neighbouring cations in the stressed direction. Using Weyl's model, predictions about the photoelastic response have been made by considering the ratio of polarizabilities between anions and cations [28]. In a glass containing an oxide of the form M_xO_y, the polarizability ratio ξ is given as the ratio of the cation polarizability α_M to anion polarizability α_O:

$$\xi = \frac{x\alpha_M}{y\alpha_O}. \tag{2.15}$$

Photoelastic measurements of several types of glass indicate that a larger value of ξ is correlated with a smaller stress-optic coefficient. While this model relies only on the deformation of ionic bonds, negative stress-optic coefficients can arise from the covalent behaviour of modifier cations added to a glass. Weyl's model may be helpful in certain cases, but its range of applicability is limited since it does not account for covalent bonding.

2.2.3   The Empirical Model of Photoelasticity

In the 2000s, Zwanziger *et al.* began investigating relationships between structure and photoelasticity in oxide glasses [29]. It was shown that in addition to polarizability, the local structure surrounding cations in a glass can also play an important role in determining the stress-optic response [5]. It is believed that longer, more metallic bonds can be polarized in the direction of the bond or orthogonal to it. The non-directional characteristic of bond polarization is necessary to have $\pi_{11} = \pi_{12}$, which gives $C = 0$ according to equation (2.14). Coordination number can also play an important role, as a structure with high coordination throughout would experience bond deformation in many directions under anisotropic stress, regardless of bond metallicity. Therefore, it was

suggested that long bonds and low coordination numbers could be favourable for reducing the stress-optic coefficient.

To account for bond lengths d and coordination numbers N_c with a single parameter, the ratio d/N_c was considered. d/N_c was computed for many different materials with known stress-optic coefficients, some of which are shown below:

Table 2.1: A sample of the data used to establish the empirical model of photoelasticity [5]

Compound	d/N_c (Å)	Sign of C
HgO	1.03	-
PbO	0.58	-
ZnO	0.50	+
TeO_2	0.50	+
B_2O_3	0.46	+
P_2O_5	0.38	+

Among the materials considered, there was a clear correlation between d/N_c and the sign of the stress-optic coefficient. When ordered from high d/N_c to low, the materials with negative stress-optic coefficients all appear at the top of the list with all of the positive stress-optic materials below. The threshold between negative and positive is near $d/N_c =$ 0.5 Å. Therefore, it was proposed that a zero stress-optic glass could be obtained if the average d/N_c for all oxide components of a glass was near 0.5 Å. This model, referred to as the empirical model of photoelasticity, is summarized by the formula

$$\sum_i x_i \left(\frac{d}{N_c}\right)_i \approx 0.5 \text{ Å},$$ (2.16)

where the sum is taken over the i components of the glass each with mole fraction x_i.

In an effort to discover new types of zero stress-optic materials using the empirical model, glasses were made from compounds whose crystal structure would yield a d/N_c ratio near 0.5 Å. This method has been used to successfully predict several types of glass for which a zero stress-optic composition can be made [5, 30]. Tin phosphate, tin silicate, antimony borate and barium tellurite glass were all shown to have a positive

stress-optic coefficient at low modifier concentration which decreases through zero as the amount of modifier increases. The zero stress-optic composition was generally predicted with an error of about 15%. Additionally, it was shown that the structure of the network modifier is not solely responsible for changes in d/N_c that correlate with photoelasticity. Network formers may also experience changes in their coordination that affect d/N_c over a range of compositions. The successful prediction of the photoelastic response in these glass compositions has been an important step forward in the development of a widely applicable and environmentally safe lead-free zero stress-optic glass.

The empirical model suggests that compounds with a particularly high or low d/N_c value should have an obvious effect on the stress-optic coefficient when added to a glass: those with $d/N_c \gg 0.5$ Å should decrease the coefficient, while those with $d/N_c \ll$ 0.5 Å should increase it. Other compounds, however, may have less predictable effects. It is not clear from the current formulation of the empirical model what the effect of adding a modifier whose d/N_c ratio is very near 0.5 Å would be. Crystalline ZnO has a 4-coordinate tetrahedral structure with Zn-O bond lengths of about 1.98 Å [5]. Therefore, its d/N_c ratio is just below 0.5 Å, lying on the threshold between contributing to a positive or negative stress-optic response, according to the model. By studying the photoelastic response of oxide glasses to which ZnO has been added, the empirical model and the transition between positive and negative birefringence could become better understood. It is not well known if the coordination of ZnO in a glass changes significantly compared to the crystalline form, and this would alter the result of the model. Therefore, it is important to accurately determine the local structure surrounding Zn cations in each glass when examining the relationship between d/N_c and the stress-optic coefficient.

2.3   Previous Work

Since the development of the empirical model, work has been done to develop a better understanding of its applicability and limitations. The first few zero stress-optic glasses

successfully predicted by the model had in common that they were modified by p-block metal oxides with low coordination numbers [5]. While it would seem intuitive that a low coordination number would be required to increase d/N_c and decrease the stress-optic coefficient, later work indicated that this is not the case. Barium tellurite glass was also shown to have a zero stress-optic coefficient, in agreement with the model [30]. Barium oxide is characterized by a high coordination number but modifies the tellurite network such that the average coordination number in the glass may still decrease. New possibilities for zero stress-optic glass became evident since there was no restriction to only a few glass modifiers having low coordination. With new possibilities came new challenges, though, as it became more important to understand the relationship between glass modifier and network former, since one can affect the coordination of the other.

In 2011, Dr. Vincent Martin completed a PhD thesis examining the structural dependence of the photoelastic response in oxide glass. In an effort to test the empirical model and the theories of photoelasticity that stood before it, many families of binary and ternary oxide glasses were prepared and analyzed. The effects of adding lead, tin, antimony, cadmium and zinc to the traditional glass network formers (silicate, borate and phosphate) were studied. Whereas the empirical model originally only took into account the crystal structure of the constituent oxides in a glass, Dr. Martin's work served to establish the practice of measuring coordination numbers and bond lengths *in situ* to obtain a more accurate d/N_c parameter. By accurately measuring d/N_c over a range of compositions, the 15% error with which a zero stress-optic composition could previously be predicted was greatly improved, to around 2% in some cases. The work on glasses containing ZnO allowed for future investigation, as only the structure of the glass former was studied. No definitive conclusion could be made about how the empirical model applies to these glasses, since the methods used were not suitable for determining the Zn coordination environment.

Martin's results indicate that adding ZnO to a phosphate or borate glass will increase the stress-optic coefficient. Based on the crystal structure d/N_c parameter for ZnO being near 0.5 Å, it would be expected that the coefficient would decrease. The empirical model could not explain the evolution of the photoelastic response in these glasses, unless the coordination of ZnO changed significantly in the glass compared to its

crystalline form. Clearly it is important to accurately determine the local structure surrounding Zn when it is added as a glass network modifier to explain the unexpected trend in the stress-optic response and determine whether or not the empirical model applies to zinc-modified glass.

The work already completed on phosphate and borate glasses allows the focus of this work to remain primarily on measuring the ZnO coordination environment. Phosphate and borate glasses are relatively easy to prepare and work with and therefore provide a good platform for studying the unexplained relationship between structure and photoelasticity over a range of compositions. Phosphate glass is particularly appealing, as the P-O coordination number and bond length have been found to be effectively independent of composition [31]. Therefore, any changes in d/N_c are due solely to the behaviour of ZnO. Zinc borate glass provides an alternative case, where the addition of the modifier clearly induces a coordination change in the borate glass network.

Tellurite glasses have useful optical properties [26] but little work has been done on studying their photoelastic response. Barium tellurite glass was shown to be capable of a zero stress-optic response, so the same result may be possible with other types of modifiers. A zinc tellurite glass is quite basic to prepare and provides three opportunities: to measure the ZnO coordination to add to the data from the phosphate and borate glasses, to test the empirical model of photoelasticity on a new type of glass, and to document the stress-optic response of a glass for which photoelasticity has not been studied.

Chapter 3

Experimental Techniques

3.1   Sample Preparation

Overview

Glass samples were prepared by melting and quenching mixtures of reagent-grade powders from Sigma-Aldrich. Powders were first mixed in the appropriate stoichiometric ratio for the desired glass composition in a glass beaker. Mixtures were transferred into platinum crucibles and then placed into a pre-heated box furnace in air. After melting, the glasses were quickly poured into a mold to quench and cool. For the XAFS experiment, glass pieces were ground into powder under inert atmosphere inside of a glove box using a mortar and pestle. The powdered glass samples were sealed in vials and brought to the beamline. For optical measurements, bulk glasses were annealed to remove internal stress then cut and polished using water or ethanol, depending on the chemical durability of the glass, to obtain parallel, optically smooth sides.

3.1.1 Zinc Tellurite (ZnO-TeO$_2$) Glass

ZnO (Sigma-Aldrich, <5 micron 99.9%) and TeO$_2$ (Sigma-Aldrich, ≥99%) powders were used to obtain ZnO-TeO$_2$ glasses. The powders were mixed in the appropriate ratios for the desired compositions, and then melted in a platinum crucible in a box furnace at approximately 800°C for 15 to 20 minutes. The melts were poured into a steel mold on a hot plate at 420°C to prevent cracking and formed a clear, yellow glass. 6 samples were

successfully prepared with varying ZnO and TeO_2 molar fractions. Samples were assigned a label according to their ZnO molar percentage:

Table 3.1: Zinc tellurite glass samples

Sample ID	Composition
ZT15	$ZnO_{(.15)}$-$TeO_{2(.85)}$
ZT20	$ZnO_{(.20)}$-$TeO_{2(.80)}$
ZT25	$ZnO_{(.25)}$-$TeO_{2(.75)}$
ZT30	$ZnO_{(.30)}$-$TeO_{2(.70)}$
ZT35	$ZnO_{(.35)}$-$TeO_{2(.65)}$
ZT40	$ZnO_{(.40)}$-$TeO_{2(.60)}$

The samples were all approximately 15 x 10 x 3 mm in size. When viewed through crossed polarizers, the glasses clearly contained residual stresses as evidenced by their birefringence. To remove stresses, the glasses were placed back into the box furnace below the glass transition temperature T_g at 325°C for 10 hours. After 10 hours, the furnace was switched off and the samples were left inside overnight to cool slowly without cracking.
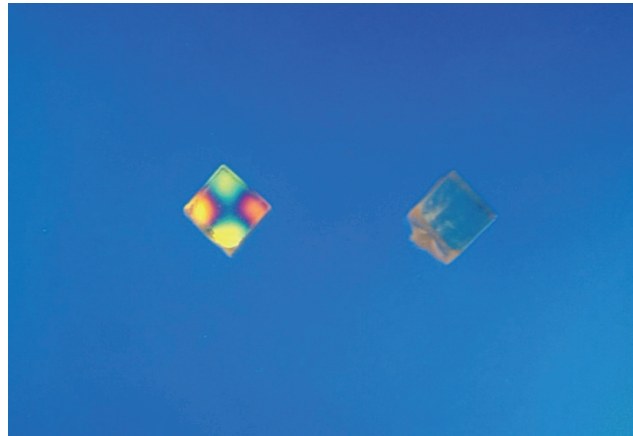

Fig. 3.1: Zinc tellurite glass before (left) and after (right) annealing, viewed through crossed polarizers to show residual stress

Annealed samples were transferred into a glove box and partially ground into powder to be used for XAFS measurements. A bulk piece of each sample was stored to be later cut and polished for optical measurements. Cutting was done using a low-speed saw with water as a coolant to obtain two parallel sides. The sides were polished using silicon carbide polishing pads and then diamond paste of decreasing grit down to 3 micron. Water was used as lubricant for polishing.

### 3.1.2 Zinc Borate (ZnO-B$_2$O$_3$) Glass

The zinc borate samples studied were prepared by Dr. Vincent Martin during his PhD in August of 2010 by a similar melt-quench method as above [28]. Powders (ZnO, Sigma-Aldrich 99.9% and B$_2$O$_3$, Sigma-Aldrich 99%) were mixed in platinum crucibles and heated in a box furnace at 1200°C for 30 minutes. Melts were poured into a room temperature brass plate then moved immediately to a 320°C hot plate. The samples were annealed between 490 and 530°C to remove stress. Four samples were obtained:

Table 3.2: Zinc borate glass samples

Sample ID	Composition
ZB30	ZnO$_{(.30)}$-B$_2$O$_{3(.70)}$
ZB40	ZnO$_{(.40)}$-B$_2$O$_{3(.60)}$
ZB50	ZnO$_{(.50)}$-B$_2$O$_{3(.50)}$
ZB60	ZnO$_{(.60)}$-B$_2$O$_{3(.40)}$

3.1.3 Zinc Phosphate (ZnO-P$_2$O$_5$) Glass

The reagents used to obtain the ZnO-P$_2$O$_5$ glasses were NH$_4$H$_2$PO$_4$ (Sigma-Aldrich ACS reagent ≥98%) and ZnO (Sigma-Aldrich, <5 micron powder 99.9%) according to the reaction [32]

$$ZnO + 2NH_4H_2PO_4 \rightarrow ZnO\text{-}P_2O_5 + 3H_2O + 2NH_3. \tag{3.1}$$
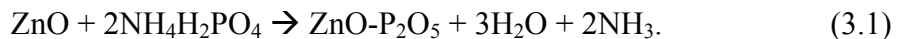
The powder mixtures in a platinum crucible were placed into a pre-heated box furnace at 1100^oC for approximately 1 hour. 6 samples were successfully prepared with varying molar fractions of ZnO and P_2O_5. Samples were assigned a label according to their ZnO molar percentage:

Table 3.3: Zinc phosphate glass samples

Sample ID	Composition
ZP45	$ZnO_{(.45)}-P_2O_{5(.55)}$
ZP50	$ZnO_{(.50)}-P_2O_{5(.50)}$
ZP55	$ZnO_{(.55)}-P_2O_{5(.45)}$
ZP60	$ZnO_{(.60)}-P_2O_{5(.40)}$
ZP63	$ZnO_{(.63)}-P_2O_{5(.37)}$
ZP645	$ZnO_{(.645)}-P_2O_{5(.355)}$

Samples varied in size but were generally near 12 x 8 x 5mm. All zinc phosphate glasses prepared by this method contained a small number of bubbles due to the presence of water vapour and NH_3. Samples were partially ground to powder in the glove box to be used for XAFS and bulk pieces were stored to be later cut and polished for optical measurements. Cutting was done using ethanol as a coolant due to the hygroscopic nature of the samples. Polishing was done using ethanol as well, again on silicon carbide polishing pads and using diamond paste down to 3 micron grit.

3.2   X-ray Absorption Fine Structure (XAFS) Spectroscopy

XAFS is a spectroscopic technique used for determining local structure around a selected atom in a sample. Since XAFS probes the atomic and molecular scale, there is no requirement for long-range order, crystallinity or other bulk properties in a material. Due to the amorphous nature of glass, certain materials characterization techniques that exploit long range ordering, such as X-ray Diffraction, are inconvenient for determining glass structure. XAFS, however, is well suited for studying amorphous materials [33].

In many cases, structure in oxide glass systems can be studied using Nuclear Magnetic Resonance (NMR) or Mössbauer spectroscopy. However, it has been shown that in practice, Mössbauer spectroscopy using ^{67}Zn nuclei results in a poor signal to noise ratio [34]. ^{67}Zn is also the only NMR-active zinc nucleus, but gives a broad (~500ppm) signal [35], making it challenging to extract meaningful information about zinc structure from such an experiment. Zinc K-edge XAFS is a straightforward experiment capable of producing high quality data [36]. Therefore, XAFS is the method of choice in this work for determining the local structure surrounding zinc in the zinc-containing glasses.

3.2.1 XAFS Theory

XAFS is based on the photoelectric effect. In an XAFS experiment, x-ray photons are absorbed by core-level electrons of a selected type of atom in a sample. The resulting photoelectrons may be freed from their host atoms if the incident x-ray energy is equal to or greater than the core-level binding energy. Photoelectrons scatter from neighbouring atoms, resulting in interference effects that are characteristic of the local structural environment. By examining absorption data, one can extract information about the photoelectron scattering process and hopefully gain knowledge about the structure of the sample material.

A quantum mechanical description is necessary to describe fully the phenomenon behind XAFS. In order for a photoelectron to be promoted from an atom, there must be an available final state, and the process is mediated by an interaction Hamiltonian. In XAFS, one measures the absorption coefficient $\mu(E)$, which depends on the amount of the total x-ray intensity which is absorbed by the sample. Since absorption depends on the presence of an available final state, $\mu(E)$ can be described by Fermi's Golden Rule [37]:

$$\mu(E) \propto \ |\langle i|H|f\rangle|^2 \delta(E_f - E_i). \qquad (3.2)$$

Here $\langle i|$ represents the initial state consisting of an incident photon and core electron, and $|f\rangle$ represents the final state with a core hole and outgoing photoelectron. H is the interaction Hamiltonian. The delta function requires energy conservation between the initial and final states. Neighbouring atoms do not contribute to the initial state since the core electron is tightly bound within the atom. In the final state, however, the affect of neighbouring atoms on the photoelectron must be considered. To accomplish this, the final state can be decomposed into a central atom portion and a neighbouring atom portion:

$$|f\rangle = \ |f_0\rangle + \ |\Delta f\rangle. \qquad (3.3)$$

Using this decomposition, the expression for the absorption coefficient becomes:

$$\mu(E) \propto \ |\langle i|H|f_0\rangle + \langle i|H|\Delta f\rangle|^2. \qquad (3.4)$$

Expanding to 1st order in Δf:

$$\mu(E) \propto \ |\langle i|H|f_0\rangle|^2 \left[1 + \langle i|H|\Delta f\rangle \frac{\langle f_0|H|i\rangle^*}{|\langle i|H|f_0\rangle|^2} + C.C. \right]. \qquad (3.5)$$

As the factor in front is just the absorption coefficient due only to the core atom, the above can be rewritten as

$$\mu(E) = \ \mu_0(E)[1 + \chi(E)], \qquad (3.6)$$

which shows that $\chi(E)$, denoted Extended X-ray Absorption Fine Structure (EXAFS), represents the fractional change in the absorption coefficient due to the effects of the neighbouring atoms:

$$\chi(E) \propto \langle i|H|\Delta f\rangle. \qquad (3.7)$$

Quantum radiation theory gives the form of the Hamiltonian describing the interaction between the electron and the quantized radiation field $\mathbf{A}$ [38]:

$$H_{int} = -\frac{e}{2mc}(\mathbf{p} \cdot \mathbf{A}(\mathbf{r}, t) + \mathbf{A}(\mathbf{r}, t) \cdot \mathbf{p}) + \frac{e^2}{2mc^2}(\mathbf{A}(\mathbf{r}, t) \cdot \mathbf{A}(\mathbf{r}, t)). \tag{3.8}$$

When considering only the absorption of a single photon, the $\mathbf{A} \cdot \mathbf{A}$ term may be neglected since it corresponds to a process whereby the total number of photons changes by 0 or ±2. For a photon of wavenumber k and polarization vector ϵ, the remaining terms can be reduced to

$$H_{int} = -\frac{e}{m}\sqrt{\frac{\hbar}{2\omega}}e^{i(\mathbf{k} \cdot \mathbf{r} - \omega t)}\mathbf{p} \cdot \epsilon, \tag{3.9}$$

and for the current purpose it is sufficient to note that:

$$H_{int} \propto e^{ikr}. \tag{3.10}$$

Now to determine the form of $\chi(E)$, the interaction Hamiltonian can be placed between the initial and final states and integrated. The tightly bound core electron state is approximated as a delta function, and the final state is the wave function of the scattered photoelectron:

$$\chi(E) \propto \int dr\, \delta(r)e^{ikr}\,\psi_{scatt}(r) = \psi_{scatt}(0). \tag{3.11}$$

This is an important result as it demonstrates a fundamental aspect of XAFS: $\chi(E)$ is proportional to the amplitude of the scattered photoelectron at the location of the absorbing atom. The scattering properties of neighbouring atoms, encoded in $\chi(E)$, affect the photoelectron wave function at the core atom and modulate the absorption coefficient $\mu(E)$ in a way that can be measured.

The photoelectron wave function can be evaluated at the origin to develop an equation for $\chi(k)$, the EXAFS in k-space. The outgoing photoelectron can be described as a spherical wave of the form $\frac{e^{ikr}}{r}$, travelling a distance R to the nearest atom and

backscattering. The scattering event is described by an amplitude $f(k)$ and a phase shift $\delta(k) - \frac{\pi}{2}$, both characteristic of the atomic species of the scatterer. The scattered photoelectron travels as a spherical wave back to the origin. Each process makes a contribution to the wave function [39]:

$$\psi_{scatt}(0) \propto \frac{e^{ikR}}{R} f(k) e^{i\left[\delta(k) - \frac{\pi}{2}\right]} \frac{e^{ikR}}{R} = \frac{f(k) e^{i\left[2kR + \delta(k) - \frac{\pi}{2}\right]}}{R^2}. \tag{3.12}$$

The EXAFS, up to a constant of proportionality, is given by the real part of the above expression (where the shift of $-\frac{\pi}{2}$ was used so that result could be expressed using a sine, rather than cosine, function):

$$\chi(k) = \frac{f(k)}{R^2} \sin[2kR + \delta(k)]. \tag{3.13}$$

This is the contribution to $\chi(k)$ for a single scatterer in one coordination shell. A complete description requires a summation over j coordination shells and multiplication by N_j, the number of atoms in each shell:

$$\chi(k) = \sum_j \frac{N_j f_j(k)}{R_j^2} \sin[2kR_j + \delta_j(k)]. \tag{3.14}$$

Two important physical effects must be accounted for before the equation is in its final, usable form. Thermal disorder will result in small variations in the absorber-scatterer distances within a given shell. These variations can be described as a variance σ_j^2. The contribution to the EXAFS is a factor $e^{-2k^2 \sigma_j^2}$, if disorder is sufficiently small that interatomic distances can be considered normally distributed about their mean value. If disorder is so large that the Gaussian approximation does not hold, the distribution of atoms can be described in a more general way using a cumulant expansion [40].

The second effect to consider is that a photoelectron has a finite window of opportunity to contribute to the EXAFS. Inelastic collisions with electrons or phonons may destroy the final state's coherence, on which EXAFS depends. Additionally, the core hole has a limited lifetime before it is filled by a new electron. These processes can be taken into account by assigning a mean free path, $\lambda(k)$, to the photoelectron. The factor

$e^{-2R_j/\lambda(k)}$, which can be considered a damping factor for the spherical photoelectron wave, represents the probability that the photoelectron is able to successfully backscatter and return to the core atom without being inelastically scattered and without the core hole being filled. The exponential decay with increasing radial distance due to this factor is what makes EXAFS an inherently local probe [41]. Adding the thermal disorder and mean free path factors gives the final expression for the EXAFS:

$$\chi(k) = \sum_j \frac{N_j e^{-2k^2\sigma_j^2} e^{-2R_j/\lambda(k)} f_j(k)}{R_j{}^2} \sin\left[2kR_j + \delta_j(k)\right]. \tag{3.15}$$

This is called the EXAFS equation. Since its development in the 1970s [33], virtually all analysis of EXAFS data has been done using this equation. Modern EXAFS analysis software is essentially just a tool for fitting the EXAFS equation to experimental data.

3.2.2   XAFS Experimentation

XAFS experiments were carried out in transmission mode at the Hard X-ray Micro-Analysis (HXMA) beamline at the Canadian Light Source in Saskatoon, Saskatchewan. Powdered samples were diluted in Boron Nitride (BN) so that the measured XAFS signal would not be too strong. Some trial and error was necessary to determine the appropriate BN to glass ratio to give a reasonably sized edge step (near 1) in the absorption coefficient. BN and glass powder mixtures of about 100mg were prepared. The glasses having the highest zinc content were mixed in a 3:1 BN to glass ratio to give the correct signal strength, while glasses with the least zinc required a 1:2 ratio. A portion of each powder mixture was pressed into a pellet and sealed between two pieces of carbon tape. Any inhomogeneities across the area of the pellet such as pinholes or large grains could result in poor data and were avoided where possible. It was decided that vacuum conditions at the beamline were not necessary as the hygroscopic nature of the glasses would be negligible over the timescale of the experiment for samples sealed in tape.

The HXMA beamline employs a 1.9T superconducting wiggler as its x-ray source. The 3 detectors (I_1, I_2 and I_3) are ionization chambers filled with 100% N_2 gas. The experiment used a Si(220) monochromator crystal and Rh focusing mirror. A Zn foil was placed between I_2 and I_3 to provide a reference signal for Zn XAFS. A ZnO powder sample was also scanned to provide a more accurate reference for the Zn-O coordination environment in glass powder. Each scan was parameterized into 3 ranges (where 0eV was set at the Zn K edge): the pre-edge region, from -200 to -30eV, in steps of 10eV; the XANES region, from -30 to 50eV, in steps of 0.25eV; and the post-edge region, from 50eV to 16keV, in steps of 50eV. Each sample was scanned 2 or 3 times over the entire energy range, as beamtime permitted. Raw data files consisting of x-ray energies and intensities from each detector were produced and saved for later processing and analysis.

3.2.3   Data Processing and Analysis

All data processing and analysis tasks were performed using the Demeter software package, version 0.9.13, written by Bruce Ravel [42]. Demeter provides a graphical interface to FEFF and IFEFFIT, libraries of algorithms for XAFS analysis that are widely used within the XAFS community [43]. Demeter contains the applications Athena, which handles data processing, and Artemis, for data analysis.

The basic task of XAFS data processing is to convert raw data into $\chi(k)$, the function representing only the post-edge oscillations in the absorption signal, or "the EXAFS". Raw data is first converted into an absorption coefficient $\mu(E)$:

$$\mu(E) = -\ln\left[\frac{I_1}{I_2}\right]. \tag{3.16}$$

$\mu(E)$ is then normalized, background-subtracted and finally Fourier-transformed to obtain $\chi(k)$. Data analysis involves fitting EXAFS equations to a structural model to obtain a spectrum similar to the measured $\chi(k)$. A detailed description of data processing and analysis using Demeter is given in Appendix A.

Athena contains a plugin for compatibility with data files from CLS beamlines. The data were first converted into the absorption coefficient $\mu(E)$, as described in Appendix A. All scans of a given sample were aligned by referencing the Zn foil data that was simultaneously measured. When glitches existed in the data, they were removed using Athena's degitching tool. Glitches were only found in zinc tellurite glass data, likely due to inhomogeneities (grains, non-uniform thickness) in the samples. Background removal, normalization and Fourier transforms were all performed using Athena's default parameter choices. Repeated scans for each sample were merged into single $\chi(k)$ spectra and saved in Athena project (.prj) files.

EXAFS spectra from the Athena files were imported into Artemis one by one for analysis. In order to determine the scattering paths present in the sample, Artemis requires crystal structure information to be input via the FEFF module. A .cif file specifying the crystal structure of ZnO was used [44], as it is reasonable to assume a first coordination shell of oxygen surrounds all zinc atoms in each glass. When fitting data from the ZnO powder standard, single and double scattering paths from Zn and O in the first three coordination shells, out to 3.8Å, were used. When fitting glass data, only single scattering Zn→O paths from the first coordination shell (about 2.0Å) were used.

The parameters from the EXAFS equation that were varied during the fitting process were the amplitude factor S_0^2, the energy shift ΔE_0, the path length difference ΔR and the variance in the absorber-scatterer distance, σ^2. When fitting several shells for the ZnO powder, each shell required its own σ^2 parameter, as the variance in path lengths may be larger for longer paths. Also, ΔR was scaled by multiplying by the effective path length, so that the value increased for longer paths but only one parameter was required.

Fitting ranges in k and R-space were chosen such that the maximum amount of information would be used in the fit without negatively affecting the fit quality. The k-range used for most fits was approximately $k_{min} = 3$Å^{-1} to $k_{max} = 11$Å^{-1}. Some scans of zinc tellurite glasses had no usable signal in the range above 9Å^{-1} so the fitting range was decreased. In r-space, fitting ranges were all approximately $r_{min} = 1.0$Å to $r_{max} = 2.6$Å, a range encompassing the first coordination shell but no others.

The "goodness of fit" was measured by statistical values reported by Artemis, particularly the R-factor and reduced chi-square (not related to the EXAFS $\chi(k)$). The

results of the fitted parameters and their correlations also provided insight into whether or not a fit was physically justifiable. Acceptable conditions were generally that S_0^2 was between 0.7 and 1.0, that ΔE_0 was on the rising portion of the absorption edge, that ΔR was near zero within uncertainty and that σ^2 was positive-definite [45]. Correlations between parameters, which indicate how one parameter would change if another were modified from its best fit value [46], were sought to be less than 0.85, although this was not always possible for weaker data. High correlations are generally unavoidable in EXAFS when two parameters contribute to the signal in the same way; such as coordination number and σ^2 which both contribute to amplitude, or ΔE_0 and ΔR which both contribute to the phase. The correlations are accounted for in the calculated error bars. When these conditions were all achieved and the largest fitting ranges were used that did not worsen the "goodness of fit" values, the fit was considered final. Zn-O bond lengths and coordination numbers, along with the corresponding error bars, were recorded for each sample.

3.3   Stress-Optic Coefficient

Stress-optic coefficients were measured by two different apparatus to ensure accurate results. Both experiments employ the Sénarmont compensator method to convert birefringence into detectable phase retardation and then into a value for the stress-optic coefficient. The first set of measurements was taken using a Strainoptics PS-100-SF polarimeter. The PS-100-SF consists of a broadband light source and polarizer upon which the user places the stressed sample. Above the sample are a quarter wave plate and rotatable polarizer that the user looks through to measure angles of polarization. The second apparatus consists of a laser light source and optical components oriented horizontally.

    In each apparatus, the axis of the first linear polarizer is at 45° to the stress axis of the sample. The birefringent sample imparts elliptical polarization on the light, which then passes through the quarter-wave plate. The fast axis of the quarter-wave plate is aligned with the axis of the linear polarizer such that the extraordinary ray picks up a

phase difference θ relative to the ordinary ray [5]. The angle of maximum extinction is found using the rotating analyzer and is equal to $\theta/2$. The optical path length difference δ can then be determined from the equation $\delta = \theta\lambda$. By plotting δ against the applied stress σ, the stress-optic coefficient C can be found since $\delta = Cl\sigma$, where l is the sample thickness.
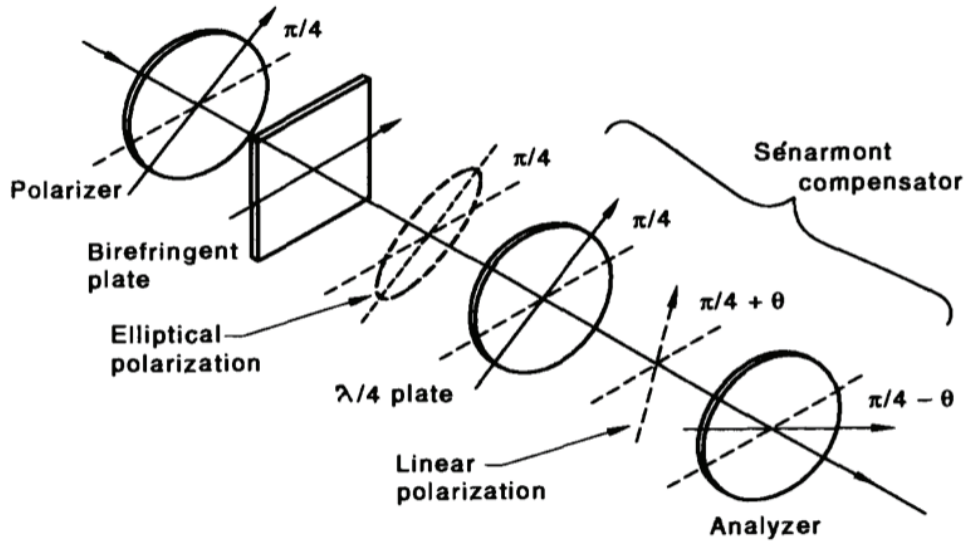

Fig. 3.2: The Sénarmont compensator method of measuring phase retardation due to a birefringent sample [47]

In the case of the Strainoptics polarimeter, the light source is a tungsten halogen bulb housed in the base of the unit and the linear polarizer is a plate fixed on top of the base. The sample is held in a motorized strain gauge that applies stress in one direction and outputs a reading in pounds. The quarter-wave plate and rotating analyzer are mounted above the sample. The user rotates the analyzer and uses their eye as the detector, visually determining the angle of maximum extinction by observing the appearance of the sample. Angles of extinction are recorded for various applied stresses so that a plot may be constructed to determine the stress-optic coefficient. Although the light source is white light, a wavelength of 575 nm is used in the calculation of δ, corresponding to the center wavelength of the quarter-wave plate. Since this method uses

white light and relies on a visual determination of the extinction angle, it is somewhat imprecise. A second method was used to obtain stronger results.

In the second method, the light source is a 594 nm HeNe laser. In front of the laser are a linear polarizer, the sample stage, a liquid crystal variable retarder (LCVR) acting as a quarter-wave plate, a computer-controlled analyzer and a detector to measure transmitted intensity. Each component is carefully aligned as it is installed by observing the location of back-reflectance. During the experiment, all components are kept in darkness behind a curtain to ensure an accurate and consistent intensity measurement. As before, applied stress is measured by the strain gauge. A computer program reads the intensity from the detector and automates the rotation of the analyzer. Applied stress and the angle of minimum intensity are recorded in a file. As above, the extinction angle is converted into an optical path length difference and the stress-optic coefficient is determined from the slope of the graph of δ vs. σ.

3.4   Raman Spectroscopy

Raman spectroscopy is used to detect the presence of particular structural units in a material by observing low-frequency modes associated with such units. Laser photons incident on a sample will excite vibrational, rotational or other types of modes and experience a corresponding shift up or down in energy as they are inelastically scattered, a process called Raman scattering. A Raman spectrum shows light intensity as a function of wavenumber shift. The locations of intensity peaks corresponding to various structures are well documented in the literature, so observing relative intensities of Raman peaks therefore provides information about relative quantities of structural units in a material. By comparing peak intensities in Raman spectra from a range of glass compositions, coordination changes can be detected as the glass network is modified. Raman spectra of zinc tellurite glasses were measured using a Nicolet NCR9650 Raman Spectrometer. A 1064nm NIR laser was used with a power of 0.3W. 450 scans for each sample were performed at a resolution of 4cm^{-1}.

3.5 Density

Density measurements were made using the Archimedes method with a Mettler-Toledo Density Measurement Kit. The kit allows the weight of a sample to be taken while the sample is immersed in a fluid. The apparatus, consisting of a beaker to hold fluid and a mechanism for lowering a pan containing the sample into the fluid, is placed atop a benchtop scale. The scale is zeroed and the sample is placed into the pan and lowered into the fluid. The scale's reading indicates the buoyancy (B) of the sample. By then measuring the sample's weight in air (W) and knowing the density of the fluid, the sample's density can be determined [48]:

$$\rho_{glass} = \rho_{fluid}\left[\frac{W}{B}\right].$$

(3.17)

3.6 Refractive Index

3.6.1 Abbe Refractometry

The refractive indices of zinc phosphate and zinc borate glasses were measured using an Atago DR-M4/1550 Abbe refractometer at 589nm. Abbe refractometry can provide very accurate measurements if the sample is well polished and of sufficient size. Samples must be polished on two perpendicular sides and must be between 15mm and 40mm long and 6 and 8mm wide. The refractometer requires a contact fluid with a greater refractive index than that of the sample. For zinc phosphate and borate glasses with n < 1.8, these fluids were readily available. However, zinc tellurite glasses have a refractive index near 2. Contact fluids of very high refractive index were not readily available and are highly toxic, so the only available option to measure the refractive index of zinc tellurite glasses was to use spectroscopic ellipsometry.

3.6.2 Spectroscopic Ellipsometry

Spectroscopic Ellipsometry was done using a J.A. Woollam Co., Inc. M2000F Spectroscopic Ellipsometer. To minimize back-reflection, samples were backed with clouded scotch tape and placed onto the stage of the ellipsometer with the tape side down. Each sample was measured using a 20 second scan time. The resulting data were fit with the CompleteEASE software package using the Cauchy Dispersion Law to determine the real part of the index of refraction [49]. B and C are the parameters allowed to vary in the relationship between index of refraction and wavelength:

$$n(\lambda) = B + \frac{C}{\lambda^2}. \tag{3.18}$$

Chapter 4

Results and Discussion

4.1 Zinc Tellurite Glass $ZnO_{(x)}$-$TeO_{2(1-x)}$

Crystalline ZnO and TeO_2 both have a d/N_c ratio of 0.50 Å. If the coordination environments of Zn and Te in the glass were the same as in their crystalline oxides, the empirical model would predict that all zinc tellurite glasses have a near-zero stress-optic coefficient. In reality, the TeO_2 glass network consists largely of TeO_4 trigonal bipyramid units and an increasing fraction of TeO_3 trigonal pyramids with the addition of a network-modifier such as ZnO [50]. As a higher fraction of TeO_3 units gives a decrease in average coordination number, it is expected that increasing the ZnO content will raise the d/N_c ratio for zinc tellurite glasses. While the structural properties of the ZnO-TeO_2 glass system are reasonably well documented in the literature [51-53], the photoelastic properties are not. Local structure and the photoelastic response of 6 zinc tellurite glasses were measured to determine how well this type of glass supports the empirical model. The Zn structural environment was measured by EXAFS and the Te environment was measured by Raman spectroscopy. Stress-optic coefficients were measured using the Sénarmont method as described in section 3.3.

4.1.1 Density

Densities of the zinc tellurite glasses were measured with the Mettler-Toledo Density Measurement Kit using the Archimedes method. Acetone, which has a density of

.790g/ml at 20°C, was used as the immersion fluid. Therefore, densities were calculated as

$$\rho_{glass} = .790 \left[\frac{Weight\ of\ glass\ in\ air}{Buoyancy\ of\ glass\ in\ acetone} \right] \frac{g}{cm^3}. \tag{4.1}$$

The molar volume of each glass was found by dividing the molar weight for $Zn_xTe_{1-x}O_{2-x}$ by the calculated density. Density values from the literature [54] are shown for comparison, where available.

Table 4.1: Density and molar volume of $ZnO_{(x)}$-$TeO_{2(1-x)}$ glasses

x	Density (g/cm³)	Density [54]	Molar Volume (cm³/mol)
.15	5.52 ± .07		26.8 ± .3
.20	5.50 ± .05	5.499 ± .005	26.2 ± .3
.25	5.49 ± .02		25.5 ± .1
.30	5.47 ± .04	5.445 ± .005	24.9 ± .2
.35	5.44 ± .02		24.3 ± .1
.40	5.41 ± .06	5.430 ± .005	23.4 ± .3

Measured density values overlap with the literature values, indicating that the nominal composition of each sample is likely an accurate representation of the true composition.

4.1.2 EXAFS

Zn EXAFS spectra of powdered zinc tellurite glasses were collected in transmission mode according to the procedure outlined in section 3.2.2 and analyzed as described in section 3.2.3 and Appendix A. In an effort to ensure reliability of the fits, careful attention was paid to their stability with respect to changing the k-range used. It was noted that small increases or decreases at the top or bottom of the range did not dramatically affect the resulting parameters. The largest k-range was used that did not statistically worsen the fit, although a larger range would have been desirable but was

limited by the quality of the data. The noisy spectrum at high k for sample ZT30 meant that a smaller than ideal k-range had to be used, to avoid larger uncertainties. Increasing k_{max} to beyond $k = 10$ Å^{-1} would generally be preferable if possible, although the criterion that the number of parameters be less than 2/3 of the number of independent points was still adhered to. Plots illustrating the first shell fit to the k^2-weighted $\chi(k)$ along with $|\chi(R)|$ are shown below for each sample. Due to a low signal to noise ratio, it was not possible to obtain a fit of reasonable quality for the sample ZT25.

a)

b)
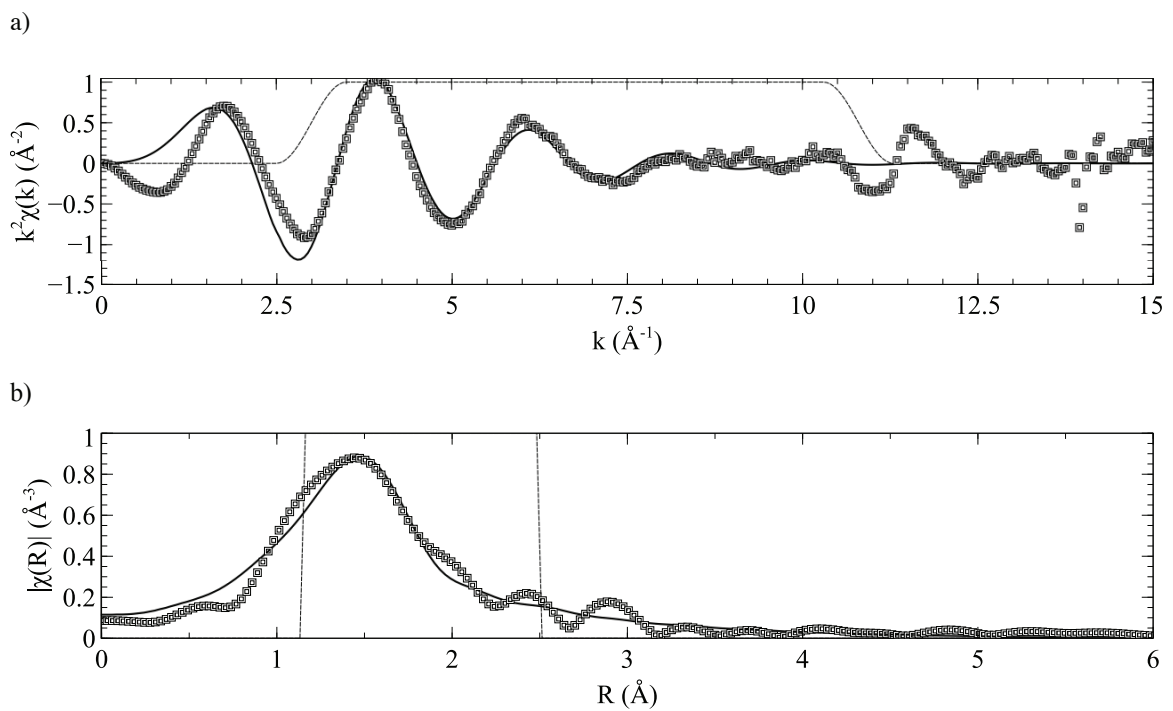
Fig. 4.1: EXAFS data $\chi(k)$ in reciprocal space (a) and $|\chi(R)|$ in real space (b), for sample ZT15. Squares: data; solid line: fit; dashed line: Hanning window function (a), fitting range (b).
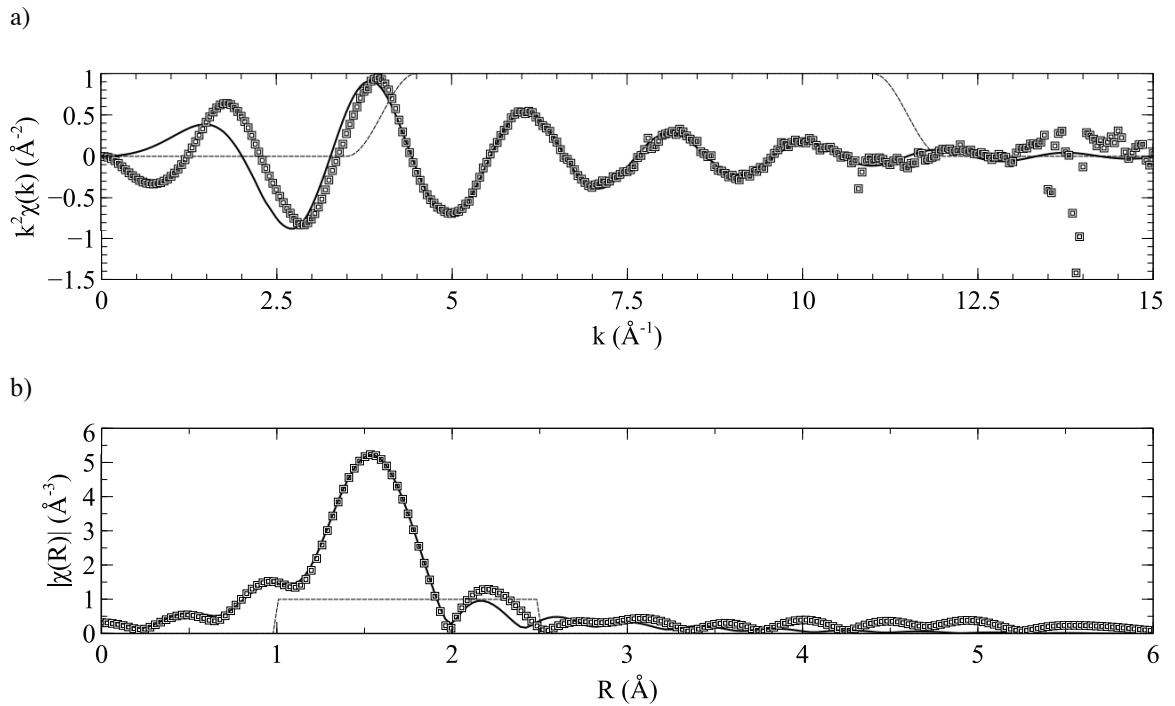
a)

b)
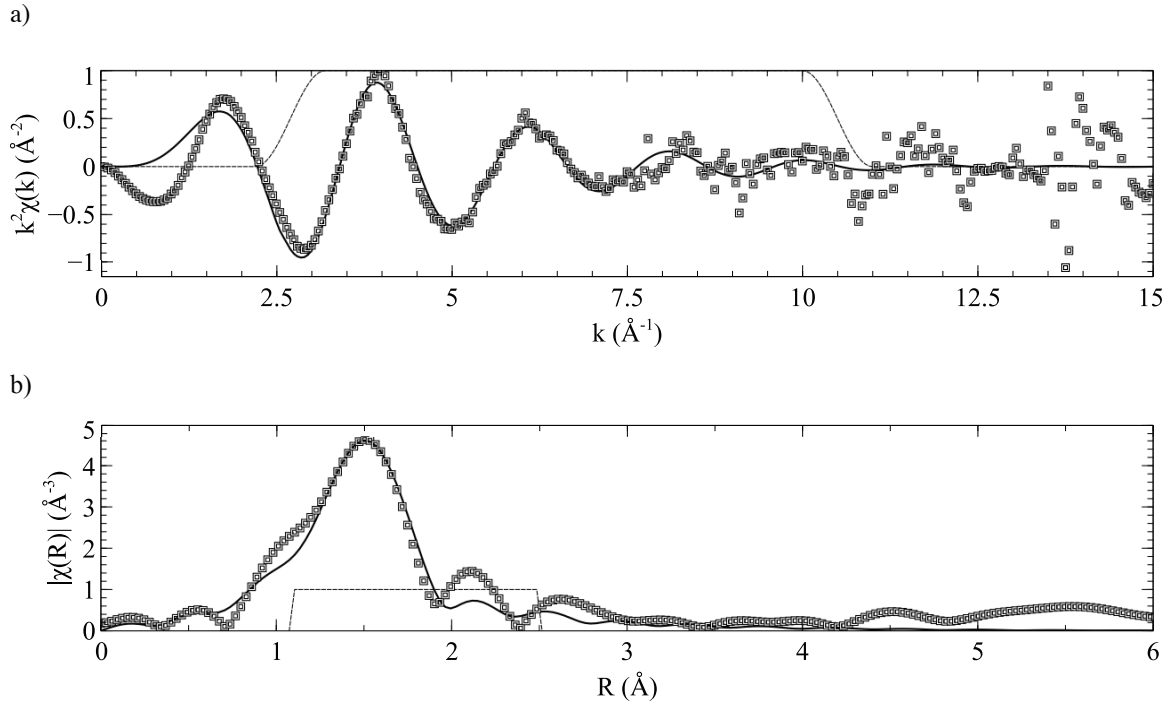
Fig. 4.2: EXAFS data $\chi(k)$ in reciprocal space (a) and $|\chi(R)|$ in real space (b), for sample ZT20. Squares: data; solid line: fit; dashed line: Hanning window function (a), fitting range (b).

a)

b)
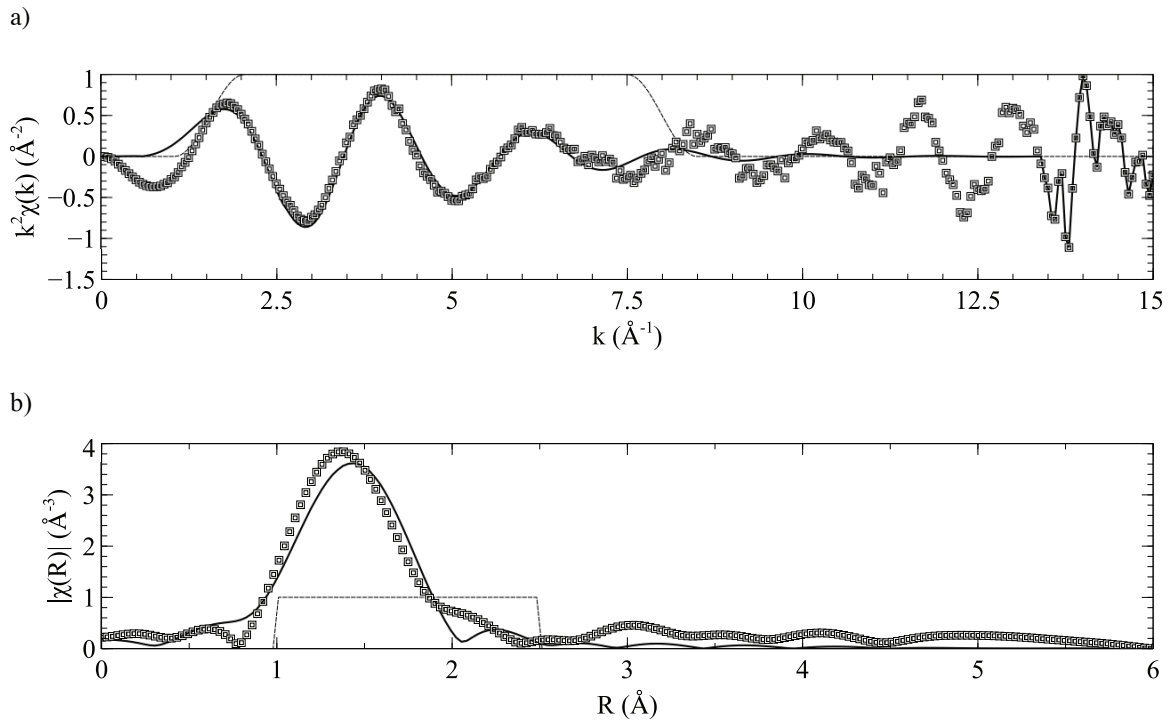
Fig. 4.3: EXAFS data $\chi(k)$ in reciprocal space (a) and $|\chi(R)|$ in real space (b), for sample ZT30. Squares: data; solid line: fit; dashed line: Hanning window function (a), fitting range (b).

a)

b)
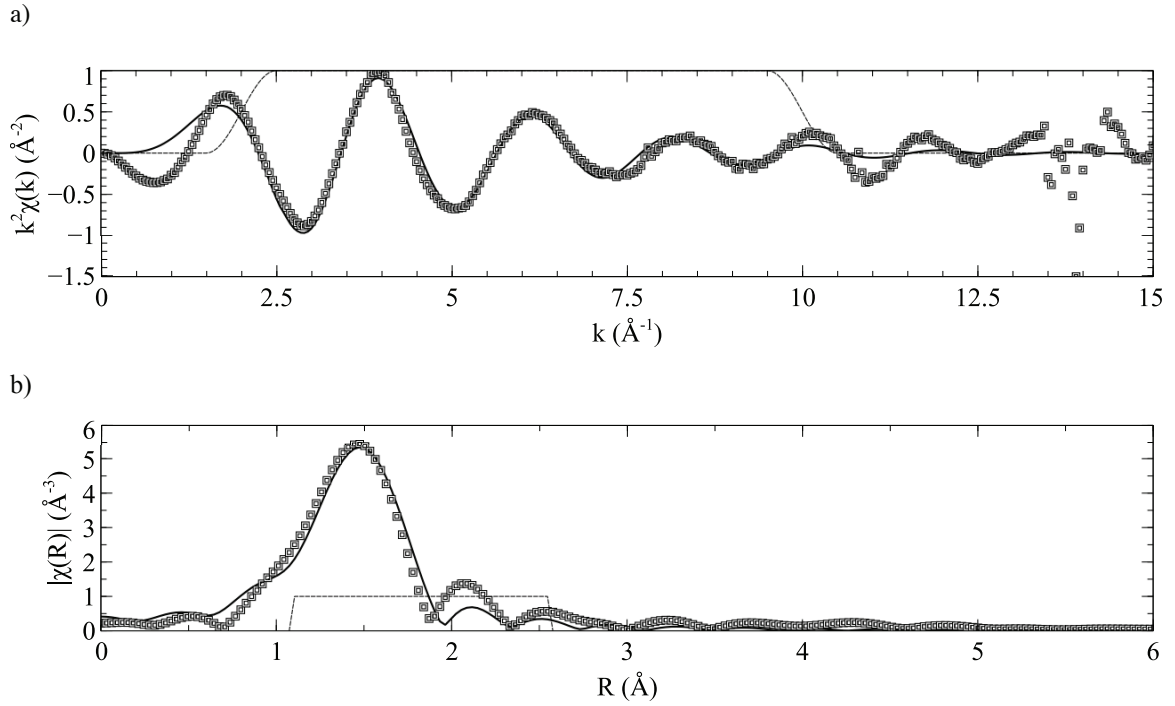
Fig. 4.4: EXAFS data χ(*k*) in reciprocal space (a) and |χ(R)| in real space (b), for sample ZT35. Squares: data; solid line: fit; dashed line: Hanning window function (a), fitting range (b).

a)

b)

Fig. 4.5: EXAFS data χ(*k*) in reciprocal space (a) and |χ(R)| in real space (b), for sample ZT40. Squares: data; solid line: fit; dashed line: Hanning window function (a), fitting range (b).

Using a first coordination shell based on the crystalline structure of ZnO, bond lengths (d), coordination numbers (N), variances in absorber-scatterer distance (σ^2) and energy shifts (ΔE_0) were fit for each sample:

Table 4.2: Bond lengths, coordination numbers, variance in absorber-scatterer distance and edge shift determined by EXAFS fitting for $ZnO_{(x)}$-$TeO_{2(1-x)}$ glasses

x	d (Å)	N	σ^2 (Å^2)	ΔE_0 (eV)
.15	1.974 ± .022	6.23 ± 1.64	.015 ± .004	-1.35 ± 2.40
.20	1.981 ± .017	4.28 ± .80	.011 ± .003	0.43 ± 1.72
.30	1.976 ± .024	4.10 ± .95	.015 ± .005	1.23 ± 1.68
.35	1.939 ± .013	4.10 ± .69	.009 ± .002	0.24 ± 1.09
.40	1.965 ± .009	3.87 ± .60	.006 ± .001	-3.52 ± 1.66

4.1.3 Raman Spectroscopy

Raman spectra of zinc tellurite glasses are shown below. The spectra below were measured using a Nicolet NCR9650 Raman Spectrometer with a 1064nm NIR laser and a power of 0.3W. 450 scans for each sample were performed at a resolution of 4cm^{-1}.
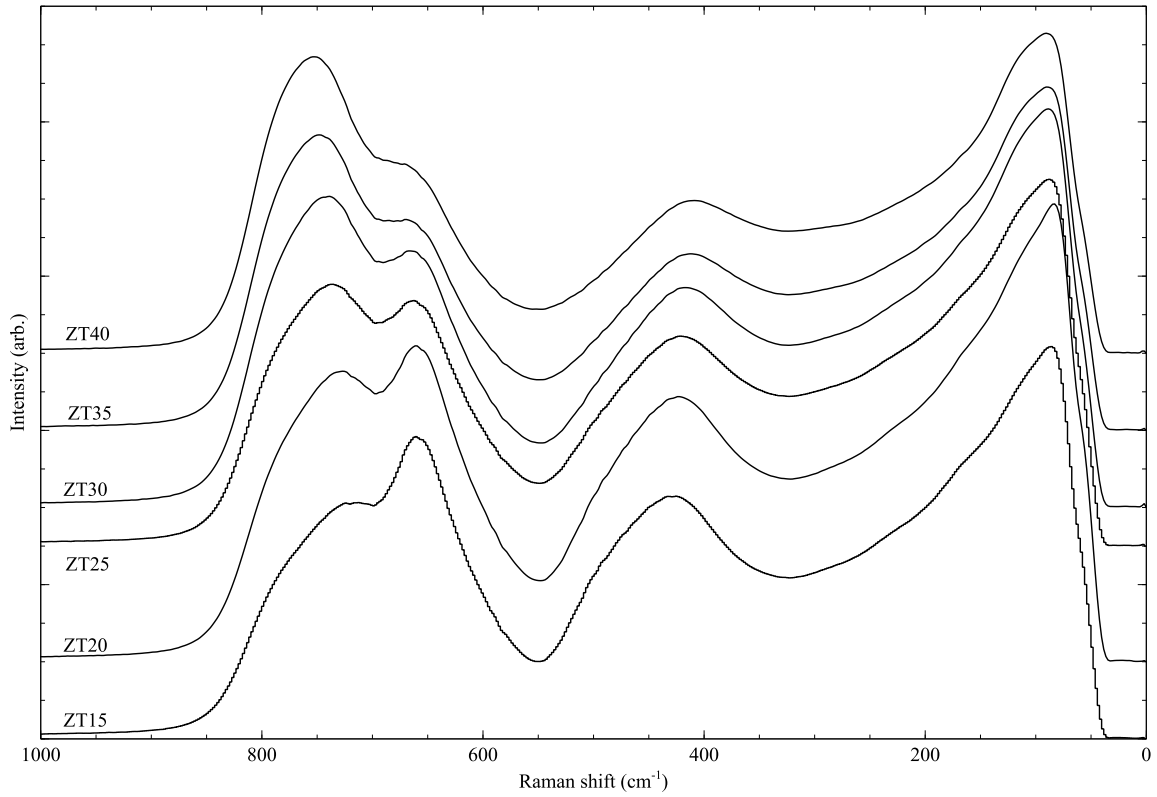
Fig. 4.6: Raman spectra of $ZnO_{(x)}$-$TeO_{2(1-x)}$ glasses where x = 0.15 to 0.40

4.1.4 Stress-Optic Coefficient

Stress-optic coefficients of polished glass samples were measured by the Sénarmont compensator method described in section 3.3, using both the benchtop polarimeter and the 594nm laser. The fractional birefringence $\Delta n/n_1$ as a function of stress is plotted below for each method.
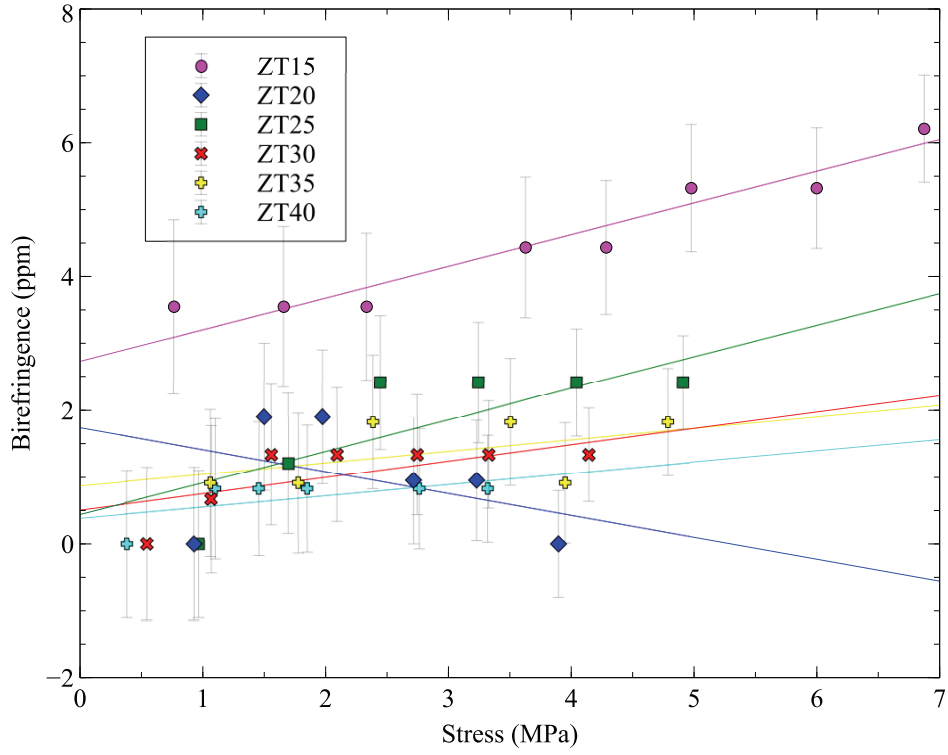
Fig. 4.7: Birefringence in $ZnO_{(x)}$-$TeO_{2(1-x)}$ glasses where x = 0.15 to 0.40 measured using polarimeter
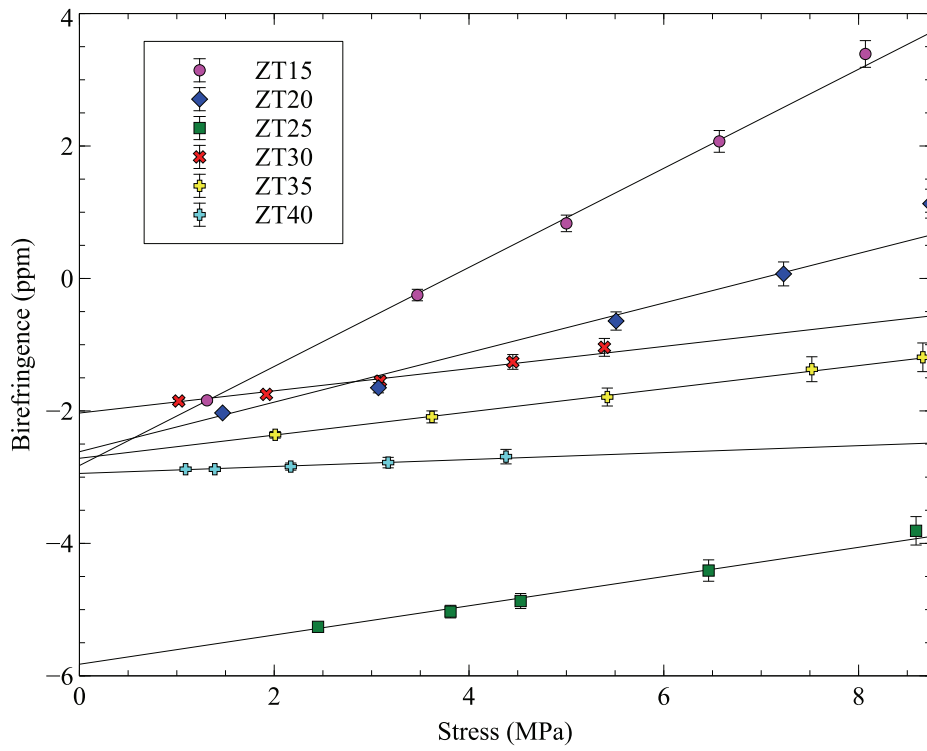
Fig. 4.8: Birefringence in $ZnO_{(x)}$-$TeO_{2(1-x)}$ glasses where x = 0.15 to 0.40 measured using 594 nm laser

The stress-optic coefficient C for each glass is found by taking the slope of the birefringence vs. stress graph, and has units of TPa^{-1}, or Brewsters. For the polarimeter measurements, uncertainties are introduced during the manual determination of extinction angle. For the laser measurements, uncertainties are given as the standard deviation from 5 trials for each sample. The non-zero y-intercept in the laser measurements is due to a known offset off approximately 2° in the rotating analyzer. As the laser measurements provided considerably greater precision, they are taken as the definitive result in the following discussion. A laser measurement was not possible for the sample ZT30 as the glass cracked during measurement, therefore the polarimeter value is used.

Table 4.3: Stress-optic coefficients of $ZnO_{(x)}$-$TeO_{2(1-x)}$ glasses

x	$C_{polarimeter}$ (Brewsters)	C_{laser} (Brewsters)
.15	0.45 ± .08	0.758 ± .012
.20	-0.21 ± .05	0.422 ± .024
.25	0.56 ± .05	0.189 ± .019
.30	0.31 ± .07	
.35	0.18 ± .05	0.178 ± .003
.40	0.20 ± .07	0.057 ± .003

4.1.5 Refractive Index

The refractive indices of zinc tellurite glasses, measured by spectroscopic ellipsometry, are shown below:

Table 4.4: Refractive indices of $ZnO_{(x)}$-$TeO_{2(1-x)}$ glasses

x	Refractive Index
.15	$2.061 \pm .010$
.20	$2.098 \pm .004$
.25	$2.044 \pm .010$
.30	$2.027 \pm .004$
.35	$2.017 \pm .004$
.40	$1.992 \pm .004$

4.1.6 Discussion

For binary glass compositions, density measurements allow for an easy approximation of glass composition by comparison with literature results for the same glass series. The density measurements of the zinc tellurite glasses agree very well with literature values so it can be assumed that the true compositions of these glasses deviate very little from their nominal compositions.

The structure of zinc tellurite glass was studied using EXAFS and Raman Spectroscopy: EXAFS to determine the Zn coordination environment by extracting bond lengths and coordination numbers from spectra taken at the Zn K-edge, and Raman to estimate the relative amounts of the various structural units containing Te by examining peak intensities in the Raman spectra. Previous models [26, 52, 57] agree that the TeO_2 glass network is disrupted with the addition of a modifier such as ZnO, as Te-O-Te bridges are broken by an oxygen atom from the modifying oxide. In this process, TeO_4 trigonal bipyramid units with one non-bridging oxygen (NBO) become TeO_3 trigonal pyramid units with two NBOs. The present measurements support this type of modification of the glass network as the fraction of ZnO is increased.

The Zn K-edge EXAFS results for the zinc tellurite glass series indicate that the Zn coordination number decreases from near 6 to near 4 and the Zn-O bond lengths remain essentially constant in the range 1.94 – 1.98 Å when the fraction of ZnO is

increased in the glass composition. Observation of the EXAFS spectra shows slightly higher amplitude of $\chi(k)$ for low ZnO compositions, in agreement with the reported values of coordination number, since coordination number determines amplitude in the EXAFS equation. For low-zinc compositions, the 6-fold coordination of zinc agrees with x-ray and neutron diffraction measurements by Kozhukarov *et al*. [52], where it was shown that paratellurite (α-TeO$_2$) chains are connected by ZnO$_6$ (also referred to as ZnO$_{4+1+1}$) polyhedra:
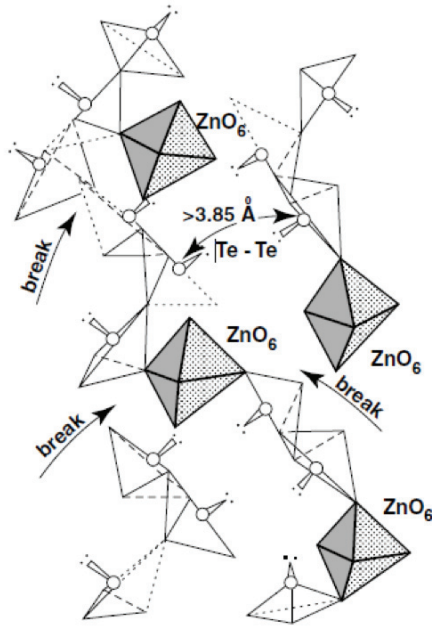
Fig. 4.9: A proposed model for the structure of ZnO$_{(20\%)}$-TeO$_{2(80\%)}$ glass based on diffraction measurements [52]

It has been shown that ZnO is capable of taking on both a network modifying and network-forming role in zinc tellurite glass, depending on composition. [51, 58, 59]. Rather than the octahedral ZnO$_6$ configuration seen above, ZnO is present in the form of ZnO$_4$ tetrahedra when acting as a network former. Therefore, the decrease in Zn coordination number as measured by EXAFS suggests that for low ZnO compositions, ZnO acts mostly as a network modifier, breaking Te-O-Te linkages, and at higher ZnO, a network of ZnO$_4$ tetrahedra is formed. The effect on the d/N_c parameter from the empirical model due to the change in the average Zn coordination environment is

obvious: as the percentage of ZnO in the glass increases from 15 to 40, the contribution to the average d/N_c ratio increases also, from ~.31 Å to ~.51 Å.

Raman spectra of the ZnO-TeO_2 glass system have been well documented [26, 50]. It has been established and agreed upon that peaks in Raman intensity near 400 cm^{-1} and 650 cm^{-1} are due to the vibrational modes of TeO_4 units in the glass, while peaks in the range of 720-780 cm^{-1} are due to TeO_3 and TeO_{3+1} units. While it is notoriously difficult to quantitatively interpret the Raman spectra of glasses, estimates can be made based on relative intensities of the various peaks. Himei *et al*. have suggested a method of determining the ratio TeO_3/TeO_4 by plotting the ratio of peak intensities corresponding to each type of unit vs. composition, then fitting a line and subtracting the y-intercept from each intensity ratio to estimate the TeO_3/TeO_4 ratio [26]. Such a method predicts that over the glass forming range of the ZnO-TeO_2 glass, the fraction of TeO_3 units increases from about .40 to about .65. Hoppe *et al*. have measured N_3 (the fraction of TeO_3 units) using neutron and x-ray diffraction and found that for a 22% ZnO glass, $0.39 < N_3 < 0.59$, while for a 30% ZnO glass, $0.62 < N_3 < 0.82$ [57]. Matsumoto *et al*. used neutron diffraction and molecular dynamics to develop models of the zinc tellurite glass structure and estimated that for 10, 20 and 30% ZnO, N_3 was relatively consistent at 0.85-0.90 [Matsumoto]. Kozhukarov *et al*. found that for a 21% ZnO glass, 35% of the Te atoms are 4-fold coordination and 65% have a lower coordination [52]. The results from the diffraction experiments and the structural models derived by molecular dynamics agree that Te-O bond lengths in the first coordination shell lie between 2.0 and 2.2 Å.

The Raman spectra in Fig. 4.6 show that the peak near 650 cm^{-1} decreases in intensity with added ZnO, indicating a decreasing presence of TeO_4 units in the glass. The peak near 720 cm^{-1} quickly increases in intensity as ZnO is added, indicating the formation of TeO_3 units. Such a trend is clearly in agreement with the aforementioned conversion of TeO_4 trigonal bipyramids to TeO_3 trigonal pyramids. The contribution to the d/N_c parameter for the TeO_2 component of the glass is therefore increasing with higher modifier content. Many of the previous estimates of the TeO_3 concentration over the glass forming range agree that N_3 can be below .40 for low amounts of modifier and increase to over 0.80 in highly modified glasses. Using a range of $0.35 < N_3 < 0.85$ and a uniform increase with the addition of modifier to the glass, d/N_c for Te would increase

from .56 to .64 Å. After combining these estimates with the ZnO result, the average d/N_c ratio for the two-component glass increases from .52 Å for the 15% ZnO glass to .59 Å for 40% ZnO. Full calculations including uncertainties are shown below in Table 5.1:

Table 4.5: The d/Nc parameter in $ZnO_{(x)}$-$TeO_{2(1-x)}$ glasses

x	Zn-O d/N_c (Å)	Te-O d/N_c (Å)	Average d/N_c (Å)
.15	.32 ± .07	.56 ± .01	.52 ± .02
.20	.47 ± .07	.58 ± .01	.55 ± .02
.30	.48 ± .09	.61 ± .01	.57 ± .03
.35	.47 ± .07	.63 ± .01	.57 ± .02
.40	.51 ± .07	.64 ± .01	.59 ± .03

      Measurements of the stress-optic coefficient for the zinc tellurite glasses indicate that the result is generally small and positive, decreasing with additional ZnO in the glass composition. As the coefficients are all less than 1, it is clear that the photoelastic effect in zinc tellurite glass is quite small regardless of the composition. To determine whether or not the photoelastic response of zinc tellurite glass is in agreement with the predictions of the empirical model, the relationship between the d/N_c parameter and the stress-optic coefficient, as shown in Fig. 5.2 below, must be examined.
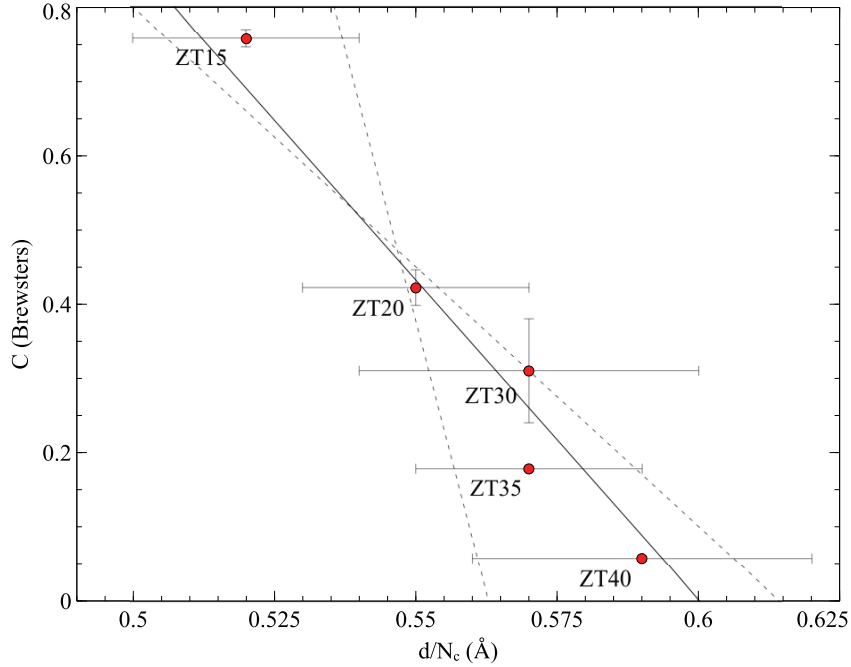
Fig. 4.10: The relationship between the d/N_c parameter and the stress-optic coefficient in $ZnO_{(x)}$-$TeO_{2(1-x)}$ glasses where x = 0.15 to 0.40

The empirical model predicts that the stress-optic coefficient of a glass will change signs from positive to negative as the average d/N_c ratio increases from below 0.50 Å to between 0.50 and 0.55 Å. The results for the zinc tellurite glass series seem to be in rough agreement with the model, but with a threshold closer to 0.60 Å. The trend across the range of compositions shows that a smaller d/N_c tends to yield a larger stress-optic coefficient. Additionally, the values of the stress-optic coefficient that reach near-zero are those for which d/N_c was near the 0.55-0.60 Å threshold. Although the EXAFS measurements have led to a relatively high degree of experimental uncertainty, the empirical model can be used to successfully make predictions about the evolution of the photoelastic response in zinc tellurite glass.

The zinc tellurite glass system is interesting to study in the context of the empirical model of photoelasticity, as both of its constituents possess a d/N_c ratio of 0.50 Å in their crystalline forms, right on the threshold between conferring a positive and negative stress-optic response. It has been found that zinc tellurite glasses carry a small, positive stress-optic coefficient, although a zero-stress optic zinc tellurite glass may be

possible at compositions containing over 40% ZnO, but such compositions are difficult to make into a glass under practical conditions. This work suggests that the photoelastic effect is minimized in zinc tellurite glass for compositions having a d/N_c ratio at or above 0.55 Å, thus giving a better understanding of the applicability of the empirical model to this type of glass. In addition to its other interesting optical properties such as high refractive index and third-order nonlinear susceptibility [26], a better understanding of its photoelastic response may lead to interesting new applications for zinc tellurite glass.

4.2 Zinc Borate Glass $ZnO_{(x)}$-$B_2O_{3(1-x)}$

The d/N_c ratios of crystalline ZnO and B_2O_3 are 0.50 Å and 0.46 Å, respectively [5]. The empirical model predicts that increasing the fraction of ZnO in the glass composition should decrease the stress-optic coefficient and this result has been previously reported [55]. The zinc borate system was studied as an extension of work done by Dr. Vincent Martin for his PhD [28]. Martin prepared zinc borate glass samples and carried out structural and photoelastic measurements. [11]B Nuclear Magnetic Resonance (NMR) spectroscopy was used to measure the coordination environment of B in the glasses and stress-optic coefficients were measured by the Sénarmont method. Zn EXAFS data were collected but not analyzed. Unfortunately, the data reported by Martin were not sufficient to test the empirical model. It is hoped that by analyzing the EXAFS data, a more accurate determination of the d/N_c ratio can be found and a meaningful conclusion can be reached regarding the applicability of the empirical model to the zinc borate glass system.

4.2.1 Density, Stress-Optic Coefficient and NMR

Martin measured the densities and stress-optic coefficients of his zinc borate glass series. Estimates of the actual compositions were inferred from the trend in the density measurements:

Table 4.6: Density, molar volume and stress-optic coefficients of $ZnO_{(x)}$-$B_2O_{3(1-x)}$ glasses

x	Actual Zn %	Density (g/cm^3)	Mol. Vol. (cm^3/mol)	C (Brewsters)
.30	51	3.409 ± .002	22.18 ± .01	1.0 ± .2
.40	58	3.574 ± .002	22.39 ± .01	3.4 ± .2
.50	61	3.629 ± .002	21.16 ± .01	4.1 ± .2
.60	63	3.663 ± .002	21.03 ± .01	5.4 ± .2

Molar Volumes were calculated for the purpose of this work by dividing the molar weight for $Zn_xB_{2-2x}O_{3-2x}$ by the density, using the actual compositions.

Martin also determined the fractions of BO_3 and BO_4^- units in the zinc borate glasses by analyzing their NMR spectra:

Table 4.7: NMR results for borate structure in $ZnO_{(x)}$-$B_2O_{3(1-x)}$ glasses

x	[BO_3] Fraction (%)	[BO_4^-] Fraction (%)
.30	65.7	34.3
.40	68.0	32.0
.50	70.8	29.2
.60	72.4	27.6

4.2.2 EXAFS

The EXAFS spectra collected by Martin were analyzed according to the procedure in section 3.2.3 and Appendix A. Plots showing the fit to χ in real space and reciprocal space are shown below for each zinc borate sample:

a)

b)
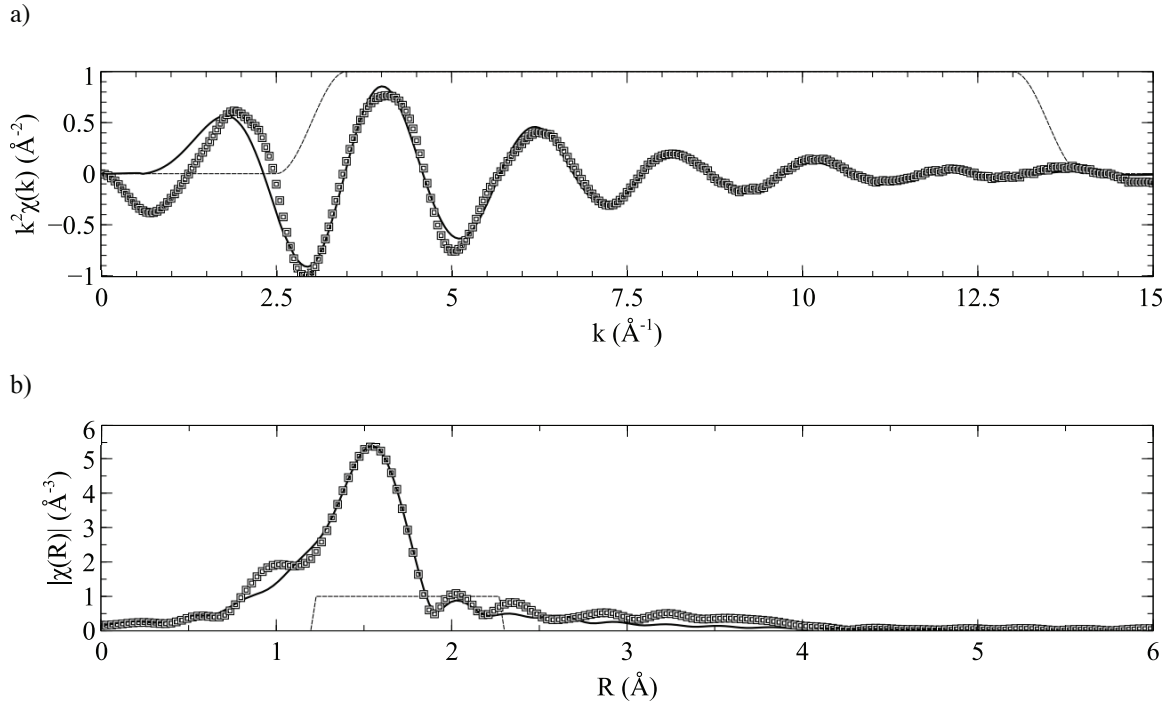
Fig. 4.11: EXAFS data χ(k) in reciprocal space (a) and |χ(R)| in real space (b), for sample ZB30. Squares: data; solid line: fit; dashed line: Hanning window function (a), fitting range (b).
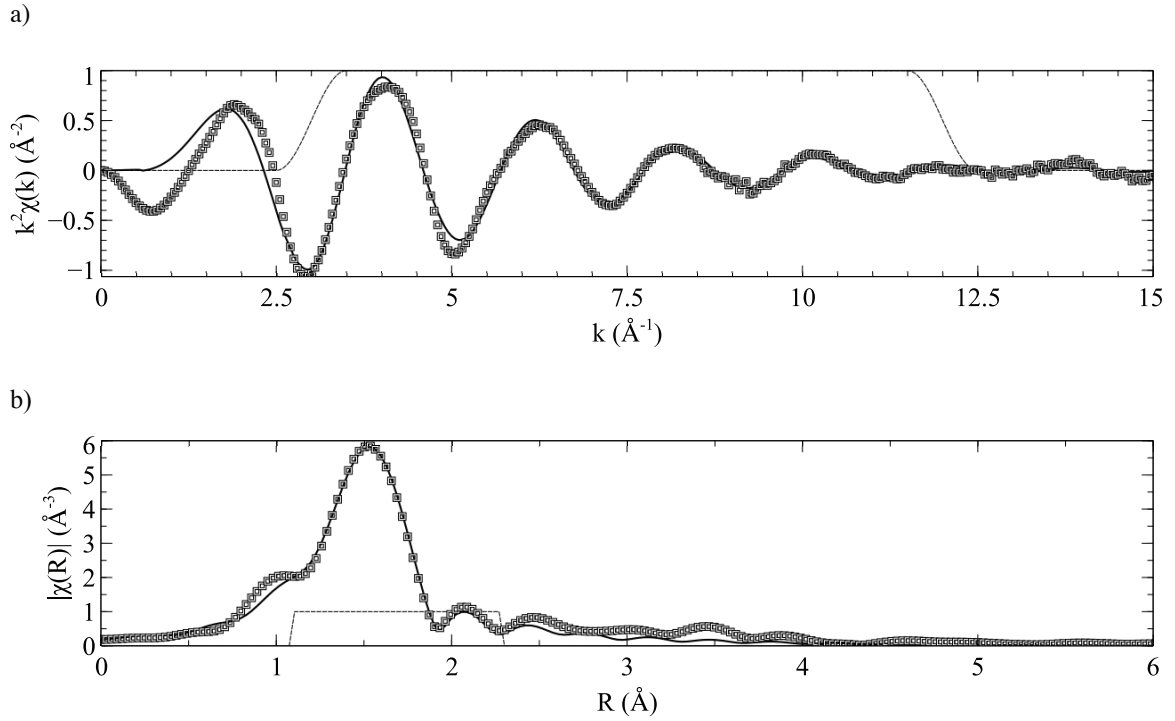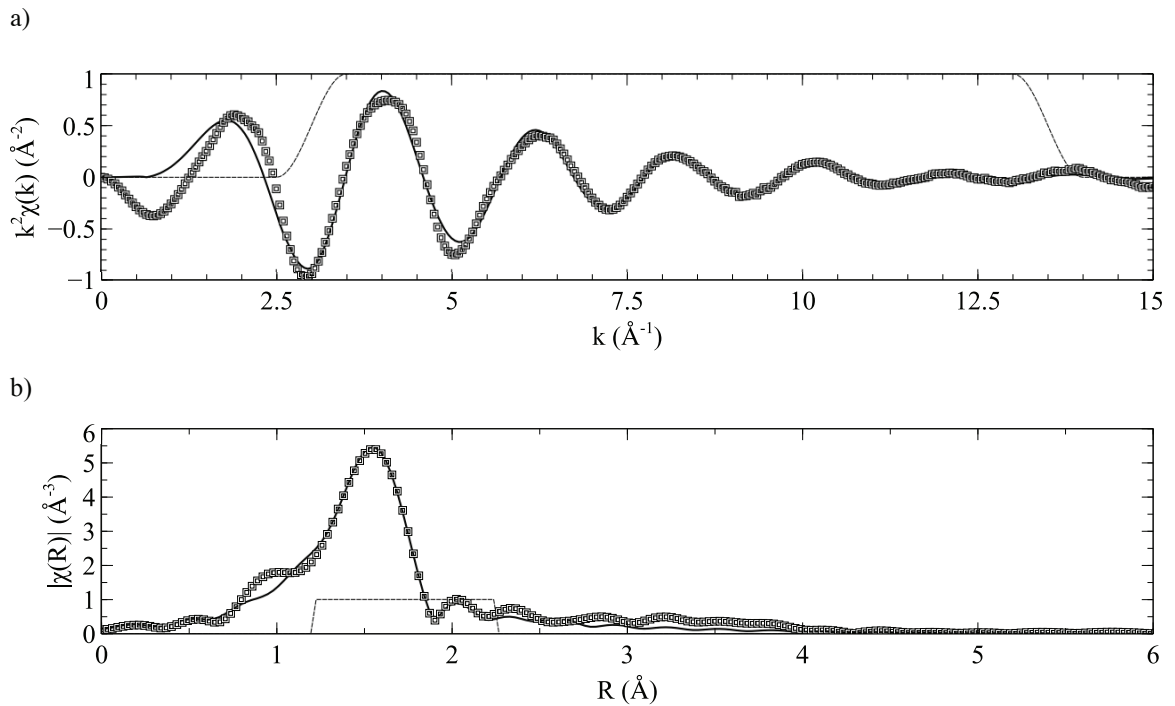
a)
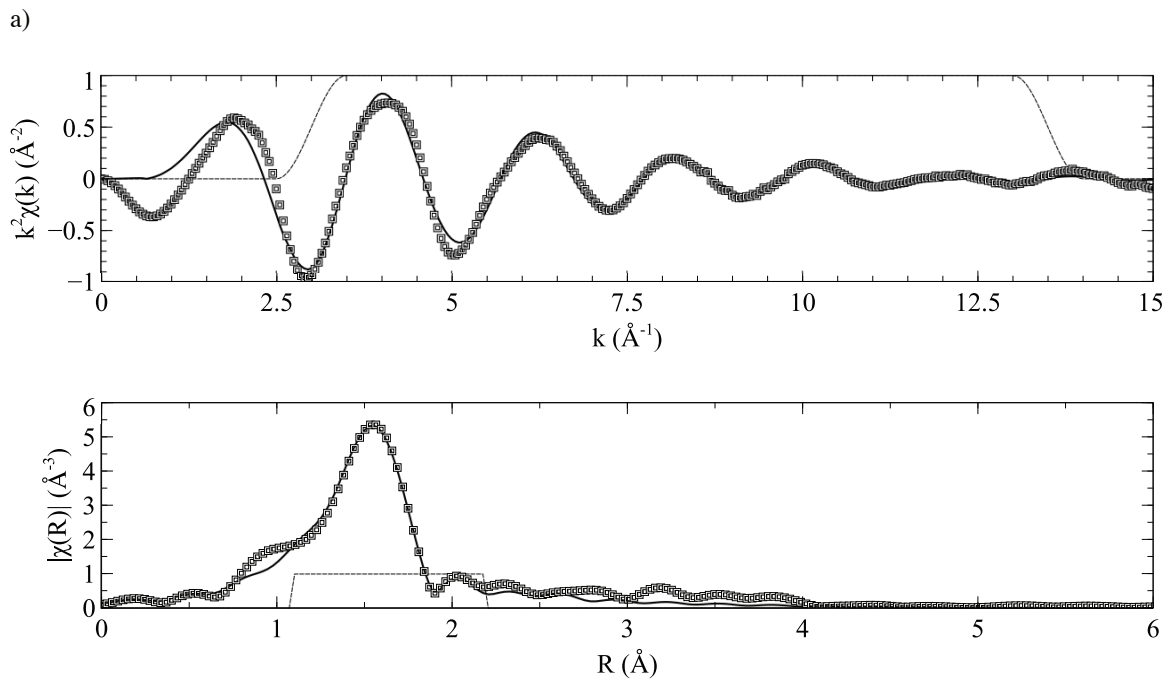
Fig. 4.12: EXAFS data χ(k) in reciprocal space (a) and |χ(R)| in real space (b), for sample ZB40. Squares: data; solid line: fit; dashed line: Hanning window function (a), fitting range (b).

a)

b)

Fig. 4.13: EXAFS data χ(*k*) in reciprocal space (a) and |χ(R)| in real space (b), for sample ZB50. Squares: data; solid line: fit; dashed line: Hanning window function (a), fitting range (b).

a)

b)

Fig. 4.14: EXAFS data χ(*k*) in reciprocal space (a) and |χ(R)| in real space (b), for sample ZB60. Squares: data; solid line: fit; dashed line: Hanning window function (a), fitting range (b).

Using a first coordination shell based on the crystalline structure of ZnO, bond lengths (d), coordination numbers (N), variances in absorber-scatterer distance (σ^2) and energy shifts (ΔE_0) were fit for each sample:

Table 4.8: Bond lengths, coordination numbers, variance in absorber-scatterer distance and edge shift determined by EXAFS fitting for $ZnO_{(x)}$-$B_2O_{3(1-x)}$ glasses

x	d (Å)	N	σ^2 (Å^2)	ΔE_0 (eV)
.30	1.961 ± .003	3.55 ± .46	.0073 ± .0004	1.26 ± .38
.40	1.960 ± .003	3.36 ± .43	.0069 ± .0004	1.41 ± .36
.50	1.959 ± .004	3.83 ± .55	.0070 ± .0005	1.25 ± .44
.60	1.960 ± .002	3.38 ± .45	.0067 ± .0003	1.40 ± .29

4.2.3 Refractive Index

Refractive indices of zinc borate glasses, measured by Abbe refractometry at 589 nm and using contact fluid with n = 1.80, are shown below:

Table 4.9: Refractive indices of $ZnO_{(x)}$-$B_2O_{3(1-x)}$ glasses

x	Refractive Index
.30	1.775 ± .004
.40	1.786 ± .004
.50	1.802 ± .001
.60	1.808 ± .003

4.2.4 Discussion

By adding Zn EXAFS analysis to the ^{11}B NMR measurements provided by Martin, a more complete picture of the local structure in zinc borate glass can be determined and correlated with the photoelastic response. Computing the average d/N_c ratio for zinc

borate glass should make it more clear whether or not the empirical model of photoelasticity can reliably be applied to this glass system.

The NMR results indicate that the addition of ZnO increases the fraction of trigonal BO_3 units and decreases the fraction of tetrahedral BO_4^- units. The decrease in average coordination agrees with previously published results where it has been suggested that BO_3 units with one or more non-bridging oxygen atoms begin to form as the modifier participates more heavily in the glass network [60, 61]. As the addition of ZnO to the glass composition lowers the average B-O coordination number, the borate contribution to the d/N_c ratio increases as the molar fraction of ZnO increases. Kajinami *et al*. indicate that the B-O bond length is 1.35 Å in the BO_3 unit and 1.45 Å in the BO_4^- unit [60]. The small decrease in d, however, is outweighed by the decrease in N_c so that the net change in d/N_c is still an increase.

EXAFS results indicate that the average Zn coordination number is approximately constant between 3 and 4, within uncertainty, over the range of compositions. Bond lengths are also constant at 1.96 Å. Using these results, the d/N_c ratio for zinc borate glass is calculated in Table 5.2 below.

Table 4.10: The d/Nc parameter in $ZnO_{(x)}$-$B_2O_{3(1-x)}$ glasses

x (Actual Zn %)	Zn-O d/N_c (Å)	B-O d/N_c (Å)	Average d/N_c (Å)
.30 (51)	.55 ± .06	.42 ± .01	.49 ± .03
.40 (58)	.58 ± .07	.42 ± .01	.52 ± .04
.50 (61)	.51 ± .06	.42 ± .01	.48 ± .04
.60 (63)	.58 ± .07	.43 ± .01	.52 ± .04

Unfortunately, the d/N_c parameters for the four glass samples are indistinguishable within uncertainty. While it may be impossible to make any claims about the evolution of d/N_c as the fraction of ZnO increases in the glass, the d/N_c value for the four glasses lies right on the 0.5 Å threshold used by the empirical model so the stress-optic response of these glasses may still provide useful insight. Fig. 5.3 shows the relationship between the stress-optic coefficient and the d/N_c parameter for the zinc borate glasses studied:
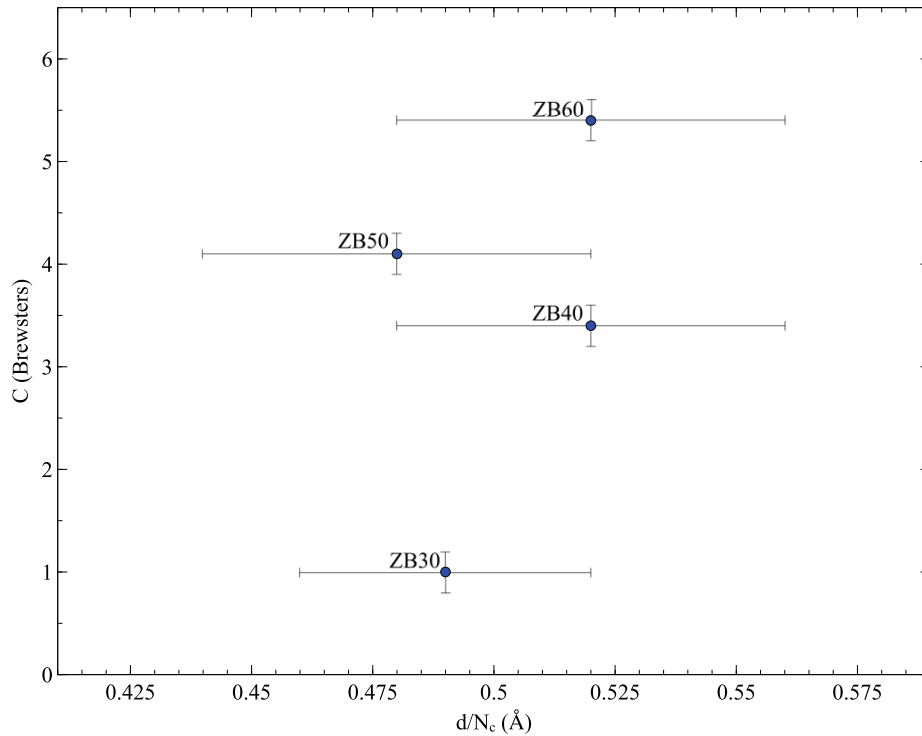
Fig. 4.15: The relationship between the d/N_c parameter and the stress-optic coefficient in $ZnO_{(x)}$-$B_2O_{3(1-x)}$ glasses where x = .51 to 63

Evidently, the stress-optic coefficient increases with increasing ZnO content, but not in a manner that can be described in terms of the d/N_c parameter. It was hoped that Zn EXAFS measurements would allow for a definitive conclusion to be made about how to apply the empirical model to zinc borate glasses. However, the limited precision with which coordination numbers can be determined through EXAFS analysis, even using high-quality data, meant that no such conclusion could be made. While it seems that zinc borate glass may reach a near-zero stress-optic response in the range near $d/N_c = 0.5$ Å, presently available data indicate that these glasses disagree with the predictions of the empirical model of photoelasticity.

4.3 Zinc Phosphate Glass $ZnO_{(x)}$-$P_2O_{5(1-x)}$

The d/N_c ratios for crystalline ZnO and P_2O_5 are 0.50 Å and 0.46 Å, respectively [5]. Previous studies indicate that these values are quite similar to those found in zinc phosphate glass [31, 56]. Therefore, the empirical model predicts that the addition of ZnO should decrease the stress-optic coefficient. As in the case of the zinc borate glass, Martin measured the stress-optic response of zinc phosphate glass but was unable to explain the results in terms of the empirical model [28]. It was concluded that additional investigation of the Zn coordination environment in these glasses might yield new insight into the relationship between local structure and photoelasticity and help us to better understand the predictive power of the empirical model. A series of ZnO-P_2O_5 glasses were prepared and Zn EXAFS was used to determine the Zn coordination environment.

4.3.1 Density

As for the zinc tellurite samples, densities of the zinc phosphate glasses were measured with the Mettler-Toledo Density Measurement Kit using the Archimedes method. Benzene, which has a density of .877g/ml at 20°C, was used as the immersion fluid. Therefore, densities were calculated as

$$\rho_{glass} = .877 \left[\frac{Weight\ of\ glass\ in\ air}{Buoyancy\ of\ glass\ in\ benzene} \right] \frac{g}{cm^3}. \tag{4.2}$$

The molar volume of each glass was found by dividing the molar weight for $Zn_xP_{2-2x}O_{5-4x}$ by the calculated density. Density values from the literature [31], for actual compositions measured by photometric, spectrochemical and microprobe analysis, are shown for comparison where available.

Table 4.11: Density and molar volume of $ZnO_{(x)}$-$P_2O_{5(1-x)}$ glasses

x	Density (g/cm³)	Density [31]	Molar Volume (cm³/mol)
.45	2.81 ± .01		40.8 ± .1
.50*	2.62 ± .01	(50%) 2.841 ± .006	42.6 ± .1
.55*	3.02 ± .02	(53.7%) 2.971 ± .006	36.0 ± .2
.60	3.27 ± .01	(60.4%) 3.273 ± .007	32.3 ± .1
.63	3.32 ± .01	(63.9%) 3.442 ± .007	31.3 ± .1
.645	3.37 ± .01		30.6 ± .1

*Significant bubbles present in glass

Measured density values fall in a similar range as the literature values, although are generally slightly lower. The discrepancy can be explained by the presence of bubbles artificially lowering the density in all zinc phosphate samples, and the nominal compositions are likely still a good representation of the true glass composition. ZP50, which lies outside the trend of increasing density and decreasing molar volume, was the sample most severely affected by bubbles.

4.3.2 EXAFS

EXAFS spectra of powdered zinc phosphate glasses were collected in transmission mode according to the procedure outlined in section 3.2.2 and analyzed as described in section 3.2.3 and Appendix A. Plots showing the fit to χ in real space and reciprocal space are shown below for each zinc phosphate sample, with the exception of ZP645 where a reasonable quality fit could not be obtained. The samples ZP55, ZP60 and ZP63 were fit using smaller than ideal k-ranges, which preferably would extend beyond k = 10 Å⁻¹, but were limited by the quality of the available data as uncertainties increased when the ranges were made larger. Nevertheless, the criterion of the number of parameters being less than 2/3 of the number of independent points was adhered to in every case.

a)

b)
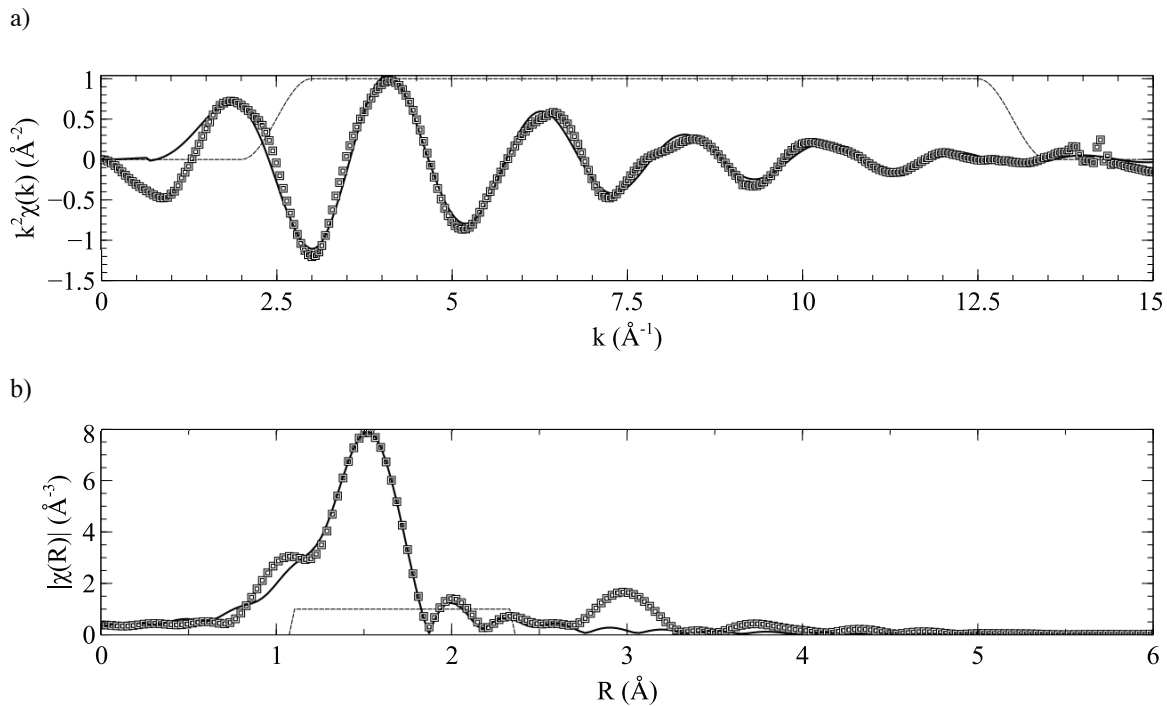
Fig. 4.16: EXAFS data χ(*k*) in reciprocal space (a) and |χ(R)| in real space (b), for sample ZP45. Squares: data; solid line: fit; dashed line: Hanning window function (a), fitting range (b).
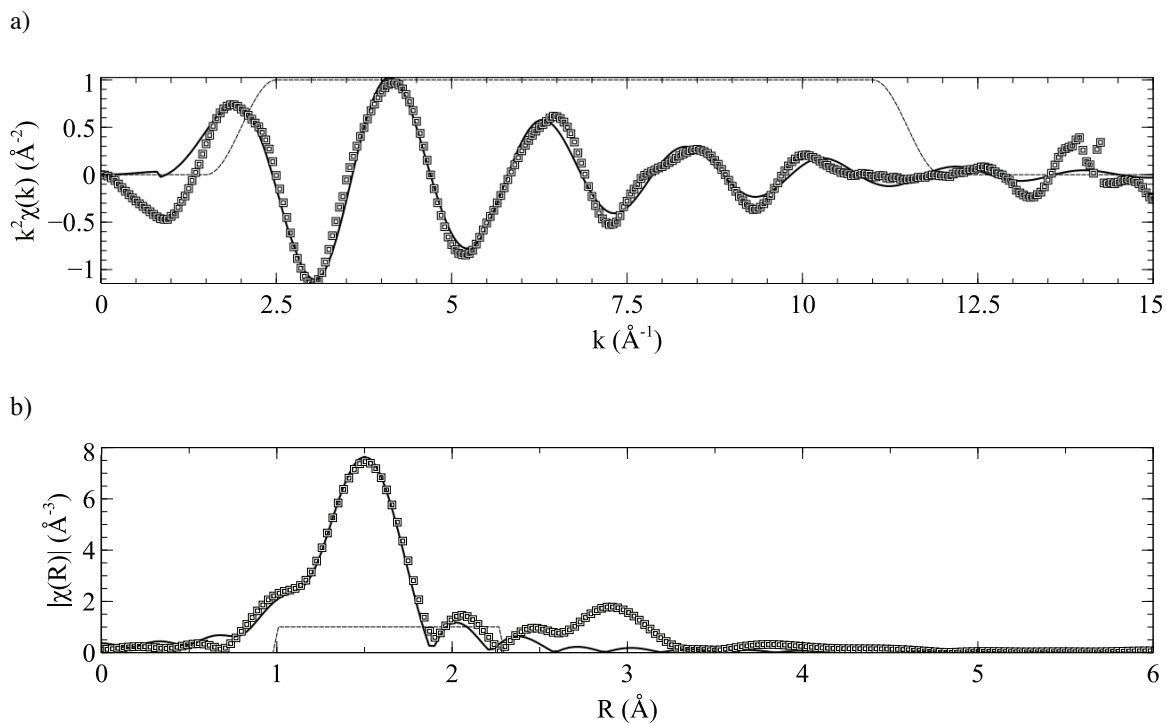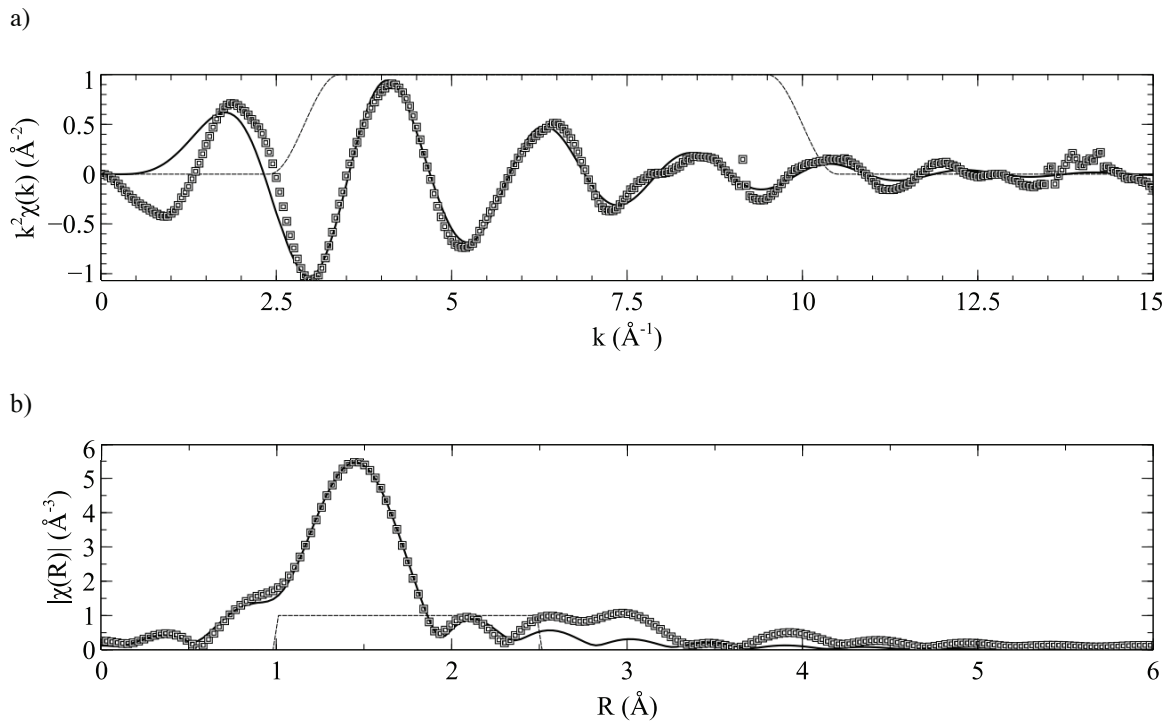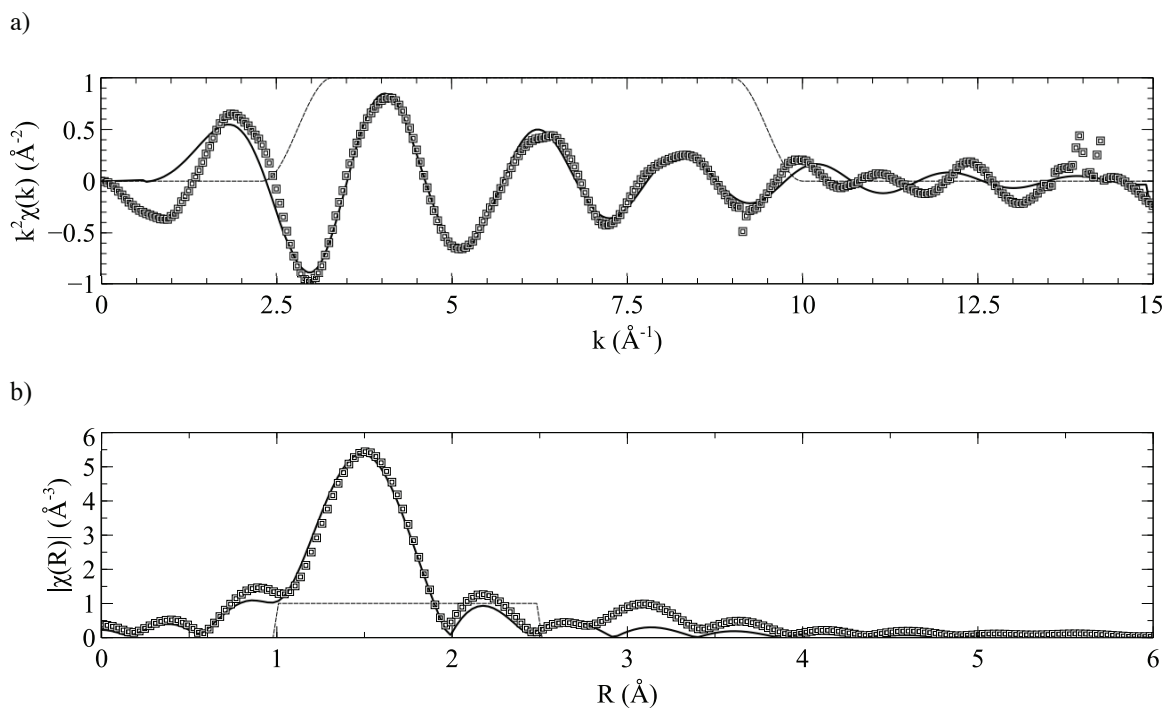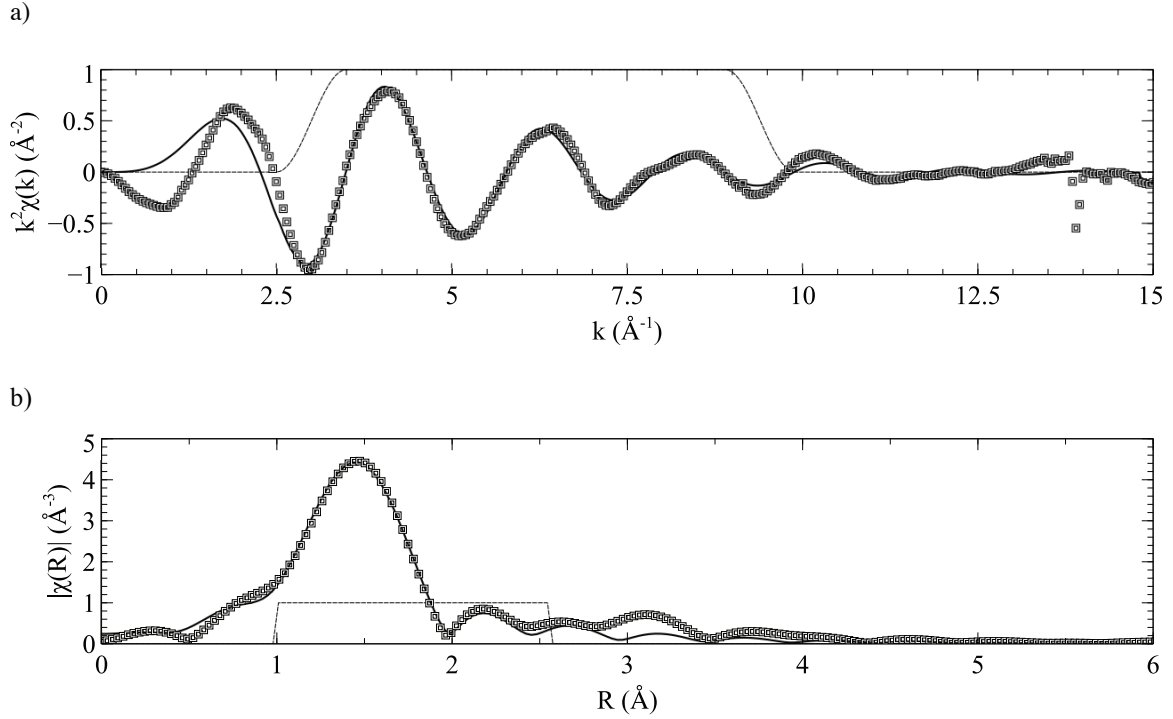
a)

b)

Fig. 4.17: EXAFS data χ(*k*) in reciprocal space (a) and |χ(R)| in real space (b), for sample ZP50. Squares: data; solid line: fit; dashed line: Hanning window function (a), fitting range (b).

a)

b)

Fig. 4.18: EXAFS data χ(*k*) in reciprocal space (a) and |χ(R)| in real space (b), for sample ZP55. Squares: data; solid line: fit; dashed line: Hanning window function (a), fitting range (b).

a)

b)

Fig. 4.19: EXAFS data χ(*k*) in reciprocal space (a) and |χ(R)| in real space (b), for sample ZP60. Squares: data; solid line: fit; dashed line: Hanning window function (a), fitting range (b).

a)

b)

Fig. 4.20: EXAFS data $\chi(k)$ in reciprocal space (a) and $|\chi(R)|$ in real space (b), for sample ZP63. Squares: data; solid line: fit; dashed line: Hanning window function (a), fitting range (b).

Using a first coordination shell based on a ZnO structure, bond lengths (d), coordination numbers (N), variances in absorber-scatterer distance (σ^2) and energy shifts (ΔE_0) were fit for each sample. As the 60% ZnO coordination appears to be significantly less than the others, the reliability of the fit for ZP60 was carefully checked to ensure stability. Small changes in the fitting ranges and initial guess parameters did not affect the outcome:

Table 4.12: Bond lengths, coordination numbers, variance in absorber-scatterer distance and edge shift determined by EXAFS fitting for $ZnO_{(x)}$-$P_2O_{5(1-x)}$ glasses

x	d (Å)	N	σ^2 (Å^2)	ΔE_0 (eV)
.45	1.940 ± .004	3.88 ± .35	.0052 ± .0005	1.80 ± .48
.50	1.940 ± .006	3.80 ± .41	.0054 ± .0009	2.74 ± .59
.55	1.920 ± .004	4.00 ± .35	.0078 ± .0007	-0.51 ± .51
.60	1.951 ± .009	3.15 ± .42	.0048 ± .0014	1.60 ± 1.05
.63	1.928 ± .006	3.64 ± .39	.0082 ± .0009	-1.00 ± .70

4.3.3 Stress-Optic Coefficient

Stress-optic coefficients of polished glass samples were measured by the Sénarmont compensator method described in 3.3, using both the benchtop polarimeter and the 594nm laser. The fractional birefringence $\Delta n/n_1$ as a function of stress is plotted below for each method.
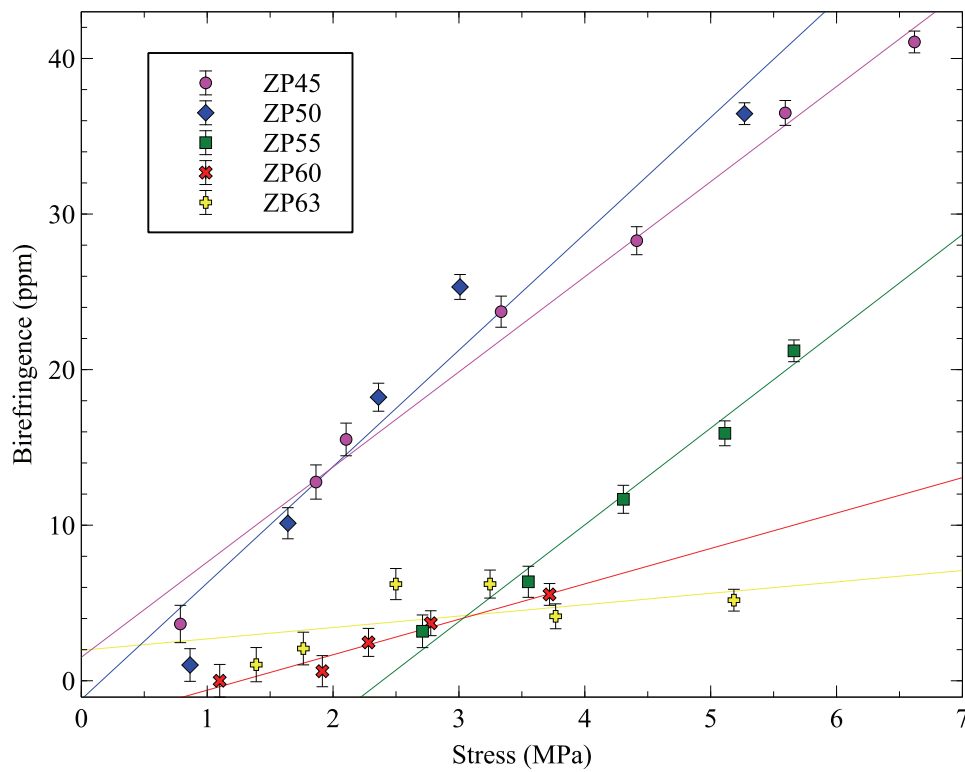

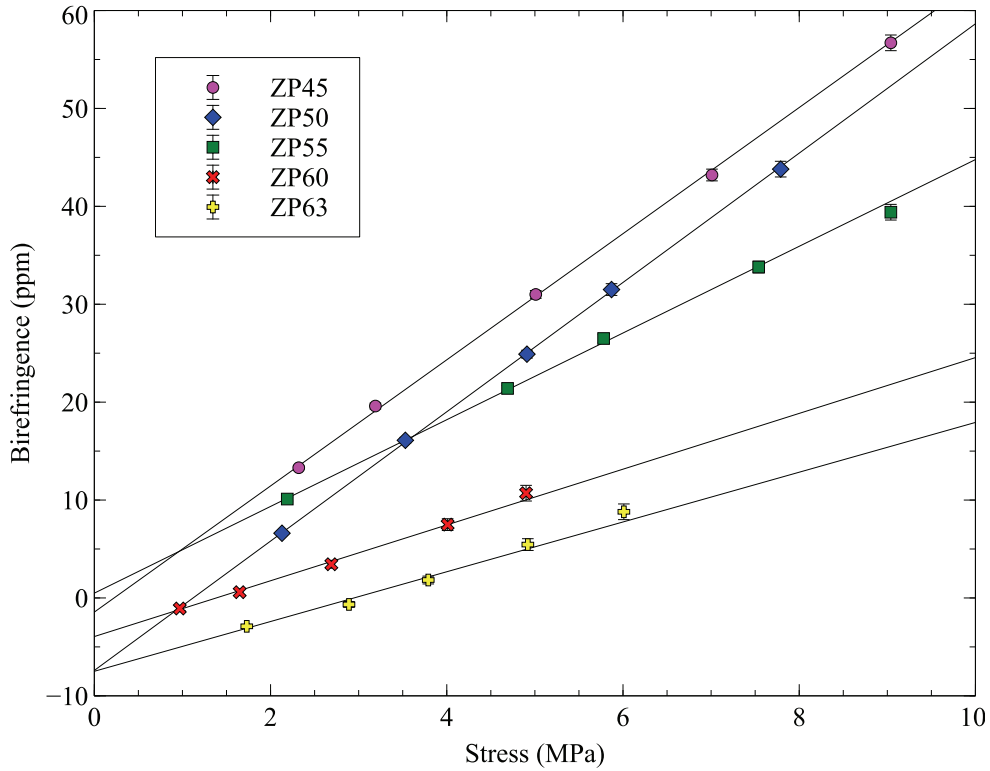Fig. 4.21: Birefringence in $ZnO_{(x)}$-$P_2O_{5(1-x)}$ glasses where x = 0.45 to 0.63 measured using polarimeter

Fig. 4.22: Birefringence in $ZnO_{(x)}$-$P_2O_{5(1-x)}$ glasses where x = 0.45 to 0.63 measured using 594 nm laser

The stress-optic coefficient C for each glass is found by taking the slope of the birefringence vs. stress graph, and has units of TPa^{-1}, or brewsters. For the polarimeter measurements, uncertainties are introduced during the manual determination of extinction angle. For the laser measurements, uncertainties are given as the standard deviation from 5 trials for each sample. As the laser measurements are generally more precise, they will taken as the definitive result in the following discussion.

Table 4.13: Stress-optic coefficients of $ZnO_{(x)}$-$P_2O_{5(1-x)}$ glasses

x	$C_{polarimeter}$ (Brewsters)	C_{laser} (Brewsters)
.45	6.3 ± .1	6.39 ± .09
.50	7.9 ± .2	6.60 ± .19
.55	6.1 ± .2	4.29 ± .12
.60	2.3 ± .2	2.98 ± .15
.63	1.0 ± .2	2.94 ± .48

4.3.4 Refractive Index

Refractive indices of zinc phosphate glasses, measured by Abbe refractometry at 589 nm and using contact fluid with n = 1.63, are shown below:

Table 4.14: Refractive indices of $ZnO_{(x)}$-$P_2O_{5(1-x)}$ glasses

x	Refractive Index
.45	$1.520 \pm .001$
.50	$1.526 \pm .001$
.55	$1.548 \pm .002$
.60	$1.578 \pm .001$
.63	$1.581 \pm .001$
.645	$1.596 \pm .001$

4.3.5 Discussion

The structure of zinc phosphate glass has been studied many times [31, 56, 62]. While the phosphate coordination environment is well understood, with bond lengths of 1.5 Å and coordination number 4, there is no consensus on the exact coordination of zinc in the glass. Walter *et al*. have found the Zn coordination number to be "about 4", while Suzuya *et al*. suggest that a combination of ZnO_4 and ZnO_5 polyhedra is present in the glass. Bond lengths have been reported between 1.9 and 2.1 Å. Using the Zn EXAFS results and stress-optic measurements, the relationship between local structure and photoelasticity will be examined to determine whether or not zinc phosphate glass supports the empirical model.

The EXAFS results in Table 4.10 show that the Zn coordination number is nearly constant at just below 4, with a slight minimum at the 60% ZnO composition. The EXAFS spectra agree with the coordination number minimum, as the amplitude of $\chi(k)$ is smallest for ZP60. Bond lengths all lie in the $1.92 - 1.95$ Å range. It appears that there

are no dramatic changes in the local structure surrounding zinc across the composition range. The monotonically increasing refractive index and decreasing molar volume (with the exception of the glasses heavily affected by bubbles), support this observation. Using the EXAFS results for zinc and the assumed tetrahedral PO_4 coordination, the d/N_c ratio for zinc phosphate glass is shown below in Table 5.3:

Table 4.15: The d/Nc parameter in $ZnO_{(x)}$-$P_2O_{5(1-x)}$ glasses

x	Zn-O d/N$_c$ (Å)	P-O d/N$_c$ (Å)	Average d/N$_c$ (Å)
.45	.50 ± .04	.375 ± .010	.43 ± .02
.50	.51 ± .05	.375 ± .010	.44 ± .02
.55	.48 ± .04	.375 ± .010	.43 ± .02
.60	.62 ± .07	.375 ± .010	.52 ± .04
.63	.53 ± .05	.375 ± .010	.47 ± .03

The average ratio appears to be quite constant for the three glasses with the lowest ZnO content. For the samples containing greater than 60% ZnO, however, d/N_c is somewhat higher due to the slightly decreasing Zn coordination number. This result aligns well with measurements of anomalous physical properties that have been documented in phosphate glasses containing approximately 50-60% modifier, referred to as the *phosphate glass anomaly* [62-64]. The anomalies have been attributed to the preference of non-bridging oxygen (NBO) atoms in the phosphate network for forming Zn-O-P bridges. As a small amount of modifier is added to the glass, the possibility for NBO to form these bridges is very high. As the fraction of modifier increases, all NBO are eventually able to form bridges. To continue bridge formation beyond this threshold, the coordination number of the modifier must be reduced, as seen in Table 4.10 where the 60% ZnO glass has the minimum coordination number. As additional modifier is added, no further bridges can be formed, so the average coordination number once again increases. The minimum in coordination number, accompanied by a corresponding minimum in the ionic volume fraction (or packing density), is believed to be the source of the phosphate glass anomaly [63].

The relationship between d/N_c and the stress-optic coefficient for zinc phosphate glass is seen below in Fig. 5.4:
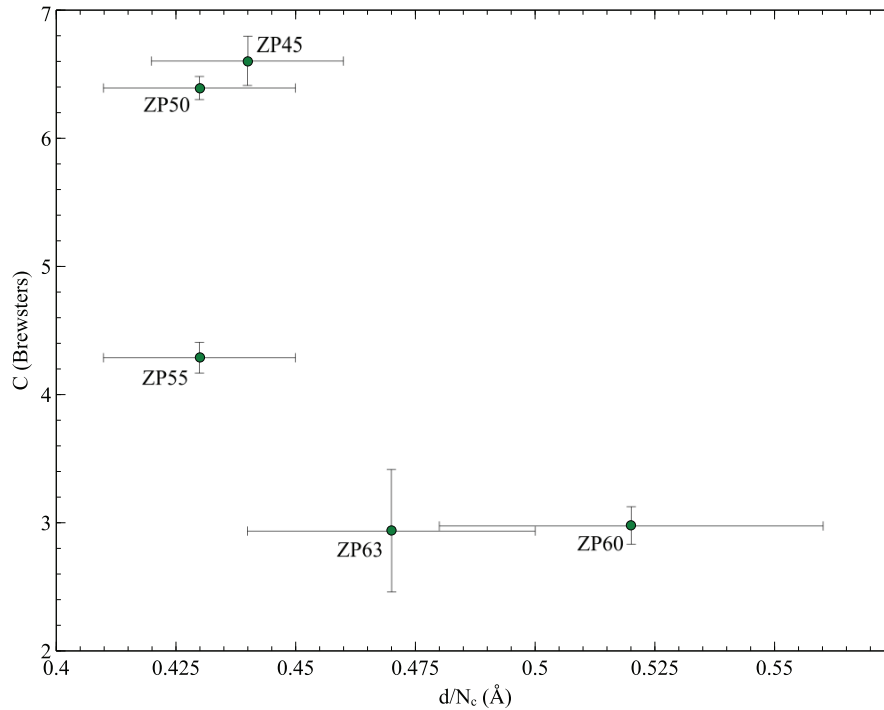

Fig. 4.23: The relationship between the d/N_c parameter and the stress-optic coefficient in $ZnO_{(x)}$-$P_2O_{5(1-x)}$ glasses where x = 0.45 to 0.63

It appears that the zinc phosphate glasses are separated into two distinct regimes: those with $d/N_c < 0.45$ Å, $C > 5.0$ B and ZnO < 60%; and those with $d/N_c > 0.45$ Å, $C < 5.0$ B and ZnO > 60%. In this sense, it would be possible to categorize the photoelastic response of zinc phosphate glasses according to their d/N_c ratio, in the spirit of the empirical model. The results do not, however, clearly suggest a zero stress-optic composition or a change from positive to negative stress-optic coefficient at $d/N_c = 0.5$ Å. It is likely that the phosphate glass anomaly affects the Zn coordination in the glass, but not its photoelastic response. Therefore, what would otherwise be a linear relationship with predictive power is obscured by the anomalous decrease in Zn coordination. For this reason, it may be difficult to ever reliably apply the empirical model of photoelasticity to phosphate glasses. If the anomalous composition range were ignored, it does appear that a trend may emerge, tending towards a zero stress-optic response near $d/N_c = 0.5$ Å, so

this may be the best strategy for identifying zero stress-optic phosphate glass compositions in the future.

Chapter 5

Conclusion

The goal of this thesis is to investigate the relationship between local structure and the photoelastic response in oxide glasses containing zinc and to test the predictions of the empirical model of photoelasticity developed by Zwanziger *et al*. The model predicts that ZnO as a glass modifier lies on the threshold between contributing to a positive and negative stress-optic response, and therefore could be useful in the development of lead-free zero stress-optic glass. The coordination environment of zinc and the photoelastic response must be measured for glasses to which ZnO has been added, to see if the predictions of the model hold true. The empirical model is a useful tool for researchers working to design new zero stress-optic glasses and this study helps to establish a better understanding of the model's applicability, strengths and weaknesses.

A significant obstacle in previous studies of zinc-modified glasses was that the zinc coordination environment is not easily determined using the methods that work well for many other chemical species, such as NMR or Mössbauer spectroscopy [34, 35]. Here, EXAFS spectroscopy provided greater insight regarding zinc's local structure when it is added to an oxide glass. The EXAFS results, combined with previous data, give a more complete structural picture that allows for more definitive statements to be made about the applicability of the empirical model. Measurements of the stress-optic coefficient provided good quality data showing clear trends and revealing possible zero stress-optic glass compositions. Structure and photoelastic properties were measured for zinc tellurite, zinc borate and zinc phosphate glasses. For each, results were compared with the empirical model's predictions and possible implications of the findings were discussed.

The zinc-containing glasses studied here each present a unique set of challenges in reaching an accurate determination of their local structure. From the data and results that were possible to obtain, an improved understanding of the correlation between structure and photoelasticity in these glasses has been developed. While it may not be possible to apply the empirical model of photoelasticity to all types of glass containing ZnO as a network modifier, this work provides a basis for whether or not one should attempt to do so. For zinc tellurite glass, it seems that the photoelastic response is relatively well correlated with structure, and the empirical model can be applied and could aid in the development of a zero stress-optic glass. Zinc borate glass provides greater challenges, and using all presently available data, no clear correlation between structure and photoelasticity emerges. The phosphate glass anomaly disrupts the pattern seen in the structure of zinc phosphate glasses, but if only the behaviour outside of the anomalous range is considered, then it may be possible to reliably apply the empirical model and predict a zero stress-optic zinc phosphate glass composition.

For zinc tellurite glass, it was found that ZnO shifts from a network-modifying to a network-forming behaviour as its molar fraction in the glass composition increases, accompanied by a corresponding decrease in coordination number from 6 to 4. The stress-optic coefficient decreases with added ZnO, to a near zero value at 40% ZnO. The stress-optic coefficient was well-correlated with the d/N_c parameter used by the empirical model. The primary conclusions from the study of zinc tellurite glass are that its photoelastic response can be predicted using the empirical model, and that its stress-optic coefficient can be very close to zero. While the model suggests that the zero stress-optic composition should be that for which $d/N_c \approx 0.5$ Å, it appears that for zinc tellurite glass, the lowest coefficients are found near 0.6 Å.

In zinc borate glass, the zinc coordination environment underwent no drastic changes as seen in the zinc tellurite case. As the fraction of ZnO is increased, tetrahedral BO_4^- units are converted into trigonal BO_3 units with non-bridging oxygen (NBO). The stress-optic coefficient increased with higher fractions of ZnO, contradicting Mueller's theory that suggests NBO serve to decrease the coefficient [10]. The d/N_c parameter for the various zinc borate glasses was indistinguishable within uncertainty; therefore the

empirical model is not able to predict the photoelastic response of zinc borate glass, according to current data.

Data from zinc phosphate glass indicate a trend that would suggest good agreement with the empirical model, with the exception of an apparent anomaly around the 60% ZnO composition. EXAFS data show an average zinc coordination slightly less than 4 and stress-optic coefficients decreased with added ZnO. The 60% ZnO glass was an exception where zinc coordination was significantly reduced, affecting the d/N_c parameter. Anomalies in this composition region have been previously observed and attributed to the varying ability of ZnO to form Zn-O-P bridges as the availability of NBO changes with composition. The anomaly, referred to as the phosphate glass anomaly, makes it difficult to successfully apply the empirical model to phosphate glass when considering all data points. However, the non-anomalous data display a trend that approaches a zero stress-optic composition near $d/N_c = 0.5$ Å, in good agreement with the model's predictions.

The above results confirm some previous theories, such as the ability of ZnO to act as both a network modifier and a network former. Further study into what determines this behaviour would prove valuable for predicting glass structure and photoelasticity. Other results have not been previously seen, such as the weak photoelastic properties of zinc tellurite glass. Two unanswered questions at the onset of the present work were whether or not ZnO could contribute to a zero stress-optic response, and whether or not the empirical model could be used to predict such a response. It has been shown that for certain glasses, both questions can be answered in the affirmative.

In the effort to design new lead-free zero stress-optic glass, this thesis contributes to a better understanding of the empirical model of photoelasticity and the materials to which it applies. Whereas it was previously not well known if zinc-modified glasses could have useful applications as zero stress-optic materials, the glasses studied herein provide a helpful starting point towards that end. Zinc tellurite glasses have promising photoelastic properties but an undesirable yellow colour. An additional glass modifier could potentially eliminate the colour, so the exploration of ternary zinc tellurite glass compositions could lead to a commercially applicable zero stress-optic glass.

For zinc borate and zinc phosphate glass, it was difficult to establish a clear correlation between the d/N_c parameter and the stress-optic response. The zinc borate structure varied slightly across the composition range, but any pattern was washed out by the large uncertainty inherent in the EXAFS measurement of coordination number. Until additional data or more precise measurement techniques become available, it will be difficult to apply the empirical model of photoelasticity to zinc borate glass. Zinc phosphate glass is slightly more promising than the zinc borate case, with one anomalous sample preventing a possible correlation that agrees with the model's predictions. If the measurements could be retaken using additional samples of zinc phosphate glass with 60% ZnO, it could be determined if the anomaly was a problem with the sample used. If the data could be interpreted in such a way as to work around or ignore the anomaly completely, then a helpful correlation could possibly be established for zinc phosphate glass.

The EXAFS data presented here leave considerable room for improvement. Additional scans and more careful attention to edge step size could result in higher quality data. Samples such as ZT15 with the smallest edge step had the largest uncertainties in their coordination number. Large uncertainties were also partially due to the small k-range from which usable data could be taken. Better data could enable a larger k-range (>10 Å) to be used, providing more certain results from which stronger conclusions could be drawn.

There is considerable potential for future work continuing in the spirit of this project. Most prominently, zinc borate glass should be more closely examined, as it is currently the best example that clearly disagrees with the empirical model's predictions. To understand the origin of such a disagreement would lead to a greater knowledge of the model's limitations. Zinc tellurite glass provides a promising basis for new optical applications and an investigation into how additional glass modifiers improve its properties may be a worthwhile endeavour. Further work on zinc phosphate glass should include exploration of the phosphate glass anomaly and finding methods to improve chemical durability. A more complete study of zinc-modified glasses could include the photoelastic response of materials not considered in this work, such as zinc silicate or zinc germanate glass.

The photoelastic response of oxide glass is a very interesting phenomenon and holds great promise as a continuing field of research with many facets yet to be fully explored. Knowledge about glass structure and photoelasticity is increasing considerably each year as glass scientists work towards the development of new materials with many technological applications.

This thesis has hopefully provided a small but significant contribution to the overall understanding of the relationship between structure and optical properties in glass. If the work contained here can provide any insight to those working on similar problems in the future, then it most certainly has been a success.

Bibliography

[1] A. K. Geim and K. S. Novoselov. The rise of graphene. *Nature Materials 6(3),* pp. 183-191. 2007.

[2] J. Forsgren, S. Frykstrand, K. Grandfield, A. Mihranyan and M. Strømme. A template-free, ultra-adsorbing, high surface area carbonate nanostructure. *PloS One 8(7),* pp. e68486. 2013.

[3] A. Macfarlane and G. Martin. *Glass: A World History.* University of Chicago Press. 2002.

[4] W. J. Smith. *Modern optical engineering: The design of optical systems.* McGraw-Hill. 2008.

[5] M. Guignard, L. Albrecht and J. W. Zwanziger. Zero-stress optic glass without lead. *Chem. Mater. 19(2),* pp. 286-290. 2007.

[6] H. Selin and S. D. VanDeveer. Raising global standards: Hazardous substances and e-waste management in the European Union. *Environment: Science and Policy for Sustainable Development 48(10),* pp. 6-18. 2006.

[7] S. Ganesan and M. G. Pecht. *Lead-Free Electronics.* Wiley-Interscience. 2006.

[8] V. Martin, U. Werner-Zwanziger, J. W. Zwanziger and R. A. Dunlap. Correlation of structure and photoelastic response in tin phosphate glass. *International Journal of Applied Glass Science 2(4),* pp. 282-289. 2011.

[9] N. Yamamoto, A. Saitoh and H. Takebe. Zero photoelastic zinc tin phosphate glass without lead oxide. *Opt. Lett. 37(20),* pp. 4203-4205. 2012.

[10] H. Mueller. The theory of photoelasticity. *J. Am. Ceram. Soc. 21(1),* pp. 27-33. 1938.

[11] W. A. Weyl and E. C. Marboe. *The Constitution of Glasses: A Dynamic Interpretation, Vol 2.* Interscience Publishers. 1962.

[12] A. Lebedev. On polymorphism and annealing of glass. *Tr. Gos. Opt. Inst 2(10),* pp. 1-20. 1921.

[13] R. Roy. Glass science and glassmaking: A personal perspective. *Int. J Appl. Glass Sci. 1(1),* pp. 3-15. 2010.

[14] I. Patel, P. W. Schmidt and S. M. Ohlberg. Small-Angle X-Ray scattering study of phase separation in glasses. *J. Appl. Phys. 43(4),* pp. 1636-1641. 1972.

[15] K. Evstropiev and E. Porai-Koshits, *J. Non Cryst. Solids 11*, pp. 170, 1972.

[16] W. H. Zachariasen. The atomic arrangement in glass. *J. Am. Chem. Soc. 54(10),* pp. 3841-3851. 1932.

[17] B. E. Warren and J. Biscce. The structure of silica glass by x-ray diffraction studies. *J. Am. Ceram. Soc. 21(2),* pp. 49-54. 1938.

[18] H. Sidek, S. Rosmawati, Z. Talib, M. Halimah and W. Daud. Synthesis and optical properties of ZnO-TeO2 glass system. *Am. J. Appl. Sci. 6(8),* pp. 1489-1494. 2009.

[19] Y. Shimizugawa and K. Hirao. The relationship between glass structure and poling-induced optical second harmonic intensity for ZnO–TeO2 glasses. *J. Mater. Res. 11(10),* pp. 2651-2655. 1996.

[20] K. Matusita, C. Ihara, T. Komatsu and R. Yokota. Photoelastic effects in phosphate glasses. *J. Am. Ceram. Soc. 68(7),* pp. 389-391. 1985.

[21] H. Liu and T. Chin. Low melting PbO-ZnO-P2O5 glasses. part 2. A structural study by raman spectroscopy and MAS-NMR. *Phys. Chem. Glass 38(3),* pp. 123-131. 1997.

[22] J. C. Knowles. Phosphate based glasses for biomedical applications. *J. Mat. Chem. 13(10),* pp. 2395-2401. 2003.

[23] J. Campbell and T. Suratwala. Nd-doped phosphate glasses for high-energy/high-peak-power lasers. *J. Non Cryst. Solids 263,* pp. 318-341. 2000.

[24] M. R. Lange, E. Bryant, M. J. Myers and J. D. Myers. High gain coefficient phosphate glass fiber amplifier. Presented at National Fiber Optic Engineering Conference (NFOEC). 2003.

[25] D. Ehrt. Structure, properties and applications of borate glasses. *Glass Technology 41(6),* pp. 182-185. 2000.

[26] Y. Himei, A. Osaka, T. Nanba and Y. Miura. Coordination change of Te atoms in binary tellurite glasses. *J. Non Cryst. Solids 177,* pp. 164-169. 1994.

[27] A. K. Varshneya. *Fundamentals of Inorganic Glasses.* Academic Press. 1994.

[28] V. Martin. Composition and structure dependence of the photoelastic response of oxide glass. PhD Thesis. 2011.

[29] J. Shaw, U. Werner-Zwanziger and J. Zwanziger. Correlation of lead borate glass structure with photoelastic response. *Phys. Chem. Glass. 47(4),* pp. 513-517. 2006.

[30] M. Guignard and J. Zwanziger. Zero stress-optic barium tellurite glass. *J. Non Cryst. Solids 353(16),* pp. 1662-1664. 2007.

[31] G. Walter, U. Hoppe, T. Baade, R. Kranold and D. Stachel. Intermediate range order in MeO-P2O5 glasses. *J. Non Cryst. Solids 217(2),* pp. 299-307. 1997.

[32] A. Montenero, M. Aielli, G. Gnappi, A. Lorenzi, V. Sglavo and G. R. Carfagni. Mechanical properties of PbOZnOP2O5 glasses. *Phys. Chem. Glass 46(5),* pp. 538-543. 2005.

[33] D. E. Sayers, E. A. Stern and F. W. Lytle. New technique for investigating noncrystalline structures: Fourier analysis of the extended X-Ray—Absorption fine structure. *Phys. Rev. Lett. 27(18),* pp. 1204-1207. 1971.

[34] N. Seregin, S. Nemov and S. Irkaev. Study of zinc impurity atoms in GaP, GaAs, and GaSb 67 ga (67 zn) and 67 cu (67 zn) by emission Mössbauer spectroscopy. *Semiconductors 36(9),* pp. 975-976. 2002.

[35] G. Wu. Zinc-67 nuclear magnetic resonance spectroscopy of solids. *Chem. Phys. Lett. 298(4),* pp. 375-380. 1998.

[36] A. Musinu, G. Piccaluga, G. Pinna, G. Vlaic, D. Narducci and S. Pizzini. Coordination of zinc and copper in phosphate glasses by EXAFS. *J. Non Cryst. Solids 136(3)*, pp. 198-204. 1991.

[37] M. Newville, "Fundamentals of XAFS," *University of Chicago,* 2004.

[38] J. J. Sakurai. *Advanced Quantum Mechanics.* Addison-Wesley. 2006.

[39] D. Koningsberger and R. Prins. X-ray absorption: Principles, applications, techniques of EXAFS, SEXAFS and XANES. 1987.

[40] G. Bunker. *Introduction to XAFS: A Practical Guide to X-Ray Absorption Fine Structure Spectroscopy*. Cambridge University Press. 2010.

[41] S. Kelly, D. Hesterberg and B. Ravel. Analysis of soils and minerals using X-ray absorption spectroscopy. *Methods of Soil Analysis Part 5,* pp. 387-463. 2008.

[42] B. Ravel and M. Newville. ATHENA and ARTEMIS: Interactive graphical data analysis using IFEFFIT. *Phys. Scripta 2005(T115),* pp. 1007. 2006.

[43] M. Newville. IFEFFIT: Interactive XAFS analysis and FEFF fitting. *J. Synch. Rad. 8(2),* pp. 322-324. 2001.

[44] M. L. Fuller. A method of determining the axial ratio of a crystal from X-ray diffraction data: The axial ratio and lattice constants of zinc oxide. *Science 70,* pp. 196-198. 1929.

[45] B. Ravel, "Re: Can Sigma-Squared Ever Be Less Than Zero?" *Ifeffit Mailing List,* 2010.

[46] M. Newville, "Re: Correlation Matrix in IFEFFIT," *Ifeffit Mailing List,* 2006.

[47] P. Hariharan. The Sénarmont compensator: An early application of the geometric phase. *J. Modern Optics. 40(11),* pp. 2061-2064. 1993.

[48] J. Bensch and H. Brynard. New approach to density measurements using Archimedes's principle. *Nature 239(93),* pp. 96-96. 1972.

[49] M. McArthur, S. Trussler and J. Dahn. In situ investigations of SEI layer growth on electrode materials for lithium-ion batteries using spectroscopic ellipsometry. *J. Electrochem. Soc. 159(3),* pp. A198-A207. 2012.

[50] T. Sekiya, N. Mochida and A. Ohtsuka. Raman spectra of MO-TeO2 (M = Mg, Sr, ba and Zn) glasses. *J. Non Cryst. Solids 168(1–2),* pp. 106-114. 1994.

[51] H. Matsumoto, T. Mabuchi, Y. Shigesato and I. Yasui. Structure analysis of ZnO-TeO2 glasses by means of neutron diffraction and molecular dynamics. *Jpn J. Appl. Phys. 35,* pp. 694-698. 1996.

[52] V. Kozhukharov, H. Bürger, S. Neov and B. Sidzhimov. Atomic arrangement of a zinc-tellurite glass. *Polyhedron 5(3),* pp. 771-777. 1986.

[53] H. Bürger, K. Kneipp, H. Hobert, W. Vogel, V. Kozhukharov and S. Neov. Glass formation, properties and structure of glasses in the TeO2-ZnO system. *J. Non Cryst. Solids 151(1),* pp. 134-142. 1992.

[54] T. Komatsu, N. Ito, T. Honma and V. Dimitrov. Temperature dependence of refractive index and electronic polarizability of RO–TeO2 glasses (R=Mg, Ba, Zn). *Solid State Sciences 14(10),* pp. 1419-1425. 2012.

[55] K. Matusita, R. Yokota, T. Kimijima, T. Komatsu and C. Ihara. Compositional trends in photoelastic constants of borate glasses. *J. Am. Ceram. Soc. 67(4),* pp. 261-265. 1984.

[56] R. K. Brow, D. R. Tallant, S. T. Myers and C. C. Phifer. The short-range structure of zinc polyphosphate glass. *J. Non Cryst. Solids 191(1),* pp. 45-55. 1995.

[57] U. Hoppe, E. Yousef, C. Rüssel, J. Neuefeind and A. Hannon. Structure of zinc and niobium tellurite glasses by neutron and x-ray diffraction. *J Phys: Condensed Matter 16(9),* pp. 1645. 2004.

[58] S. Sakida, J. Jin and T. Yoko. X-ray diffraction study of MO-TeO2 (M= Zn and Ba) glasses. *Phys. Chem. Glass. 41(2),* pp. 65-70. 2000.

[59] J. Ayuni, M. Halimah, Z. Talib, H. Sidek, W. Daud, A. Zaidan and A. Khamirul. Optical properties of ternary TeO2-B2O3-ZnO glass system. Presented at IOP Conference Series: Materials Science and Engineering. 2011.

[60] A. Kajinami, Y. Harada, S. Inoue, S. Deki and N. Umesaki. The structural analysis of zinc borate glass by laboratory EXAFS and X-ray diffraction measurements. *Jpn. J. Appl. Phys. 38S1(38-1),* pp. 132. 1999.

[61] V. Martin, B. Wood, U. Werner-Zwanziger and J. W. Zwanziger. Structural aspects of the photoelastic response in lead borate glasses. *J. Non Cryst. Solids 357(10),* pp. 2120-2125. 2011.

[62] K. Suzuya, K. Itoh, A. Kajinami and C. K. Loong. The structure of binary zinc phosphate glasses. *J. Non Cryst. Solids 345*pp. 80-87. 2004.

[63] U. Hoppe, G. Walter, R. Kranold, D. Stachel and A. Barz. The dependence of structural peculiarities in binary phosphate glasses on their network modifier content. *J. Non Cryst. Solids 192,* pp. 28-31. 1995.

[64] T. Okura, K. Yamashita and T. Kanazawa. A structural explanation for the phosphate glass anomaly. *Phys. Chem. Glass. 29(1),* pp. 13-17. 1988.

Appendix A

EXAFS Data, Data Processing and Analysis

The contents of this appendix are based on Demeter version 0.9.13. Demeter is written by Bruce Ravel and is available at: http://bruceravel.github.com/demeter/

EXAFS Data

A copy of the raw data used here is archived in Dalhousie's DalSpace institutional repository along with the electronic version of this thesis.
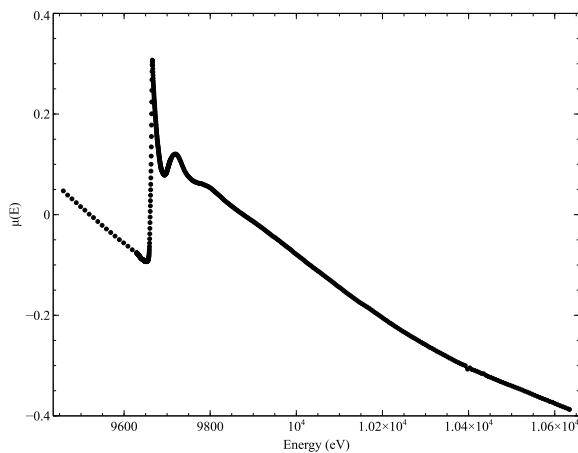
Fig. A1: Absorption spectrum of sample ZT15
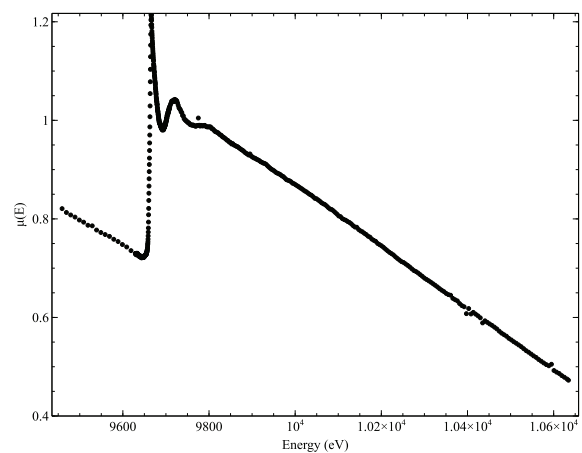
Fig. A2: Absorption spectrum of sample ZT20
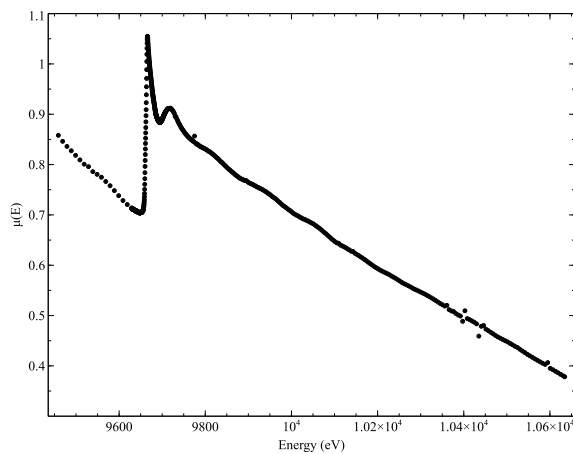
Fig. A3: Absorption spectrum of sample ZT25
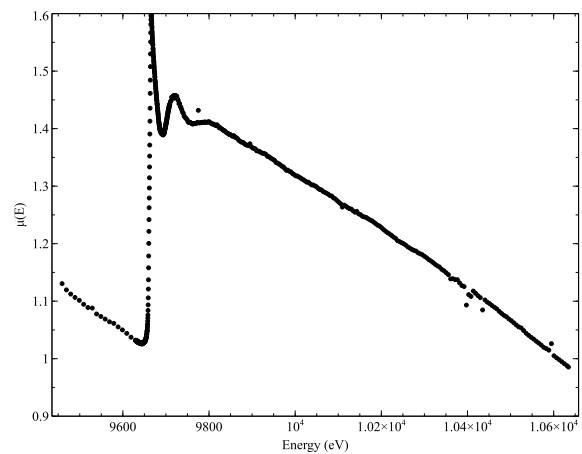
Fig. A4: Absorption spectrum of sample ZT30

78
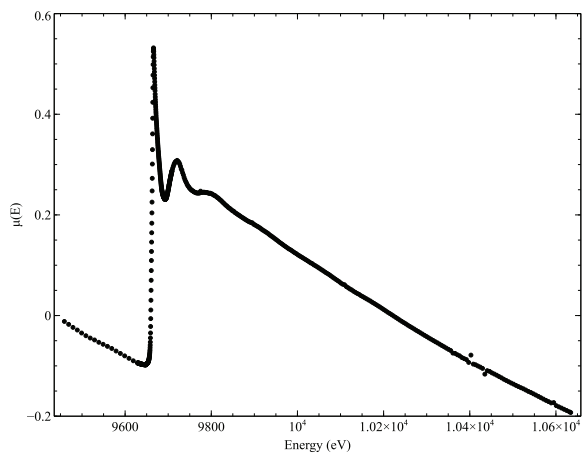
Fig. A5: Absorption spectrum of sample ZT35
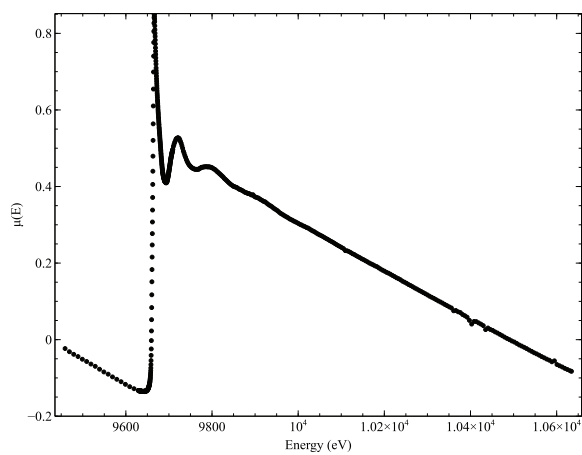
Fig. A6: Absorption spectrum of sample ZT40
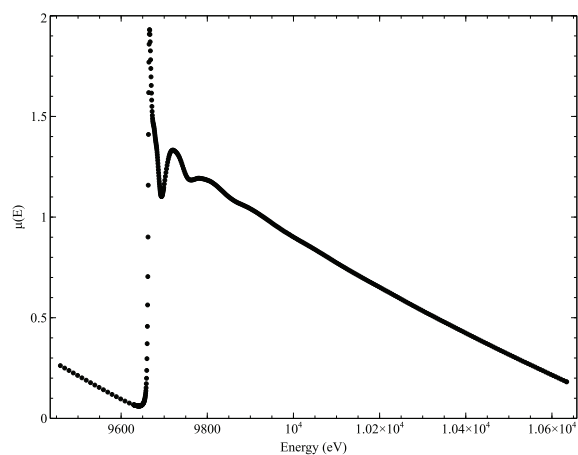
Fig. A7: Absorption spectrum of sample ZB30
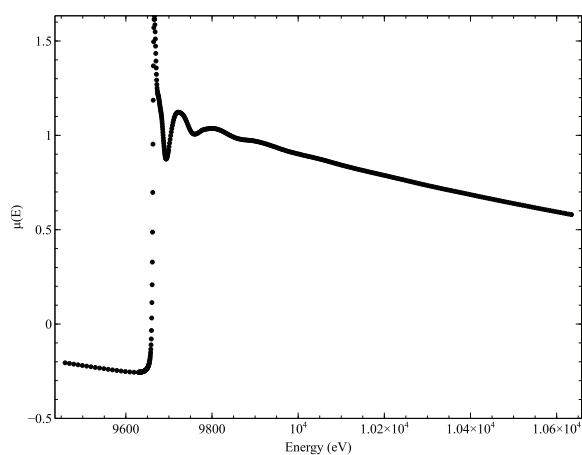
Fig. A8: Absorption spectrum of sample ZB40
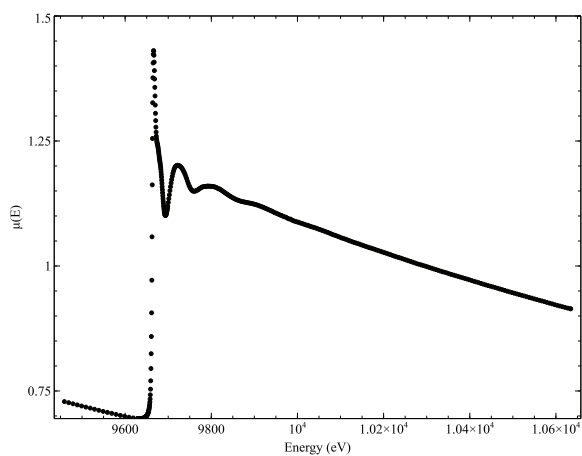
Fig. A9: Absorption spectrum of sample ZB50
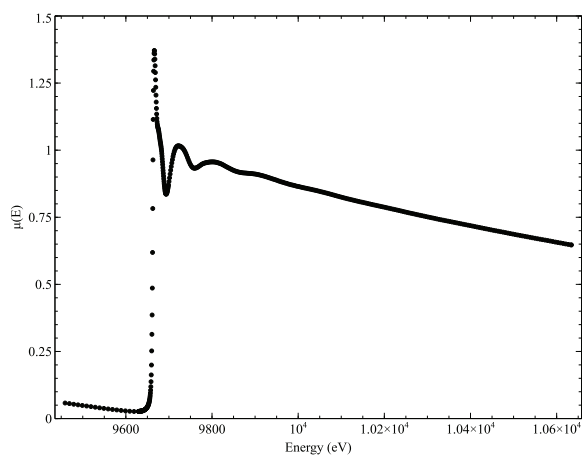
Fig. A10: Absorption spectrum of sample ZB60
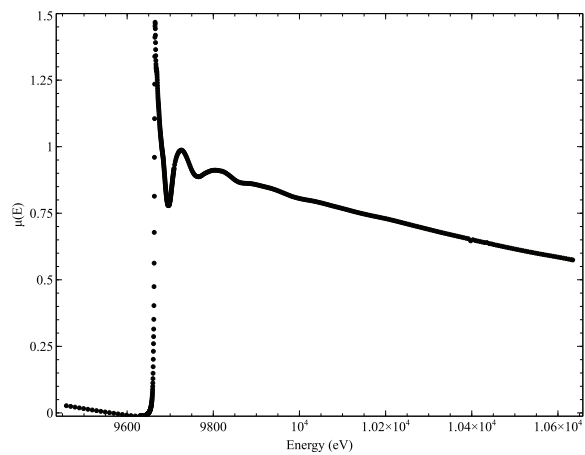
Fig. A11: Absorption spectrum of sample ZP45
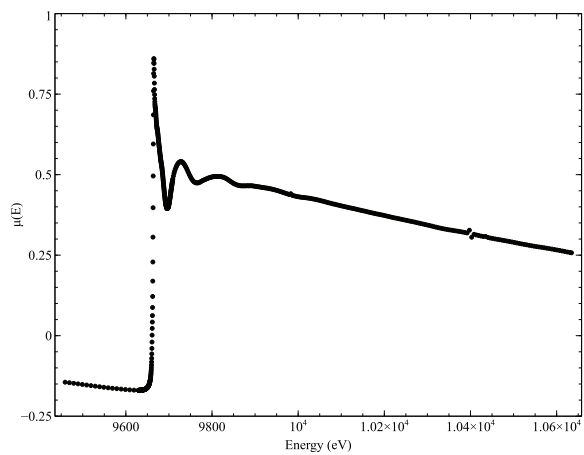
Fig. A12: Absorption spectrum of sample ZP50

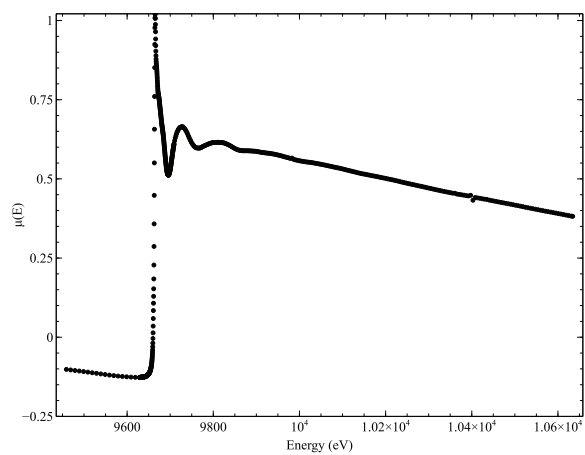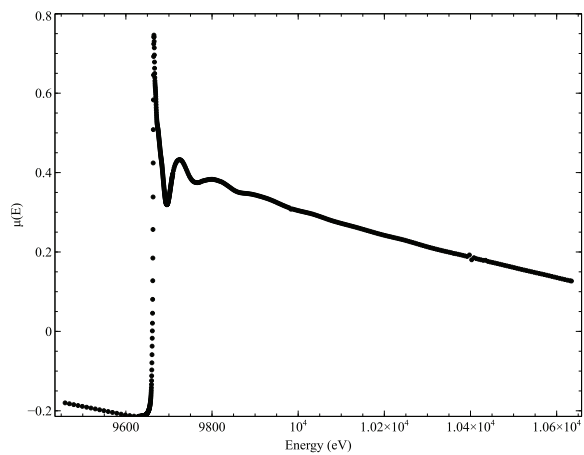Fig. A13: Absorption spectrum of sample ZP55

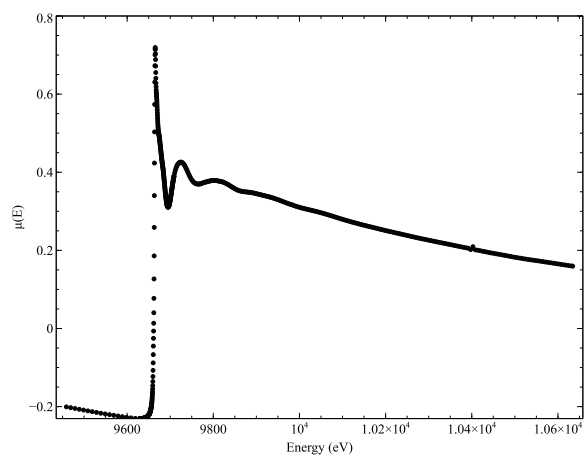Fig. A14: Absorption spectrum of sample ZP60

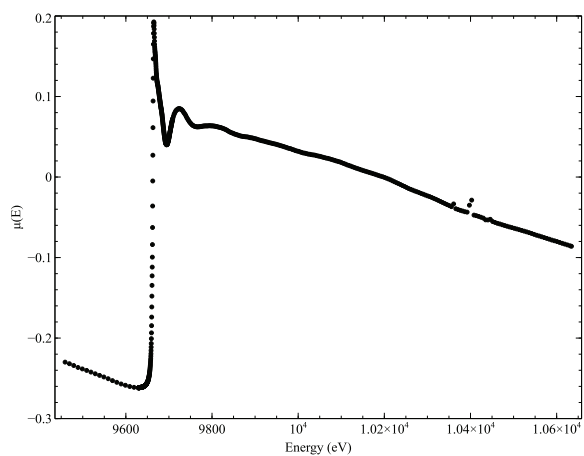

Fig. A15: Absorption spectrum of sample ZP63

Fig. A16: Absorption spectrum of sample ZP645

Data Processing in Athena

Raw data files containing x-ray energy and measured intensities from each detector in the EXAFS experiment are imported into Athena. Athena can import and process many files at once. To construct absorption spectra from data files, Athena must first be told which data columns represent the x-ray energy and which represent the measured intensities before and after the sample. Athena then knows the value of the absorption coefficient, $\mu(E) = -\ln(I_{incident}/I_{transmitted})$, at each value of energy, depending on which columns of intensities are chosen as the numerator and denominator.
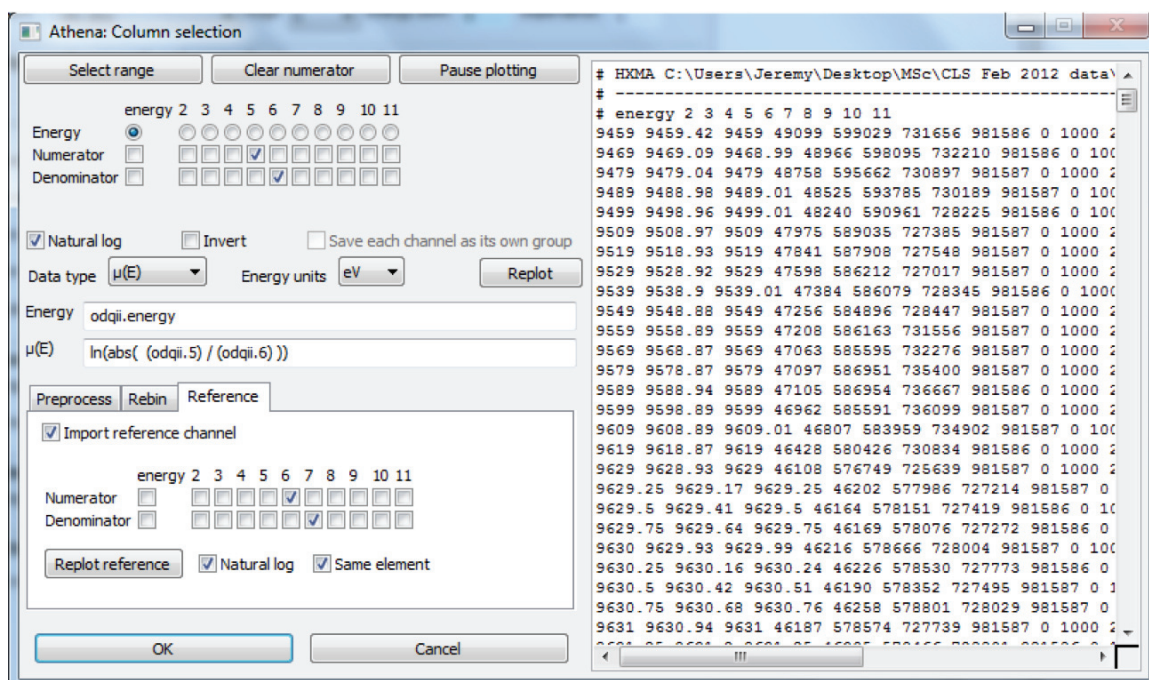

Fig. A17: The column selection window in Athena v. 0.9.13

In this data, column 5 contains I_1 data and column 6 contains I_2, so box 5 is selected for Numerator and box 6 for Denominator. "Natural log" is selected and the data type is set as "$\mu(E)$". Energy units are set to eV. It is also useful to import a "reference" channel – typically, data from a foil standard between detectors I_2 and I_3 for every scan. This allows one to align data later, so that a set of 3 scans will be on the exact same energy grid. "Import reference channel" is selected and boxes 6 and 7 are checked, for I_2

and I_3. Clicking OK creates an absorption spectrum and reference channel for each data file imported. These appear in the panel on the right of Athena's data processing window.
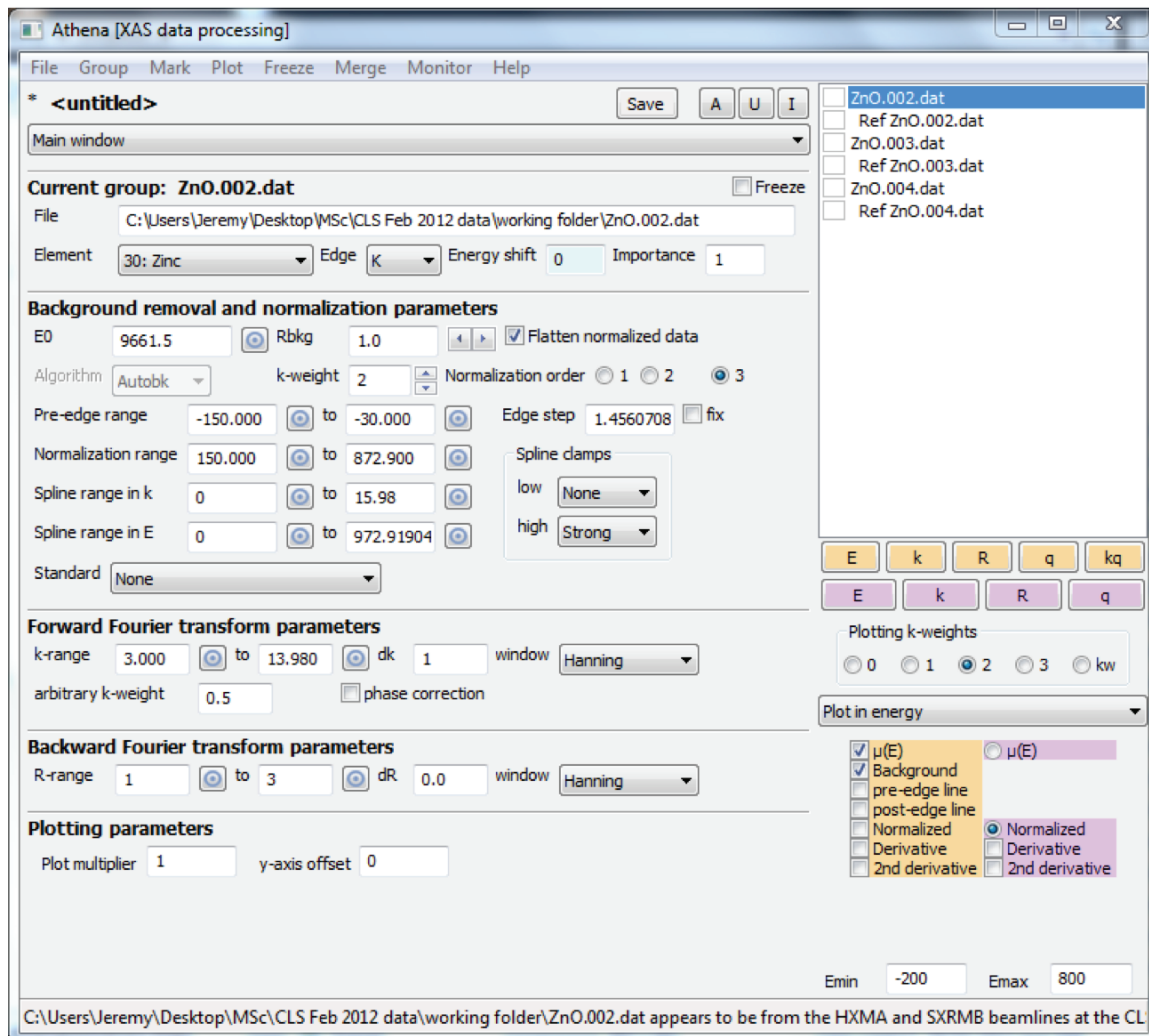

Fig. A18: The data processing window in Athena, showing 3 scans of ZnO and corresponding reference data.

The data processing window allows one to perform every step necessary to convert the absorption spectra into $\chi(k)$ data. Generally, this involves a background removal, normalization and Fourier transform of the data. Each operation depends on a number of parameters, such as the choice of element, edge energy (E0) and ranges in energy, k-space and R-space. Athena automatically examines the data and chooses suitable parameters for these operations, which in many cases require no further adjustment. For the purposes of this work, Athena's values were used without modification.

Two additional operations can be performed to ensure the highest quality data output possible: aligning and deglitching. Since each reference spectrum is from the same zinc foil standard, they should theoretically all be on the same energy grid. In practice, there may be small differences between scans but alignment corrects this. The second and third reference scans in a 3-scan set are aligned with the first. Since the energy scale of each sample scan is tied to its reference, this process aligns all sample scans as well.
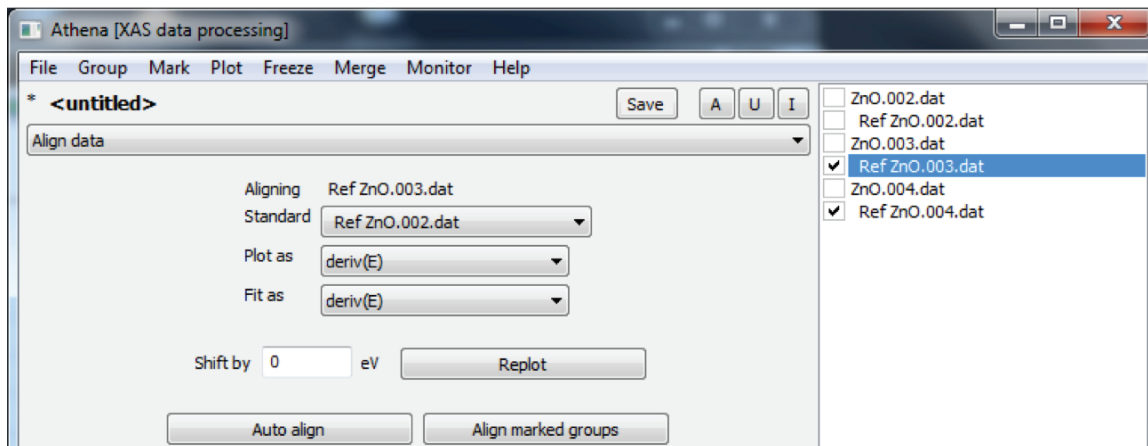

Fig A19: Data alignment in Athena

Occasionally, glitches appear in the absorption spectrum due to sample inhomogeneities, imperfections in the monochromator or other factors. Athena can correct these by deleting individual data points that are far removed from the rest of the measured spectrum. Under "Deglitch and truncate data", the user selects the relevant points by clicking on them, and then clicks "Remove point".
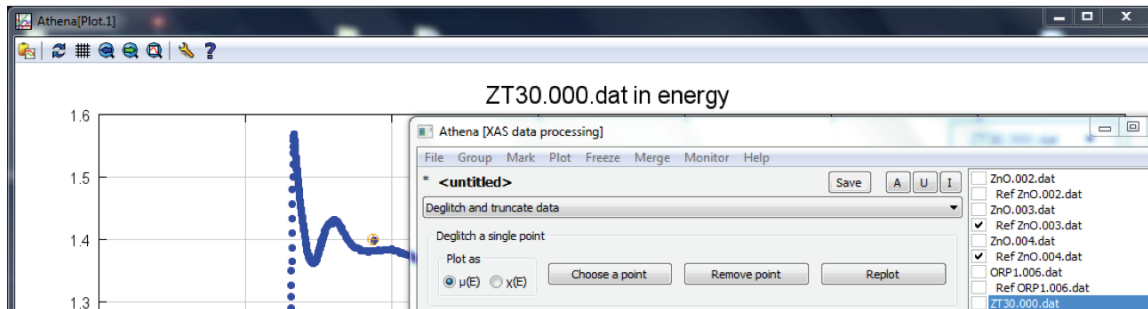

Fig A20: Glitch removal in Athena

The final step in data processing is to create a $\chi(k)$ spectrum for each sample, to be saved in an output file. In the main window, every scan from a single sample is selected and "Merge $\chi(k)$" is chosen from the Merge menu. The Merge operation automatically carries out the background removal, normalization and Fourier transform as specified previously. The spectra from each scan are averaged resulting in a single $\chi(k)$ for every sample. The Athena project file (.prj) is saved so that it may later be imported with Artemis for data analysis.

Athena contains many other features and functions which are beyond the scope of this work. The above description is sufficient to carry out basic processing on the type of data used to create this thesis.

Data Analysis in Artemis

Artemis provides all of the necessary tools for extracting meaningful physical information, such as bond lengths and coordination numbers, from EXAFS data. Once $\chi(k)$ data is imported, the user chooses a number of photoelectron scattering paths that may exist in the sample based on a similar crystal structure. Several parameters from the EXAFS equation are chosen to vary and Artemis attempts to fit EXAFS equations to the specified scattering paths to construct a spectrum which closely resembles the measured $\chi(k)$. If a good fit is obtained, the user has some knowledge about the structural parameters in the sample that gave rise to the experimental spectrum.

To begin, the project file from Athena is chosen from the File menu to be imported. If the project contains data for many samples, the user chooses which to import. Next, a "FEFF" model is created based on a known crystal structure. The FEFF6 module is used within Artemis to find possible scattering paths that exist in a structure and the corresponding scattering amplitudes and phase shifts. The user imports (from a .cif or .inp file) or manually specifies a crystal structure. Clicking "Run Atoms" generates a list of atomic coordinates for all atoms that exist in the structure out to a specified radius. "Run FEFF" then computes all possible scattering paths that exist between the core atom and its neighbours and outputs a list of paths.

The user must select scattering paths that they believe are present in the sample material. Paths are listed by how heavily they would contribute to the amplitude of the EXAFS signal, so in general, the earlier paths in the list are the most significant. Trial and error is necessary to determine which paths will be included in the final fit, but the general approach is to include all paths that contribute positively to the quality of the fit and none that contribute negatively, assuming one's choices are physically justifiable. The chosen paths are dragged from the FEFF onto the paths list in Artemis' Data window.
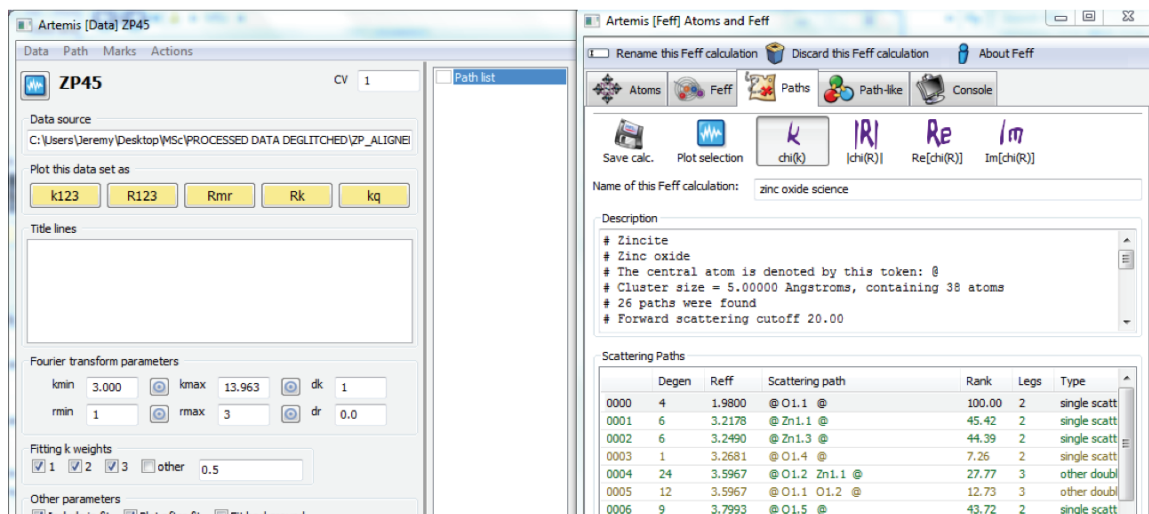

Fig A21: ZnO scattering paths in FEFF and Artemis' path list

To carry out a fit, guess parameters and their initial values must be defined. It is common to begin with 4 guess parameters: The amplitude factor S_0^2, the energy shift $\Delta E0$, the path length difference ΔR and the variance in the absorber-scatterer distance, σ^2. The guess parameters for each path are defined in the Data window, and assigned values in the GDS window.
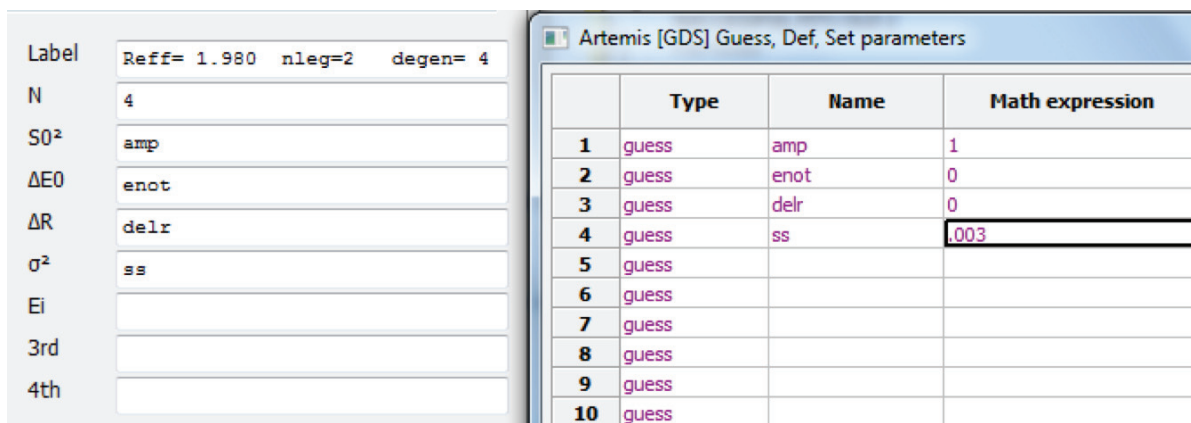
Fig. A22: Defining guess parameters and assigning initial values

Artemis is now able to carry out a fit using the chosen guess parameters, FEFF model and EXAFS data. For each path in the path list, Artemis fits an EXAFS equation containing the guess parameters chosen for that path. When the calculated $\chi(k)$ is as close as possible to the measured $\chi(k)$, the final fit is shown along with a log of the fitting process.
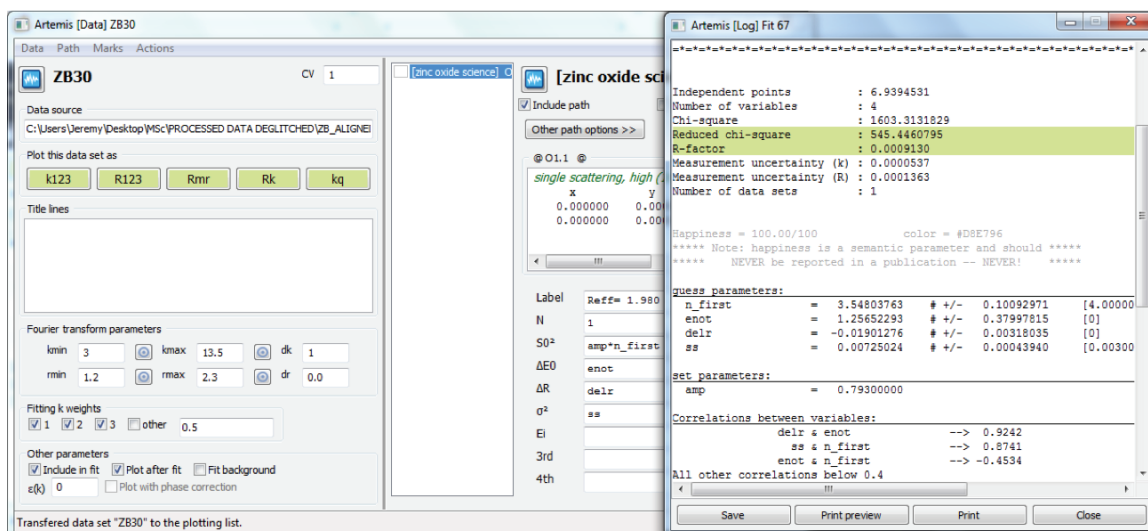

Fig. A23: Artemis' Data window and fit log

Much of the log pertains to the "goodness" of the fit. One must consider many factors when deciding whether or not a fit is "good enough", but generally the most important are the reduced chi-square and R-factor (each which must be minimized, as they indicate the mismatch in the fit) and the ratio of number of variables to number of independent points, which must not be too high.

The number of variables is the number of fitting parameters used. The number of independent points is the information content of the data, as determined by the Nyquist criterion. Assuming the $\chi(k)$ signal is a sum of perfect sine waves, the number of independent points in the data would be $N = 2\Delta k \Delta R / \pi$, where Δk and ΔR are the ranges in k and R-space over which the fit was performed. Realistically, the information content would be considerably less, i.e. $N < 2\Delta k \Delta R / \pi$. Therefore, the number of variables must be less than the number of independent points. Generally, a ratio of 2/3 is considered acceptable by members of the XAFS community.

To achieve the best possible fit, one should consider the following principles at all times:

i)   Include as much good quality data and as little poor quality data as possible in the fitting ranges.

ii)   Make physically defensible choices of guess parameters and assign reasonable starting values.

iii)   Include all scattering paths that are believed to be present in the material and that contribute positively to the quality of the fit.

Not all principles can be perfectly adhered to at all times. For example, if the information content of the data is limited, there may not be enough independent points to allow the user to introduce the guess parameters necessary for fitting 2nd or 3rd coordination shells.

Error bars are calculated by Artemis and reported beside the guess parameter results. One can assume these are the correct size for the reported values. However, there may be experimental sources of uncertainty that Artemis has no knowledge of. For example, it is common to assume that the amplitude parameter S_0^2 determined from an elemental standard is equal to that for a sample containing the same element. If this is not exactly the case, perhaps due to over-absorption or sample inhomogeneities, then there will be additional uncertainties for the user to consider and propagate manually.

With EXAFS, coordination numbers are never determined directly in the way that other parameters, such as bond lengths, are. The reason for this is that coordination number and amplitude are multiplied in the EXAFS equation, so they cannot be fit independently. The two parameters are 100% correlated. The best one can do is fit the product of the two: $N*S_0^2$. If one can know the value of S_0^2 prior to the fit, then in

principle, coordination number can be determined. In practice, this is commonly done like so:

i) Measure a well-known standard, such as a metal or oxide containing the same core element as the sample of interest, under identical experimental conditions.

ii) By holding the known coordination number of the standard fixed, determine S_0^2 for the standard. In theory, S_0^2 is chemically transferable. That is, it should be the same for any sample with the same core element.

iii) When analyzing the sample, fix the value of S_0^2 determined from the standard. In Artemis, one sets the amplitude parameter to "set" in the GDS window and assigns the determined value. Then, in the Data window, the path corresponding to the coordination shell of interest is selected. "N" is fixed at 1 and S_0^2 is given a mathematical expression like "amp*n_first", meaning the fixed amplitude parameter multiplied by a guess parameter called n_first. Now when Artemis calculates amplitude, it is actually calculating (amplitude)*(coordination number), with amplitude fixed at a known value. Thus, the value reported for n_first represents coordination number.

Label	Reff= 1.980 nleg=2 degen= 4
N	1
S0²	amp*n_first
ΔE0	enot
ΔR	delr
σ²	ss

Artemis [GDS] Guess, Def, Set parameters

	Type	Name	
1	set	amp	0.79300
2	guess	n_first	4.00000
3	guess	enot	0
4	guess	delr	0
5	guess	ss	0.00300

Fig A24: Parameters for determining coordination number in Artemis